Investigating the effect of retained austenite on wear and fatigue behavior of AISI 8620 steel

by

Sougata Roy

A dissertation submitted to the graduate faculty

in partial fulfillment of the requirements for the degree of

DOCTOR OF PHILOSOPHY

Major: Mechanical Engineering

Program of Study Committee:
Sriram Sundararajan, Major Professor
Pranav Shrotriya
Gap-Yong Kim
Scott Chumbley
Wei Hong

The student author, whose presentation of the scholarship herein was approved by the program of study committee, is solely responsible for the content of this dissertation. The Graduate College will ensure this dissertation is globally accessible and will not permit alterations after a degree is conferred.

Iowa State University

Ames, Iowa

2018

TABLE OF CONTENTS

LIST OF FIGURES

Page

LIST OF TABLES

Page

NOMENCLATURE

RA	Retained Austenite
WEC	White Etching Crack
WEA	White Etching Area
RCF	Rolling Contact Fatigue
AISI	American Iron and Steel Institute
XRD	X-Ray Diffraction
RS	Residual Stress
SRR	Slide-to-Roll Ratio
CI	Confidence Interval
DoF	Degree of Freedom
SiC	Silicon Carbide
MPR	Micro Pitting Rig
XFEM	eXtended finite element method
P/P	Peak to Peak
SE	Secondary Electron
BSE	Back Scattered Electron
CL	Correlation Length
AACF	Average Auto Correlation Function
FCC	Face Center Cubic
BCC	Body Center Cubic
BCT	Body Center Tetragonal

ACKNOWLEDGEMENTS

I would like to take this opportunity to express my gratitude to all those who have helped me with the various ways during my Doctoral study which have been explicitly reported this dissertation. First and foremost, I would like to thank my advisor, Professor Sriram Sundararajan for his constant support, guidance and the unshakable trust he had in me throughout my Ph.D. study. He was not only a Ph.D. supervisor but a great mentor who always guided me with valuable resources so that I can reach my long-term goals in my career. It was through him I learnt how to manage work-life balance maintaining a busy work schedule.

I would also like to extend my sincere thanks to all my committee members for serving on my Program of Study (POS) committee and providing me with all the valuable inputs and suggestions for my research. I would like to thank Professor Pranav Shrotriya (Mechanical Engineering) for his constant support with valuable comments and allowing me to use his laser facility for my study. I would also like to express my gratitude to Professor Scott Chumbley (Material Science and Engineering) for Materials Science based discussions, Professor Wei Hong (Aerospace Engineering) for providing valuable insight into fracture mechanics and finite element modelling and Professor Gap-Yong Kim (Mechanical Engineering) for his encouragement and advice during the study.

I would also like to thank all the collaborators at Iowa State University with whom I have worked in the various research projects. I am thankful to Wyman Martinek, Jim Shelledy and Taylor Schweizer in the Mechanical engineering department for their great help in sample preparation of the studies related to abrasive wear. For the material characterization, Warren Straszheim and Scott Schlorholtz from Materials Analysis

Research Laboratory, Gaoyuan Ouyang and Kurt T. Koch from Ames Laboratory. I am extremely grateful to Dr. Curtis L. Mosher for training me on Atomic Force Microscope and guiding me to work on topographical study of gold (AU) nanoparticle coated surfaces (not included in dissertation).

I would like to convey my gratitude to the following industrial collaborators who made it possible to perform the various studies reported in this dissertation. Jake McCann and Clayton Short at Advanced Heat Treat (USA) helped to get the samples heat treated properly for the wear study. Richard Candler and Ian Griffin at Wallwork (UK) helped to get the samples carburized for the rolling contact fatigue (RCF) studies. I am also thankful to Matt Smeeth at PCS instruments (UK) for preparing the samples for RCF studies. I am grateful to Erina kagami at Rigaku corporation (USA) for guiding me to set protocols for micro-XRD studies, Benjamin Gould, Ye Zhou, Nick Demas and Aaron Greco from Argonne National laboratory (USA) for characterizing white etching cracks in micropitted samples.

I would like to express my gratitude to my former and current colleagues in the Multiscale Surface Engineering and Tribology Laboratory – Therin Young, Alex Jenson, George Ooi, Derek White, Jeremy Wagner, Yosef Jazaa, Gowtham Sivakumar, Jocelyn Jackson, Daniel Renier, Allison Gregorovic, Anvay Pradhan and William Beachner. In addition, my thankfulness goes to my colleagues and all of Professor Shrotriya's students in Advance Sensors and Nanoscale Mechanics Lab – Jingnan Zhao and Kwang Wong for helping me during laser surface treatment study. Each of my colleagues has been a source of entertainment and support with whom I have shared all my professional ups and downs and the mutual encouragement we boosted upon each other.

Financial support for this study was provided by John Deere Product Engineering Center in Waterloo, Iowa and Iowa State University.

Finally, I would like to thank my parents for all their countless sacrifices and in-laws for their constant encouragement from the beginning and the person who has been through thick and thin as my strongest source of strength, my wife Sayani for her love, support and patience through all these years.

ABSTRACT

Enhancing the operational life and reliability of drivetrain components via heat treatment routes is a long-studied topic of research. By varying parameters using heat treatment, the resulting attributes of the material such as hardness, residual stress, amount of retained austenite (RA), microstructure, grain size, grain orientation etc. can be varied. While the effect of hardness and residual stress on the resulting tribological properties of the steel is well known, the effect of RA is not as clearly understood yet. In this study, AISI 8620 steel samples were subjected to several heat treatment schemes using conventional and laser based surface treatment routes to vary the amount of RA. The samples were subsequently used to conduct wear and rolling contact fatigue tests where samples are compelled to fail due to abrasive wear, micropitting, macropitting and white etching crack (WEC) formation. By conducting these systematic experiments, the effect of RA on those failure modes was elucidated using several surface based and microstructure based experimental techniques.

It was observed that at higher contact pressures, a higher hardness and higher RA% result in superior wear resistance. This is attributed to the higher hardness resulting from the heat treatment route to generate higher RA% as well as martensitic transformation of austenite during sliding. Generated RA% due to laser treatment was higher at lower scanning velocity and with air and nitrogen as a shielding gas compared to argon but was limited to below 10%. Higher RA had significant effect on micropitting but less significant effect on macropitting since sub-surface cracks observed to have a compelling impact on macropitting life. Higher RA samples showed far more branching WEC networks, and the white etching area adjacent to the crack networks was less defined. The

study establishes the role of RA on tribomechanical behavior in the context of other mechanical and microstructural phenomena as well as the correlation of behavior to heat treatment routes for preferred wear and fatigue life. Overall, the findings will provide valuable input for the design and manufacturing of drivetrain components for a wide range of applications ranging from agricultural equipment to the wind energy sectors.

CHAPTER 1. INTRODUCTION

1.1 Background and Motivation

Drivetrain components manufactured from steel are one of the most crucial components in machinery. Enhancing the operational life and reliability of these components via heat treatment routes is a long-studied topic of research, both via experiments and computational modelling [1-5]. Depending upon the type of steel being used for a particular component and its application, five heat treatment routes are most popularly used. These are carburizing, carbo-nitriding, nitriding, nitro-carburizing and boronizing [6]. Carburizing is a popular technique used for low carbon steels at temperatures between 850-950°C where carbon is diffused to iron or steel surface layer typically resulting in increased hardness, residual stress and fatigue/tensile strength. By varying parameters during the carburizing and any subsequent quenching processes, the resulting attributes of the material such as hardness, residual stress, amount of residual austenite (RA), microstructure, grain size, grain orientation etc. can be varied [7-12].

Retained Austenite (RA) and heat treatment of steel

Austenite that does not transform to martensite during quenching is called retained austenite or RA. Thus, RA presents on the surface when the steel is not quenched up to martensite finish (M_f) temperature which is temperature is not low enough to form 100% martensite. Different techniques can be used to decrease M_f temperature below room temperature. One of them is increasing carbon potential during carburizing [13, 14]. This increased carbon percentage in austenite helps to depress both martensite start (M_s) and martensite finish (M_f) temperature resulting higher RA levels in microstructure.

Figure 1.1 shows a steel microstructure containing retained austenite and martensite. Under light microscope, the white areas (zones which are not etched) are called RA. The blackish needle like zones are called martensite. Under specific loading conditions this RA can transform to martensite and is called martensitic phase transformation. In case of Transformation Induced Plasticity or TRIP steels RA can be transformed to martensite during operation. Martensite is formed by a shear mechanism where atoms move cooperatively and simultaneously. The shear forces displace the newly formed martensite partly above and partly below the surface of the parent austenite phase. Plastic deformation of the parent austenite is possible in steel because the austenite has sufficient ductility.

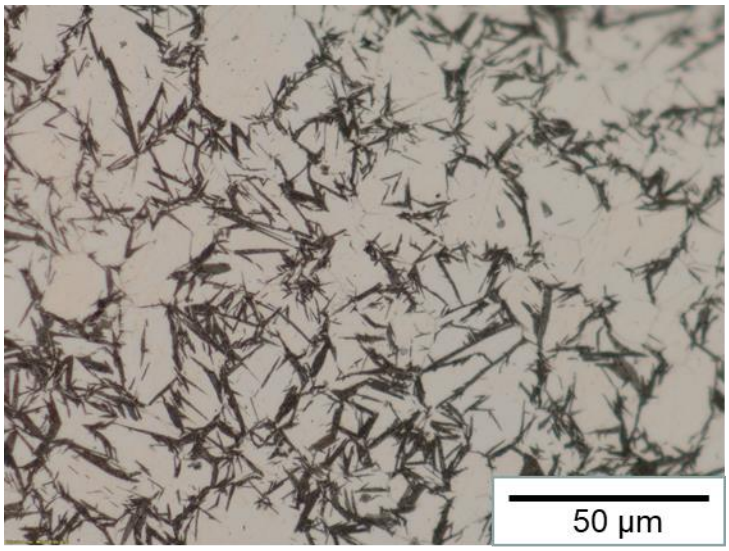

Figure 1.1: Steel microstructure containing austenite (white region) and martensite (black regions)

In this study two different routes were used to vary RA percentage on steel surface using laser surface treatment and conventional heat treatment. Different researchers have conducted experiments by varying different laser treatment parameters such as laser power [15], shielding gas [16], overlapping percentage [17] to modify microstructural properties.

In case of conventional heat treatment RA can be varied by changing carbon potential during carburizing, quenching media and temperature [13], tempering time and temperature [18, 19] and deep-freezing [20-22]. Along with RA percentage, each of these steps can affect some other microstructural properties simultaneously. Detailed microstructural observation and different mechanical behaviors were also studied to observe the effect of heat treatment routes on those microstructural properties.

While the effect of hardness and residual stress on the resulting tribological properties of the steel is well known, the effect of retained austenite (RA) is not as clearly understood [7, 8, 13, 15, 23-28]. Siepak [7] utilized thermal treatment to obtain varying RA% in carburized 12HN3A steel samples and observed that RA had a beneficial effect on wear resistance for a contact pressure between 300-1400 MPa, a rolling-sliding (10%) condition and for specimens with comparatively lower hardness range. Li et al. [24] followed two different routes to get samples with different RA%, one by changing austenitization temperature and other by quenching temperature. He conducted impact wear test and reported that RA has no effect on wear resistance with hard abrasives while showing a positive effect with soft abrasives whereas other studies [29] showed results contrary to Li's observation. Kim and Kweon [13] reported that as the RA% in carburized steels increased from 6 to 30%, the wear resistance decreased while beyond 30 % the wear resistance increased with an increase in RA under dry sliding conditions. They also observed that samples with higher RA% exhibited higher hardness, which is contrary to Siepak's [7] observation where he had shown 40% RA samples showing significantly lower hardness than samples with only martensitic microstructure. These studies suggest that it is often challenging to separate the effect of RA from the effect of other parameters

(e.g. hardness) on the resulting tribological behavior. Thus, there is a need to better understand the impact of heat treatment routes using conventional carburizing and laser surface hardening on steels and the affect that the heat treatment may have on the resulting tribological behavior, especially in the context of the amount of retained austenite.

The basic assumption in case of liquid lubrication is that, although there is resistance to shear within the fluid due to its viscosity and the viscous resistance is much smaller than the frictional resistance observed during dry sliding. The performance of a lubricated contact is therefore largely determined by the viscosity of lubricating oil. Viscosity is the resistance to flow and is the ratio of shear stress to shear strain rate for the lubricating oil. In case of Newtonian fluid, the viscosity is a constant, i.e. there is a linear relationship between stress and strain rate. However, in reality, most of the lubricants show non-Newtonian behavior by showing changes in viscosity due to temperature, pressure and shear rate during operating conditions. The important function of a lubrication oil is to create and maintain a lubrication film between two surfaces which are in relative motion. The film thickness depends on lubricant viscosity, applied load and relative velocity of mating surfaces. There are generally considered to be four lubrication regimes: boundary, mixed, elastohydrodynamic (EHL), and hydrodynamic. Some researchers mention mixed and EHL regime together as mixed lubrication (see Figure 1.2). The film thickness ratio or lambda ratio (λ) is calculated using minimum oil film thickness under operating condition (H_{min}) and measured initial composite roughness (Rq)of both surfaces.

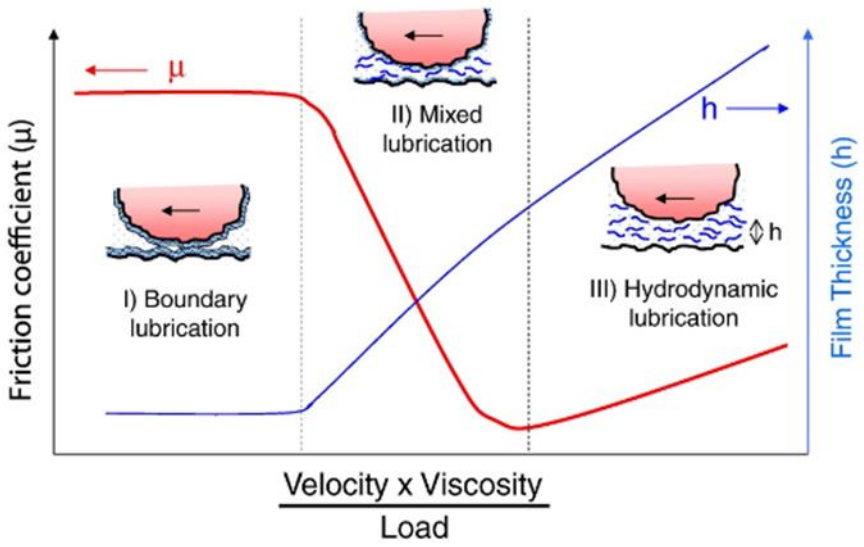

Figure 1.2: Lubrication regimes as a function of operating parameters [30]

Based on lambda ratio (λ), the lubrication regimes can be divided into four categories:

- Boundary lubrication, $\lambda < 1$
- Hydrodynamic lubrication, $\lambda > 5$
- Mixed lubrication, $1 < \lambda < 3$
- Elastohydrodynamic lubrication, $3 < \lambda < 5$

The lubrication film thickness is lowest in case of boundary lubrication and it gradually increases to hydrodynamic lubrication case. In present study, the effect of RA on different RCF failure modes are observed in boundary lubrication regimes which is high load and low speed combination case. This type of operating condition is observed in gear drives of agricultural machineries, wind-turbines and earth moving equipment.

Much research has been aimed at alleviating rolling contact fatigue by modifying material, properties including retained austenite [31], residual stress [32] and employing different heat treatment techniques [33] and coatings [34]. In case of retained austenite, Rivero and Rudd observed higher initial RA on bearing balls can lower their service life [35]. On the

other hand, Dommarco et al. showed superior rolling contact fatigue life for samples with increased RA [31]. These contradictory results suggest that the role of RA on RCF needs further detailed investigation. Secondly, most of the recent studies focus on the effect of different surface coatings [34, 36] and lubricants [37-40] on micropitting, but there is comparatively a dearth of literature that addresses the microstructural implications on four crucial RCF failure modes i.e. abrasive wear, micropitting, macropitting and white etching crack formation. These four failure modes are discussed briefly in the section below:

Abrasive wear

Abrasive wear happens when a hard surface slides on a soft surface. The type of contact in case abrasive wear determines whether it is a two-body abrasion or three body abrasion. Figure 1.3 shows the fundamental difference between abrasive and adhesive wear mechanism.

Figure 1.3: Abrasive wear mechanism [41]

In case of two body abrasion, grits or hard particles remove material from opposite surface. In case of three body abrasion, external abrasion particles which are present in the contact zone conduct the wear process. Based on severity of wear, abrasive wear can be divided into three modes: ploughing, wedge formation and cutting. Plowing occurs when the material is displaced to the edges resulting formation of grooves on the worn part. In case of cutting, material is separated from the surface in the form of debris or microchips. This

is the most severe condition of abrasive wear. The transitional mode from ploughing to cutting is called wedge formation.

Micropitting

Micropitting is a surface contact fatigue which occurs in rolling-sliding contacts. This is also called gray staining or frosting due to its appearance on failed surface as showed in Figure 1.4. In bare eye, micropitted surface looks dull, stained with patches of gray (morphology of micropitting). Micropitting begins with attacking high points on gear tooth or bearing surfaces. Based on experimental studies, eventually during RCF life numerous microscale cracks are initiated at or very close to surface. These cracks then propagate from surface into the bulk material at a shallow angle until ruptures to form a shallow micropit. According to ISO 15144 micropitting is "a phenomenon that occurs in Hertzian types of rolling and sliding contact that operates in elastohydrodynamic (EHL) or boundary lubrication regimes" [42].

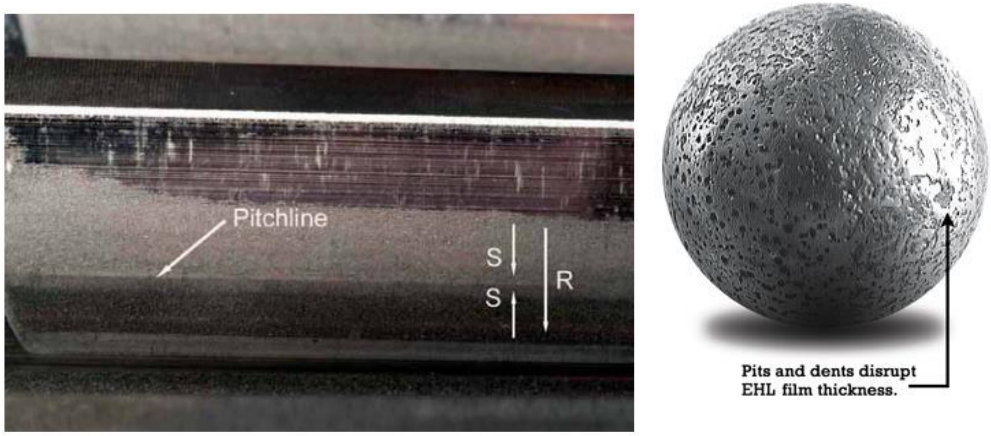

Figure 1.4: Representative images of micropitting phenomena observed in gears (left) [43] and bearings (right) [44]

Gear tooth dedendum is more vulnerable to micropitting especially along the start of active profile (SAP) and the lowest point of single tooth contact (LPSTC). However, micropitting can be observed anywhere in active flanks. Micropitting can be observed only on pinion, only in gear or on both. Generally, gear with rougher surface results micropitting on the mating surface especially if it is harder than the mating surface. Micropitting phenomena gets accelerated if the opposing surface is harder, faster and rougher.

Macropitting or spalling

Macropitting or spalling or flaking is a rolling contact failure mode driven by Hertzian contact stress or other factors (e.g. material condition, lubrication etc.). Macropitting is characterized by sudden and catastrophic material loss. Figure 1.5 shows representative images of macropitting observed in bearings and gears. There is some ambiguity over whether the crack initiation may be either surface or sub surface initiated. Sub surface initiation can occur from the location of the maximum shear stress region in a highly-loaded contact or from sub-surface defects (e.g. crack, void, inclusion etc.). Once a sub-surface crack starts, it usually propagates in the rolling direction and breaks through to the surface.

The preventive measures can be taken to avoid macropitting or spalling are reducing surface stress (proper alignment or load control), improve steel cleanliness, improve oil filtration (to avoid debris), usage of dry and cool lubricants. Generally, pitting appears as shallow craters at contact surfaces with maximum depth of 10 μm. Spalling appears as deeper cavities typically 20-100 μm at contact surface [45].

Figure 1.5: Representative images of macropitting phenomena observed in gears (left) [46] and bearings (right) [47]

One of the main reason behind the obscurity of the terms is probably the physical causes of pitting and spalling have not been established yet. Xu and Sadeghi mentioned when debris pass through a contact region, they generate dents on rolling surface [48]. These work as stress raisers to initiate microcracks which will grow into spalls leading to failure of the machine component. There have been some contact fatigue models developed based on assumption that spalling was a result of surface crack initiation and propagation [49-51]. Way's hypothesis postulates that spalling formation is driven by entrapment of lubricating oil under surface cracks [52]. But experiments conducted by Cheng et. al showed that surface cracks are generally in the range of 5-10 μm and it is impossible to form a large spall cavity unless there is near surface inclusion [53]. Ding described spalling as a sub-surface initiated failure mode [54]. Ding's definition has been well received by some recent studies conducted on spalling [55-57].

White Etching Crack formation

Bearings in heavy industries gearboxes or drive train components (e.g. paper mills, crusher mills, wind turbine gear boxes) are often subjected to a common failure mode called white etching cracks (WEC) or White Structure Flaking (WSF). These cracks are generally

observed in the white etching areas (WEA) on the steel surface. These are called ‘white etching’ because of white appearance of the altered microstructure of a polished and etched sample. Figure 1.6 shows a representative image of failed bearing raceway along with sub-surface WEC network.

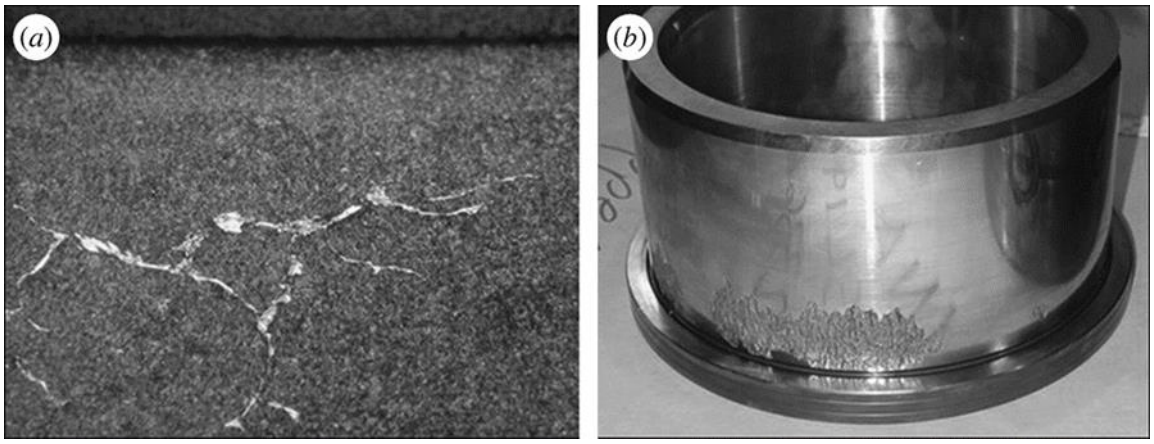

Figure 1.6: Representative image of WEC phenomena observed in wind turbine bearing raceway [58]

Wind turbine gearbox failures are the leading cause of downtime and results significant maintenance costs on wind plant operator and equipment manufacturer [59]. Sheng mentioned in 2014 Wind Turbine Tribology seminar that 64% of all gearbox failures reported to National Renewable Energy Laboratory (NREL) occur due to failures in bearings of the gearboxes with dominant failure mode as WECs. In wind turbines, bearings containing WECs can fail around 5-10% of their design life [60].

WEC affected areas consists of ultrafine, nano-recrystallized grains. These areas appear white under a light microscope due to their low etching response. Bruce et.al had observed WECs attached to MnS inclusions of length 3-45 μm and depths upto 630 μm from the bearing raceway surface [61]. Currently WEC induced failures are not fully understood despite intense research effort [59]. These cracks have been observed to form from

butterfly cracks. Stadler et al. mentioned that there may be several reasons behind observation of white etching layers. These layers can come from phase transformation, steel re-austenitization, scuffing/smearing conditions or electric erosion re-melting. This can also happen due to martensite decay, from material's pre-existing defects or due to adiabatic shear bands (ASBs) [62].

1.2 Research Objectives

To obtain a comprehensive understanding of the role of retained austenite on the tribomechanical behavior of AISI 8620 steel under boundary lubrication (low lambda) conditions. AISI 8620 steel is commonly used in drivetrain components such as gears and bearings.

The whole study can be divided into two broad objectives: (1) Investigate the effect of process conditions on RA generation and wear and (2) Investigate the effect of RA on rolling contact fatigue. Figure 1.7 illustrates the organization of the specific research tasks and organization of the dissertation. The specific objective with respect to each of these parts are mentioned below:

(1a) Investigate the effect of different conventional heat treatment parameters on RA generation of carburized steel.

(1b) Investigate the effect of conventional heat treatment parameters on tribo-mechanical properties such as microhardness, residual stress, friction and abrasive wear behavior of carburized steel.

(1c) Study the potential of laser heat treatment technique as a non-conventional way to vary RA on steel.

(1d) Investigate the effect of laser scanning velocity and shielding gases on tribo-mechanical property of steel in terms of microhardness, surface temperature generation, microstructural alteration, friction and abrasive wear behavior.

Experience and understanding gained from the first phase studies were used to inform second set of studies to observe the effect of RA on crucial RCF failure modes. The objectives for these group of studies are mentioned below:

(2a) Investigate the effect of varying carbon potential and tempering parameters on RA generation of heat treated steel.

(2b) Observe the effect of RA on micropitting failure mode of carburized steel under boundary lubrication.

(2c) Formulate novel protocol to quantize micropitting on test samples and capture martensitic phase transformation during RCF tests.

(2d) Find correlation between surface roughness parameters and micropitting during RCF tests.

(2e) Investigate the effect of RA on macropitting or spalling behavior of carburized steel under boundary lubrication.

(2f) Investigate the effect of RA on white etching crack (WEC) morphology of carburized steel under boundary lubrication.

1.3 Broader Impacts

Observing the above-mentioned failure modes for different RA samples should contribute significantly to the existing literatures on drivetrain components. The study is expected to establish the role of RA on abrasive wear, micropitting, macropitting and WEC formation in the context of other mechanical and microstructural phenomena as well as the correlation

of behavior to heat treatment routes for preferred fatigue and abrasive wear life. The present study has broad-based implications for the energy sector. An optimum level of RA resulted from a planned heat treatment scheme can be helpful to avert premature gear failure. Railway wheels can't meet strict demands of rolling contact wear and fatigue resistance due to rising speed and weight of traffic. WEC formation in bearings of wind turbine gearbox is one of the major issue observed in non-renewable energy sector. Although several researchers speculated about role of RA on WEC, but there is no scientific observation made in this area till date. Overall, the findings will provide valuable input for the design and manufacturing of drivetrain components for a wide range of applications ranging from agricultural equipment to the wind energy sectors.

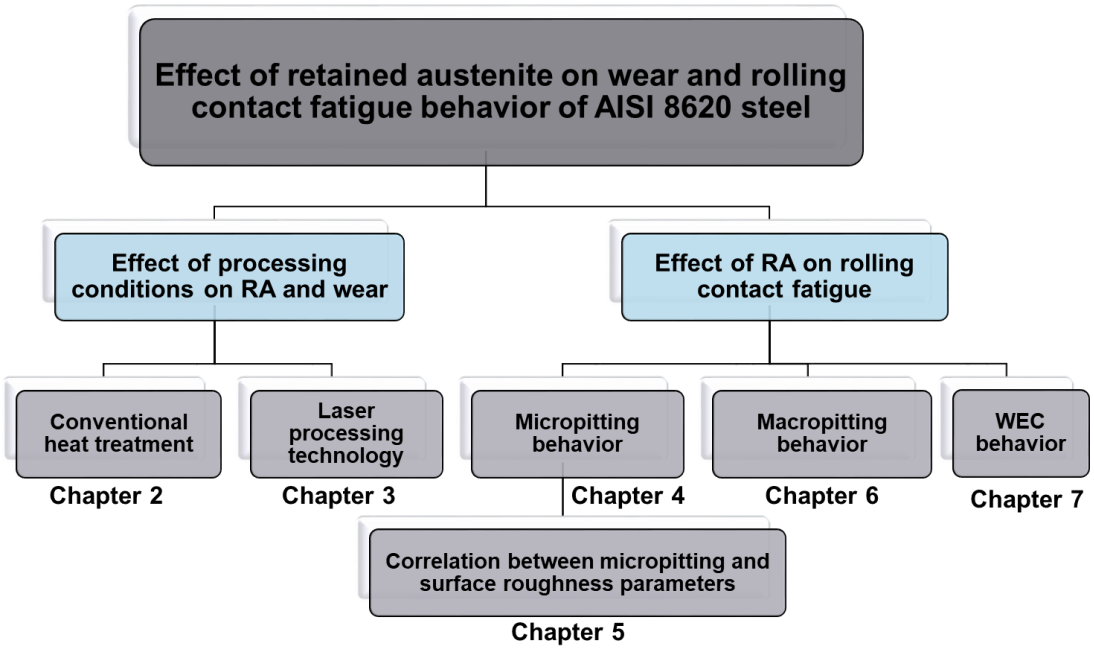

Figure 1.7: Outline of research objectives

1.4 Thesis Organization

Figure 1.7 shows the research objectives along with the chapters in which the discussions regarding each objective are organized. Following this introductory chapter, chapter 2 discusses the effect of different conventional heat treatment parameters on RA and tribomechanical properties of steel. In chapter 3, the effect of scanning velocity and shielding gases during laser heat treatment are studied on RA, microstructure, hardness and tribological behavior of steel. In chapter 4, the effect of RA on micropitting behavior is elucidated. Correlation between surface roughness parameters and micropitting are discussed in chapter 5. The effect of RA on macropitting behavior is explained in chapter 6. Interlaying mechanisms on WEC formation for different RA samples are discussed in chapter 7. In chapter 8, conclusions from different chapters are listed. Experimental instruments and methods used related to each study are mentioned in the respective chapters.

1.5 References

1. Kim, S.Y., S. Kubota, and M. Yamanaka, *Application of CAE in cold forging and heat treatment processes for manufacturing of precision helical gear part.* Journal of Materials Processing Technology, 2008. **201**(1-3): p. 25-31.

2. Ferguson, B.L., Z. Li, and A.M. Freborg, *Modeling heat treatment of steel parts.* Computational Materials Science, 2005. **34**(3): p. 274-281.

3. Atraszkiewicz, R., et al., *High pressure gas quenching: Distortion analysis in gears after heat treatment.* Materials Science and Engineering a-Structural Materials Properties Microstructure and Processing, 2012. **558**: p. 550-557.

4. Cho, J.R., et al., *Distortions induced by heat treatment of automotive bevel gears.* Journal of Materials Processing Technology, 2004. **153**: p. 476-481.

5. Matlock, D.K., et al., *Surface Processing to Improve the Fatigue Resistance of Advanced Bar Steels for Automotive Applications.* Materials Research, 2005. **8**: p. 453-459.

6. Harmer, S. *Heat Treatment of Steels-The Processes*. 2001; Available from: http://www.azom.com/article.aspx?ArticleID=543.

7. Siepak, J., *The Influence of Contact Stress on the Wear of a Carburized Steel Case with a High Content of Retained Austenite.* Wear, 1982. **80**(3): p. 301-305.

8. Asi, O., et al., *The relationship between case depth and bending fatigue strength of gas carburized SAE 8620 steel.* Surface & Coatings Technology, 2007. **201**(12): p. 5979-5987.

9. Scheuer, C.J., et al., *Low temperature plasma carburizing of martensitic stainless steel.* Materials Science and Engineering a-Structural Materials Properties Microstructure and Processing, 2012. **539**: p. 369-372.

10. Scheuer, C.J., et al., *Low-temperature plasma carburizing of AISI 420 martensitic stainless steel: Influence of gas mixture and gas flow rate.* Surface & Coatings Technology, 2012. **206**(24): p. 5085-5090.

11. Krauss, G., *Microstructure and Fracture of a Carburized Steel.* Metallurgical Transactions a-Physical Metallurgy and Materials Science, 1978. **9**(11): p. 1527-1535.

12. Parrish, G., *Carburizing: Microstructures and properties.* Heat Treatment of Metals, 2000. **27**(2): p. 38-38.

13. Kim, H.J. and Y.G. Kweon, *The effects of retained austenite on dry sliding wear behavior of carburized steels.* Wear, 1996. **193**(1): p. 8-15.

14. Roy, S. and S. Sundararajan, *The effect of heat treatment routes on the retained austenite and Tribomechanical properties of carburized AISI 8620 steel.* Surface & Coatings Technology, 2016. **308**: p. 236-243.

15. Colaco, R. and R. Vilar, *On the influence of retained austenite in the abrasive wear behaviour of a laser surface melted tool steel.* Wear, 2005. **258**(1-4): p. 225-231.

16. Roy, S., et al., *Effect of laser treatment parameters on surface modification and tribological behavior of AISI 8620 steel.* Tribology International, 2017. **112**: p. 94-102.

17. Zhao, Y., et al., *Effects of Overlapping Distances on Steel Microstructure and Properties After Multi-track Laser Quenching.* Journal of Materials Engineering and Performance, 2017. **26**(12): p. 5973-5982.

18. Bakhsheshi-Rad, H.R., et al., *Effect of Multi-Step Tempering on Retained Austenite and Mechanical Properties of Low Alloy Steel.* Journal of Iron and Steel Research International, 2011. **18**(12): p. 49-56.

19. Kumar, R., R.K. Behera, and S. Sen, *Effect of Tempering Temperature and Time on Strength and Hardness of Ductile Cast Iron.* 4th National Conference on Processing and Characterization of Materials, 2015. **75**.

20. Bensely, A., et al., *Effect of cryogenic treatment on tensile behavior of case carburized steel-815M17.* Materials Characterization, 2007. **58**(5): p. 485-491.

21. Bensely, A., et al., *Effect of cryogenic treatment on distribution of residual stress in case carburized En 353 steel.* Materials Science and Engineering a-Structural Materials Properties Microstructure and Processing, 2008. **479**(1-2): p. 229-235.

22. Das, D., et al., *Influence of sub-zero treatments on fracture toughness of AISI D2 steel.* Materials Science and Engineering a-Structural Materials Properties Microstructure and Processing, 2010. **528**(2): p. 589-603.

23. Coronado, J.J. and A. Sinatora, *Abrasive wear study of white cast iron with different solidification rates.* Wear, 2009. **267**(11): p. 2116-2121.

24. Li, C.G., et al., *Influence of Carbon Content of Martensitic Matrix and Retained Austenite on Wear of Martensitic Ductile Iron.* Wear, 1993. **162**: p. 75-82.

25. Xi, J.T., et al., *Influence of Retained Austenite on the Wear-Resistance of High Chromium Cast-Iron under Various Impact Loads.* Wear, 1993. **162**: p. 83-88.

26. Abareshi, M. and E. Emadoddin, *Effect of retained austenite characteristics on fatigue behavior and tensile properties of transformation induced plasticity steel.* Materials & Design, 2011. **32**(10): p. 5099-5105.

27. Jeddi, D. and H.P. Lieurade, *Effect of retained austenite on high cycle fatigue behavior of carburized 14NiCr11 steel.* Fatigue 2010, 2010. **2**(1): p. 1927-1936.

28. Hu, Z.Z., et al., *The effect of austenite on low cycle fatigue in three-phase steel.* International Journal of Fatigue, 1997. **19**(8-9): p. 641-646.

29. Gahr, K.-H.Z., *Microstructure and Wear of Materials*. Tribology Series. Vol. 10. 1987: Elsevier.

30. Sotres, J. and T. Arnebrant, *Experimental Investigations of Biological Lubrication at the Nanoscale: The Cases of Synovial Joints and the Oral Cavity.* Lubricants, 2013. **1**(4): p. 102-131.

31. Dommarco, R.C., et al., *Residual stresses and retained austenite evolution in SAE 52100 steel under non-ideal rolling contact loading.* Wear, 2004. **257**(11): p. 1081-1088.

32. Shen, Y., et al., *Effect of retained austenite - Compressive residual stresses on rolling contact fatigue life of carburized AISI 8620 steel.* International Journal of Fatigue, 2015. **75**: p. 135-144.

33. D'Errico, F., *Micropitting Damage Mechanism on Hardened and Tempered, Nitrided, and Carburizing Steels.* Materials and Manufacturing Processes, 2011. **26**(1): p. 7-13.

34. Mahmoudi, B., et al., *Influence of a WC/a-C:H Coating on Micropitting Wear of Bearing Steel.* Tribology & Lubrication Technology, 2015. **71**(4): p. 24-27.

35. Rivero, I.V. and C.O. Ruud, *Deviation of residual stress patterns in 52100 bearing steel due to inherent microstructural transformations after rolling contact.* Materials Characterization, 2004. **53**(5): p. 381-393.

36. Bakoglidis, K.D., et al., *Rolling performance of carbon nitride-coated bearing components in different lubrication regimes.* Tribology International, 2017. **114**: p. 141-151.

37. Soltanahmadi, S., et al., *Investigation of the effect of a diamine-based friction modifier on micropitting and the properties of tribofilms in rolling-sliding contacts.* Journal of Physics D-Applied Physics, 2016. **49**(50).

38. Moallem, H., S. Akbarzadeh, and A. Ariaei, *Prediction of micropitting life in spur gears operating under mixed-lubrication regime using load-sharing concept.* Proceedings of the Institution of Mechanical Engineers Part J-Journal of Engineering Tribology, 2016. **230**(5): p. 591-599.

39. Wei, J., A.Q. Zhang, and P. Gao, *A study of spur gear pitting under EHL conditions: Theoretical analysis and experiments.* Tribology International, 2016. **94**: p. 146-154.

40. Soltanahmadi, S., et al., *Tribochemical study of micropitting in tribocorrosive lubricated contacts: The influence of water and relative humidity.* Tribology International, 2017. **107**: p. 184-198.

41. Martini, A.; Available from: http://faculty2.ucmerced.edu/amartini/tribology.shtml.

42. Kissling, U., *Application of the First International Calculation Method for Micropitting*. 2012: Gear Technology. p. 54-60.

43. Errichello, R.L. *Morphology of Micropitting*. 2012. 74-81.

44. *Preventing Micropitting and Surface Fatigue*. Machinery Lubrication Available from: http://www.machinerylubrication.com/Read/29276/micropitting-surface-fatigue.

45. Ding, Y. and J.A. Gear, *Spalling depth prediction model.* Wear, 2009. **267**(5-8): p. 1181-1190.

46. Kuhnell, B.T. *Wear in Rolling Element Bearings and Gears - How Age and Contamination Affect Them*. Available from: http://www.machinerylubrication.com/Read/664/wear-bearings-gears.

47. Leone, T. *Modifying Gears for Taller Overdrive*. 2008; Available from: https://sites.google.com/site/diyoverdrive/durability-failure.

48. Xu, G. and F. Sadeghi, *Spall initiation and propagation due to debris denting.* Wear, 1996. **201**(1-2): p. 106-116.

49. Kudish, I.I., *A new statistical model of contact fatigue.* Tribology Transactions, 2000. **43**(4): p. 711-721.

50. Tallian, T.E., *Spalling Life Model with Relaxed Distribution Constraints, for Rough Hertz Line Contacts.* Journal of Tribology-Transactions of the Asme, 1993. **115**(3): p. 453-459.

51. Blake, J.W. and C.F. Draper, *Further Development of a Predictive Pitting Model for Gears - Improvements in the Life Prediction Analysis.* Tribology Transactions, 1994. **37**(2): p. 237-244.

52. Way, S., *Pitting due to rolling contact.* Journal of Appllied Mechanics, 1935. **57**: p. A49-A58.

53. Cheng, H.S., L.M. Keer, and T. Mura, *Analytical modelling of surface pitting in simulated gear-teeth contacts.* SAE Technical Paper, 1984: p. 4.987–4.995.

54. Ding, Y. and N.F. Rieger, *Spalling formation mechanism for gears.* Wear, 2003. **254**(12): p. 1307-1317.

55. Raje, N., F. Sadeghi, and R.G. Rateick, *A statistical damage mechanics model for subsurface initiated spalling in rolling contacts.* Journal of Tribology-Transactions of the Asme, 2008. **130**(4).

56. Santus, C., et al., *Surface and subsurface rolling contact fatigue characteristic depths and proposal of stress indexes.* International Journal of Fatigue, 2012. **45**: p. 71-81.

57. Choi, Y. and C.R. Liu, *Spall progression life model for rolling contact verified by finish hard machined surfaces.* Wear, 2007. **262**(1-2): p. 24-35.

58. Kotzalas, M.N. and G.L. Doll, *Tribological advancements for reliable wind turbine performance.* Philosophical Transactions of the Royal Society a-Mathematical Physical and Engineering Sciences, 2010. **368**(1929): p. 4829-4850.

59. Gould, B. and A. Greco, *The Influence of Sliding and Contact Severity on the Generation of White Etching Cracks.* Tribology Letters, 2015. **60**(2).

60. Sheng, S., *Gearbox Reliability Database: Yesterday, Today, and Tomorrow (Presentation)*. 2014: National Renewable Energy Laboratory (NREL), Golden.

61. Bruce, T., et al., *Characterisation of white etching crack damage in wind turbine gearbox bearings.* Wear, 2015. **338**: p. 164-177.

62. Stadler, K., J. Lai, and R. Vegter, *A Review: The Dilemma With Premature White Etching Crack (WEC) Bearing Failures.* Bearing Steel Technologies: 10th Volume, Advances in Steel Technologies for Rolling Bearings, ASTM International, , 2015. **487-508**.

CHAPTER 2. THE EFFECT OF HEAT TREATMENT ROUTES ON THE RETAINED AUSTENITE AND TRIBOMECHANICAL PROPERTIES OF CARBURIZED AISI 8620 STEEL

Modified from a paper published in *Surface and Coatings technology*

Sougata Roy and Sriram Sundararajan

2.1 Abstract

The objective of this study is to investigate the effect of heat treatment routes involving carburizing and quenching technique on the tribological behavior of carburized AISI 8620 steel. This particular material is commonly used in drivetrain components and undergoes sliding or rolling under high contact pressure conditions. Different levels of retained austenite (RA), hardness and residual stress were achieved by varying carbon potential (0.45% to 1.05%) during carburizing as well as by employing different end-quenching routes (from air-cooled to deep freezing). Wear tests were carried out using a ball on flat reciprocating micro-tribometer between a diamond probe and the samples under dry sliding conditions. Samples were subsequently analyzed using non-contact profilometry and field emission scanning electron microscopy to observe wear behavior and elucidate mechanisms. Hardness and RA had comparatively significant effect on wear resistance as compared to residual stress. It was observed that beyond a certain limiting Hertzian contact pressure level, higher carbon potential carburized sample resulted in increased abrasive wear resistance. This increased wear resistance is attributed to the higher hardness and conditions conducive to transformation of RA into martensite via ploughing-induced work-hardening. The findings indicate that surface

treatments resulting in a combination of high hardness and moderately high RA levels result in enhanced abrasive wear resistance for AISI 8620 steel.

2.2 Introduction

Drivetrain components manufactured from steel are one of the most crucial components in machinery. Enhancing the operational life and reliability of these components via heat treatment routes is a long-studied topic of research, both via experiments and computational modelling [1-5]. Depending upon the type of steel being used for a particular component and its application, five heat treatment routes are most popularly used. These are carburizing, carbo-nitriding, nitriding, nitro-carburizing and boronizing [6]. Carburizing is a popular technique used for low carbon steels at temperatures between 850-950°C where carbon is diffused to iron or steel surface layer typically resulting in increased hardness, residual stress and fatigue/tensile strength. By varying parameters during the carburizing and any subsequent quenching processes, the resulting attributes of the material such as hardness, residual stress, amount of residual austenite (RA), microstructure, grain size, grain orientation etc. can be varied [7-12].

While the effect of hardness and residual stress on the resulting tribological properties of the steel is well known, the effect of retained austenite (RA) is not as clearly understood [7, 8, 13-20]. Siepak [7] utilized thermal treatment to obtain varying RA% in carburized 12HN3A steel samples and observed that RA had a beneficial effect on wear resistance for a contact pressure between 300-1400 MPa, a rolling-sliding (10%) condition and for specimens with comparatively lower hardness range. Li et al. [15] followed two different routes to get samples with different RA%, one by changing austenitization temperature and other by quenching temperature. He conducted impact wear test and reported that RA

has no effect on wear resistance with hard abrasives while showing a positive effect with soft abrasives whereas other studies [21] showed results contrary to Li's observation. Kim and Kweon [16] reported that as the RA% in carburized steels increased from 6 to 30%, the wear resistance decreased while beyond 30 % the wear resistance increased with an increase in RA under dry sliding conditions. They also observed that samples with higher RA% exhibited higher hardness, which is contrary to Siepak's [7] observation where he had shown 40% RA samples showing significantly lower hardness than samples with only martensitic microstructure. These studies suggest that it is often challenging to separate the effect of RA from the effect of other parameters (e.g. hardness) on the resulting tribological behavior. Thus, there is a need to better understand the impact of heat treatment routes on steels and the affect that the heat treatment may have on the resulting tribological behavior, especially in the context of the amount of retained austenite.

In this study, AISI 8620 steel samples were subjected to several carburizing and end quenching schemes to vary the amount of retained austenite. The resulting samples were examined for retained austenite, hardness and residual stresses. Dry sliding tests were conducted to evaluate the friction and wear behavior. Correlations between the retained austenite, hardness and residual stresses with the observed behavior are discussed and prevailing wear mechanisms are identified.

2.3 Materials

This study focused on AISI 8620 steel, an alloy steel used widely for carburized parts where hardened case is desired for wear resistance. This particular steel is very commonly used in gears, ring gears, shafts and crank shafts. The chemical composition of

AISI 8620 is given in Table 2.1. For this study, circular discs were cut from a long bar of AISI 8620 steel (EMJ Metals). Both disc surfaces were CNC milled followed by surface grinding to minimize surface roughness prior to heat treatment. A Zygo NewView 7100 non-contact profilometer was used to measure the surface roughness of the samples. All samples exhibited an average surface roughness (Ra) in the range of 0.5-0.7 μm over a scan size of 0.47 mm ×0.35 mm.

Table 2.1: Composition of AISI 8620 steel [22]

Component	Wt%
C	0.18-0.23
Cr	0.4-0.6
Fe	96.9-98.02
Mn	0.7-0.9
Mo	0.15-0.25
Ni	0.4-0.7
P	Max 0.035
S	Max 0.04
Si	0.15-0.35

The heat treatment schemes utilized in this study are outlined in Figure 2.1. There were two different routes taken to vary the amount of retained austenite. The first route involved changing carbon potential during carburizing from 0.45% to 1.05% (Sample sets B and A respectively) and the second involved incorporating an additional deep-freezing step (sample set C).

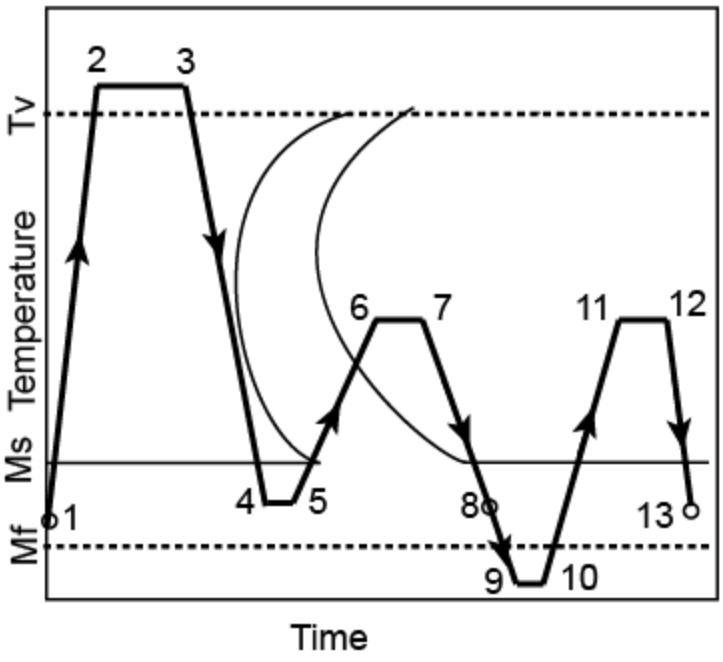

Sample	Path	Steps	Temperature & time	C Pot-ential
A	1-8	Carburizing 925º C,4hrs (2-3) Quenching 70ºC, 20min (4-5) Tempering 150ºC, 2hrs (6-7)		1.05
B	1-8			0.45
C	1-13	Above steps + deep freeze -40ºC, 1hr (9-10)+ Second tempering (11-12)		0.45
D	Non-heat treated			

Figure 2.1: Heat treatment schemes used to generate samples with different retained austenite (RA) % (T_v= Austenitization temperature; M_s=Martensite start temperature; M_f=Martensite finish temperature)

For sample C a second tempering step followed deep-freezing. The endothermic carburizing atmosphere consists of carburizing gases (CH_4 and CO) and decarburizing gases (CO_2 and H_2O). All samples were carburized for four hours at a specific carbon

potential level. In particular, increasing carbon potential during carburizing is known to increase RA% [23], while the use of different end-quenching routes (from air-cooled to deep freezing) decreases RA%. Therefore, the use of these combined techniques helped to get samples with RA% from 15 to 3.5%. The transformation of austenite to martensite is hindered when carbon potential is increased during carburizing which results in higher RA. Similarly, deep freezing creates a high quench rate, which increases the transformation rate from austenite to martensite.

2.4 Methods

2.4.1 Measurement of Retained Austenite (RA)

X-ray diffraction (XRD) is one of the most important techniques used to accurately quantify the amount of RA [24-26]. In this study, a Siemens D 500 X-ray diffractometer with a diffracted beam monochromator was used to quantify RA percentage of the samples after heat treatment. A Cu Kα target was used (wavelength 0.15418 nm) with a target voltage of 40 kV and current 30 mA. XRD scan data for a range of 32 to 86 degrees (2θ angle) was analyzed using TOPAS software to determine the amount of RA in those samples. TOPAS uses the Rietveld method which helps to fit theoretical data to a measured pattern using analytical profile functions & least square methods [27]. Some studies calculate and report the RA% while ignoring the amount of magnetite or other phases present in the sample [16] while others include magnetite in the calculations [28]. In this case RA% was calculated including the presence of third phase (magnetite) in the samples. XRD measurements were conducted on three samples for each heat treatment route (A, B, C) and untreated (D) condition.

2.4.2 Micro-hardness and Residual stress tests

Heat treatment influences surface hardness of steel, which in turn impacts its wear resistance behavior. Hardness of the samples were evaluated using a Leco LM247AT microhardness tester with a Vicker's diamond indenter and associated Amh43 software. Five measurements at a load of 1 Kgf (9.81 N) were made on each sample and mean of those measurements were calculated and reported along with a 95% confidence interval.

Heat treatment processes can also influence the residual stress which in turn influence tribological behavior. Residual stresses were measured using X-ray diffraction. In order to do this, strain in the crystal lattice was first determined and associated residual stress was calculated from the elastic constants [29-31]. The relation between changes in inter-planer spacing (d_n) and magnitude of surface residual stress (σ) for steel samples can be shown as:

$$\sigma = \frac{E}{(1+\nu)Sin^2\psi}\frac{(d_n - d_0)}{d_0} \tag{2.1}$$

where, E is Young's modulus of steel, ν is Poisson's ratio, ψ is the tilt angle, d_n are the inter-planer spacing of the corresponding diffraction peak measured at each tilt angle and d_0 is the stress-free lattice spacing.

The crystallographic distance was found according to crystallographic chart reference code 00-006-0696 for cubic Fe (metal) corresponding to (310) plane provided by ICDD-PDF (International Committee for Diffraction Data-Powder Diffraction Files). The elastic modulus and Poisson's ratio of iron was taken as 205 GPa and 0.3 respectively [22] for

all the calculations. Diffraction data was collected at four different tilt angles for each sample and three repetitions were conducted to find the mean value of residual stress.

2.4.3 Micro-scale friction & wear tests

Friction and wear tests were conducted using a custom-built reciprocating ball-on-flat microtribometer that can produce a microscale (apparent area ~1000 μm^2) multi-asperity contact. A schematic of its major components is shown in Figure 2.2. A desired probe of specific radius is placed at the end of a crossed I-beam structure, which is lowered using a linear stage to apply a desired normal load to the sample. The normal and the friction (lateral) forces are measured using semiconductor strain gages on the cantilevers. Friction forces can be resolved to approximately ±5 mN and normal forces to approximately ±15 mN. The signal from the normal load is monitored and used in a simple proportional-integral (PI) feedback loop to maintain the desired normal force regardless of any slope or waviness in the surface of the sample. The desired sample is affixed to another stage set perpendicular to the beam, which provides linear motion.

Coefficient of friction between the samples and a spherical AISI 52100 steel probe (radius of 2 mm and hardness around 60 HRc) with an average Ra surface roughness 0.005 μm (over a a scan size of 0.47×0.35 mm) was determined from a ramped load test. Here the applied normal load was increased linearly from 0 to 200 mN (max contact pressure 500 MPa) for a specific sliding distance of 20 mm at a speed of 1 mm/s while the lateral force was recorded. A linear fit to the lateral force data plotted against normal load provided the coefficient of friction.

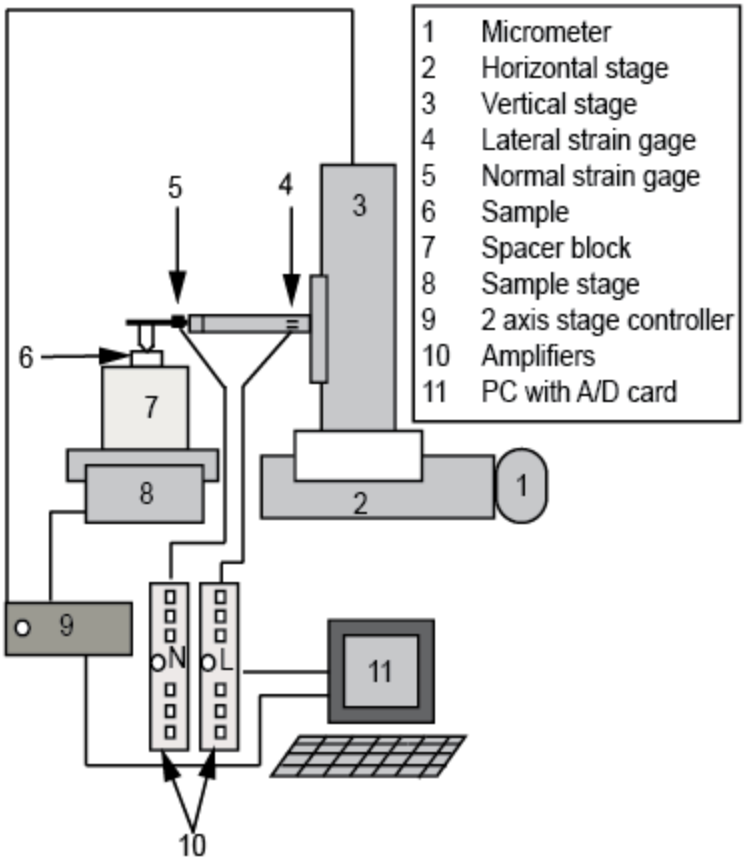

Figure 2.2: Schematic of reciprocating microtribometer used for friction and wear tests

Next, reciprocating sliding tests were conducted against a diamond probe (conical tip with a radius of 75 μm, (Bruce Diamond Corporation) for 750 cycles with a stroke speed of 5 mm/s at constant load. Tests were conducted at various normal loads (180 mN, 260 mN and 350 mN) to study effect of contact pressure on the wear response. All friction and wear tests were conducted under dry sliding conditions. Three repetitions were conducted for each test condition on each sample.

Wear track depths were measured using a non-contact surface profilometer (Zygo NewView 7100). Wear depth was measured at four regions along each wear track. To get an accurate and representative wear depth, at each region, three rectangular zones

(areas) were created where the wear track zone was assigned as the test region and the zones adjacent to the wear track on either side were assigned as the reference region. The test zone's average height was subtracted from reference zone's average height to get an averaged wear depth between wear track zone and its neighborhood zone.

An FEI Quanta-250 Scanning Electron Microscope (FESEM) was used to obtain high resolution images of wear tracks and an Oxford Aztec energy-dispersive x-ray analysis was used to perform elemental mapping of the wear track and adjacent regions.

2.5 Results & discussion

2.5.1 Effect of heat treatment on RA%

Figure 3 shows the measured RA percentages on the heat-treated samples. As shown in Figure 2.1, an RA range of 3 to 15 % was observed for our samples. In addition to austenite and martensite, all carburized samples showed small amount of magnetite (Iron oxide) which is very common for carburized samples. Sample A shows the maximum RA of 15%. The high carbon potential used during carburizing hinders transformation of austenite to martensite during cooling and resulting higher RA% in that sample. This result has also been observed previously by Kim and Kweon [16]. In case of samples B and C, the extra hour of deep-freezing cycle in dry ice resulted in a slight decrease in RA (from 6 to 3.5%). This is consistent with findings by other researchers [32, 33] on the effect of cryogenic treatment on microstructure. Thus, a wide range of RA was obtained with 15% for sample A to 3% for the non-carburized sample (Sample D). Although sample D was non-carburized and prepared from raw material (cold drawn AISI 8620 steel bar), a small amount (~3%) of RA didn't transform during the cold finishing operation.

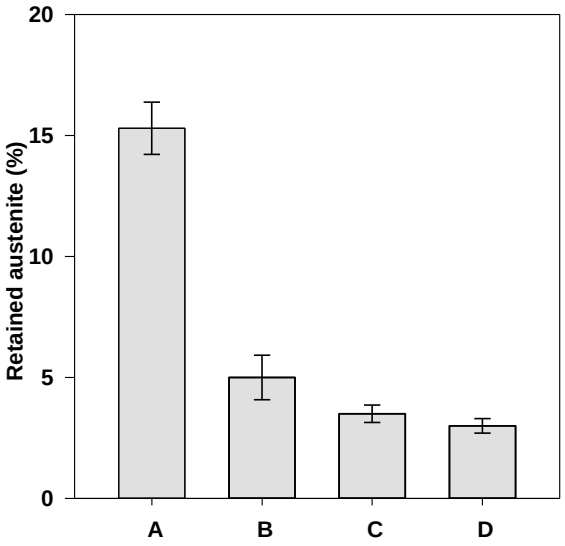

Figure 2.3: Effect of heat treatment on retained austenite (RA) % in samples. Mean values of three samples from each batch are shown. Error bars represent 95% confidence intervals.

Carbon content underneath surface was measured using EDAX X-ray microanalyser [34] equipped with EDS for both sample A and sample C at an accelerating voltage 10 kV. Initially, real carbon content standards were used to calibrate the equipment. It was observed the maximum carbon weight% on surface for sample A and sample C was approx. 0.9% and 0.6% respectively. Surface carbon content for sample A is similar to the observation by Rowan and Sisson [35] for AISI 8620 steel carburized with 1.1%C potential. Higher carbon weight percentage on surface was resulted due to higher carbon potential used for sample A compared to sample C. Carbon percentage dropped close to 0.2 wt.% at a depth of around 1.2 mm from surface for both samples.

2.5.2 Effect of heat treatment on microhardness

Figure 2.4 shows microhardness values exhibited by the various samples. As one would expect, Sample A, B and C exhibited higher hardness compared to sample D due to carburizing. Sample A showed higher hardness than samples B and C.

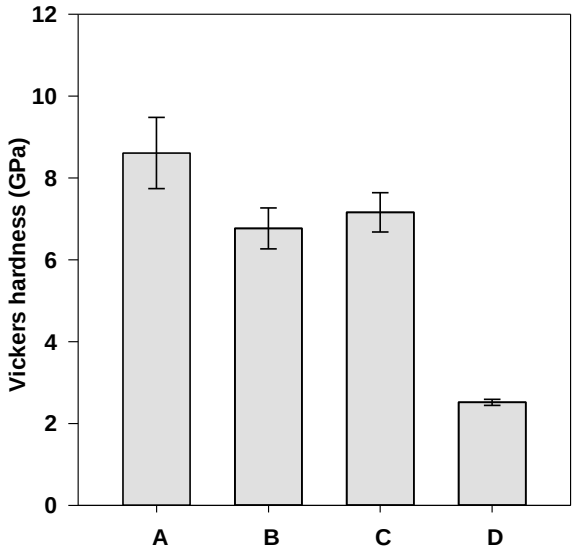

Figure 2.4: Effect of heat treatment on microhardness. Mean values from five measurements are shown. Error bars represent 95% confidence intervals

The higher hardness exhibited by Sample A is attributed to the application of higher carbon potential during carburizing compared to other samples resulting in increased carbon content. Sample C shows a slightly higher hardness compared to sample B, which is attributed to the added quenching undergone by sample C. It appears that deep cryogenic quenching with more quenching time can significantly affect the hardness as shown by Liu et al. [36]. If both heat treatment techniques are compared in our study, varying carbon potential shows more significant effect on hardness improvement than varying end quenching.

2.5.3 Effect of heat treatment on residual stress

Figure 2.5 shows the magnitude of the residual stresses of the samples as evaluated by X-ray diffraction. All samples exhibited a compressive residual stress and negligible shear strain. The carburizing technique generated additional compressive residual stress on sample A, B and C which is generally beneficial for wear resistance.

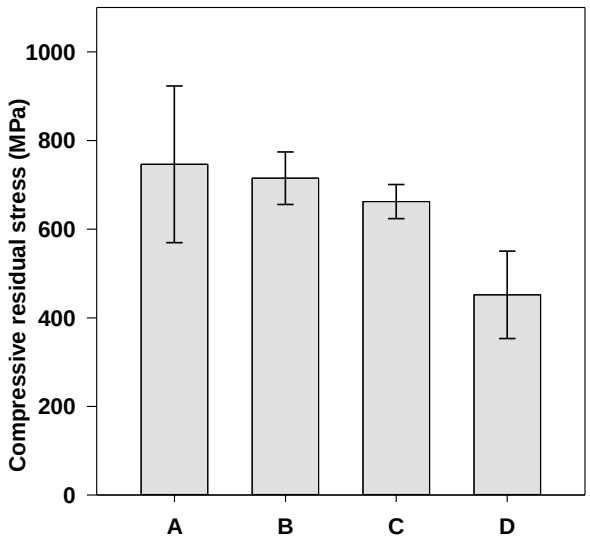

Figure 2.5: Calculated residual stresses for the samples using XRD at four different tilt angles. Mean values from three repetitions of residual stress measurements are shown. Error bars represent 95% confidence intervals.

From Figure 2.5 it can be observed that sample A and B exhibited slightly higher residual stress compared to sample C. This supports the finding by Bensely et al [33] that cryogenically treated steel subjected to tempering (similar to sample C) results in a reduction in compressive residual stress due to better thermodynamic stability and lattice relaxation. From the mean residual stress values, there is a weak decreasing trend of residual stress with decreasing RA% suggesting a mild correlation. As a comparison,

Kim and Kweon [16], found no significant correlation between initial RA% and residual stress levels for AISI 8620 steel.

2.5.4 Effect of heat treatment on friction and wear

The microscale friction tests resulted in very comparable coefficient of friction values for all the samples (~ 0.1) indicating that the heat treatment has negligible effect on the interfacial friction behavior under dry sliding. The friction coefficient was lower than the values observed in other studies [37, 38] primarily due to differences in sliding distance and contact pressures. Thus, the reason behind getting lower friction for present case is most likely due to the fact that fully adhered junctions was yet to form given the relatively low pressure and sliding distance. In addition, relative humidity most likely played a role, contributing to form a thin water film that helped to reduce friction coefficient. There was no surface damage observed after the friction tests indicating that the tests were most likely conducted in adhesive regime.

The resulting wear depths from the reciprocating wear tests against the diamond probe under different loads (contact pressure) are shown in Figures 2.6 a and b. Hertzian contact stresses for each loading conditions were calculated based on empirical relation of ball on flat contact condition. Tests were conducted at maximum hertz pressure ranging from 5.2 to 7.9 GPa. Data for maximum contact pressures of 6 to 7.5 GPa (corresponding loads of 180 mN to 350 mN respectively) are shown for discussion. For all samples, at 6 GPa and lower pressures, the wear track depths were low and exhibited no significant trend across the samples. Figure 2.6a shows the wear track depths for the samples as a function of contact pressure. At contact pressure of 6.8 and 7.5, sample A showed better wear resistance compared to other carburized samples. The finding

indicates that the combined effect of high hardness and higher retained austenite helped to show better wear resistance at higher contact stress condition. This finding supports Siepak's [7] claim that beyond a limiting hertz stress condition higher RA sample should show better wear resistance because the RA in the microstructure inhibits crack nucleation and propagation. Sample B and sample C had comparable wear resistance since they had comparatively lower hardness and RA. Since sample D was non-carburized, its wear resistance was much poorer than the other carburized samples.

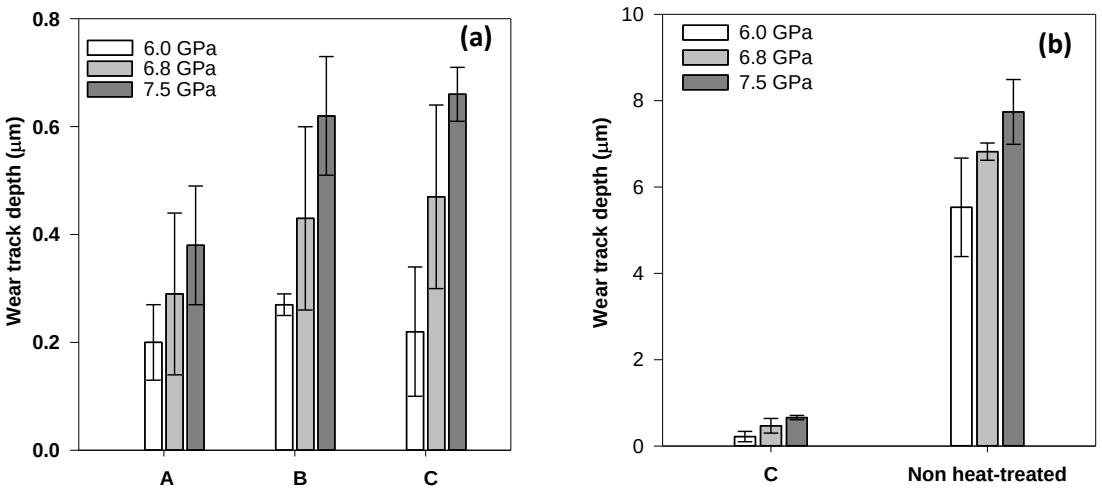

Figure 2.6: (a) Wear track depth on carburized samples at various contact pressures. (b) Wear track depth comparison between carburized and non-carburized samples. Mean values from three repetitions of wear tests are shown. Error bars represent 95% confidence intervals.

In order to understand the wear mechanisms, the wear tracks were analyzed using field emission scanning electron microscopy. Figures 2.7 and 2.8 show representative images of the wear tracks generated at contact pressures of 6 and 7.5 GPa respectively. From the images, it is clear that abrasive wear is the most dominant wear mode in all cases. At the

lower contact pressure of 6 GPa (Figure 2.7), there is pile up of materials on the two sides of wear track region for all heat-treated samples, which is indicative of micro-ploughing.

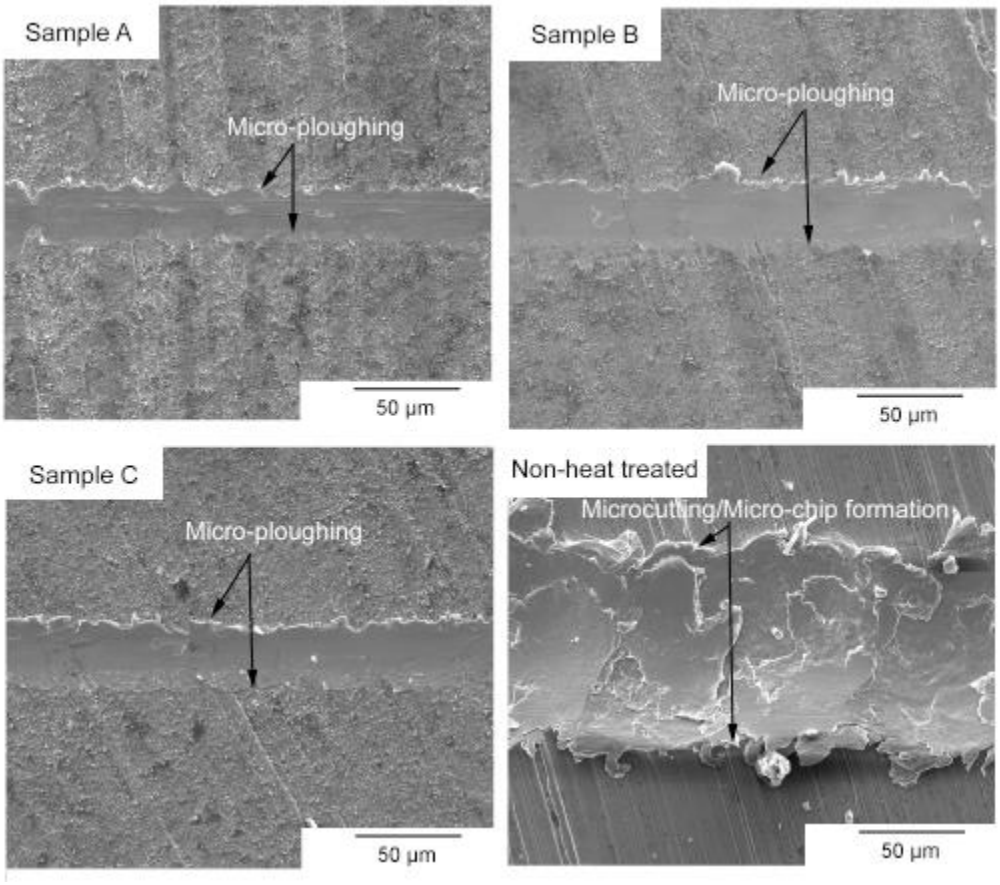

Figure 2.7: Field Emission Scanning Electron Microscope (FESEM) images of wear tracks from sliding tests against a diamond probe at 6 GPa contact stress condition. Prominent features indicating dominant wear mechanisms are highlighted.

At a contact pressure of 7.5 GPa (Figure 2.8), the wear track width for sample A was less than that of sample B and C. This is consistent with the lower wear depths measured for Sample A compared to sample B and C at this contact pressure. At the contact pressure of 7.5 GPa, samples B and C exhibit significant serrations at the wear track edges compared to sample A. At this contact pressure, the main abrasive wear mechanism for sample B

and C appear to be a mixture of wedge formation and micro-ploughing while for sample A, micro-ploughing remains to be the dominating wear mechanism.

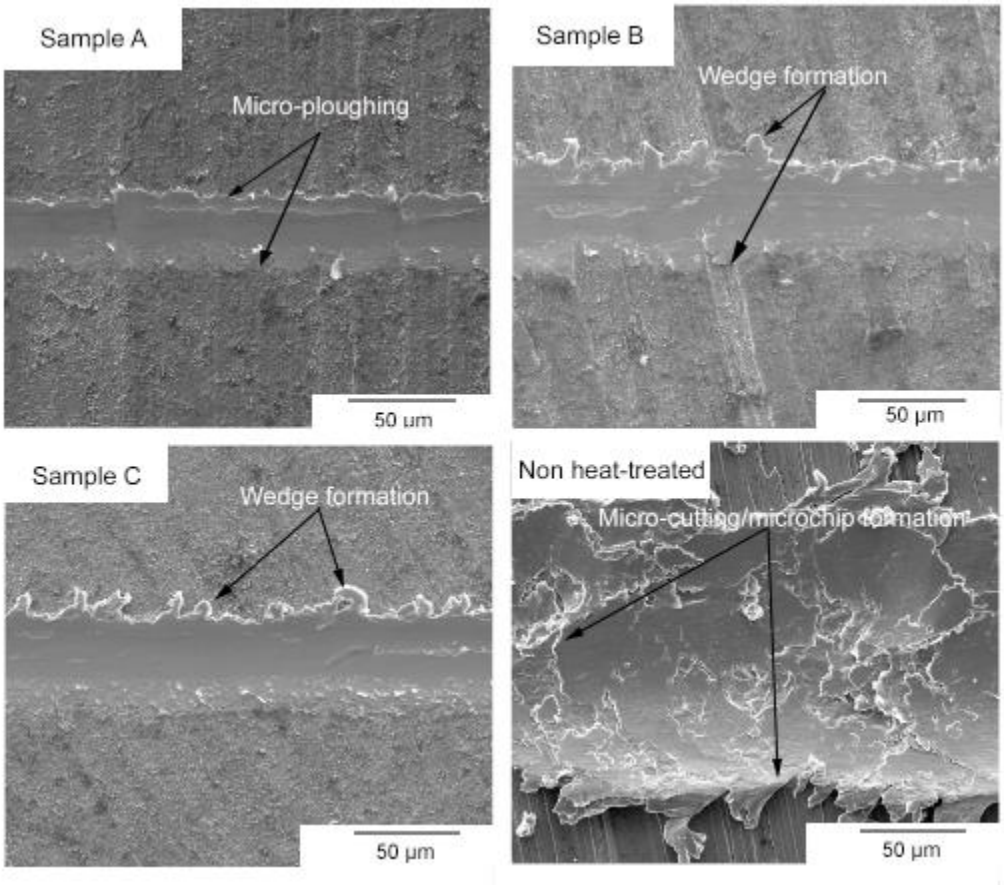

Figure 2.8: Field Emission Scanning Electron Microscope (FESEM) images of wear tracks from sliding tests against a diamond probe at 7.5 GPa contact stress condition. Prominent features indicating dominant wear mechanisms are highlighted.

Wedge formation is the intermediate transition mode between micro-ploughing and cutting in case of abrasive wear. For sample D, at both 6 GPa and 7.5 GPa contact pressure conditions, several microchips as well as severe fracture on the wear track are observed. This is indicative of microcutting as the abrasive wear mechanism for this non-carburized sample.

In order to verify the observed wear mechanisms, Hokirigawa and Kato's empirical relationship for abrasive wear [39, 40] was used to predict the abrasive wear mode. In this model, the degree of penetration, defined by ratio of depth of groove and the radius of contact, was calculated for each sample. A degree of penetration of 0.12 or lower is indicative of micro-ploughing; values of 0.12-0.18 are indicative of wedge formation and values above 0.18 point to microcutting as the dominant wear mechanism. At the contact pressure of 6 GPa, the depth of penetration is approximately 0.05 for all three samples, indicating that the abrasive wear mechanism should be micro-ploughing for all the samples. This helps explain the comparable wear depths observed for all the samples at this contact pressure. For sample B and C at a contact pressure of 7.5 GPa, the degree of penetration was above 0.14, which indicates that the abrasive wear mechanism is wedge formation, which is consistent with the observations. For sample A, the degree of penetration was close to 0.08, indicating that the dominant wear mechanism continues to be micro-ploughing only, which is again consistent with the observations. Since sample D is non-carburized its wear resistance is very low compared to other three samples. For sample D, the calculated degree of penetration exceeded 1 for both higher and lower pressure conditions, which is indicative of cutting. Thus, the inference from FESEM images for the samples are verified by Hokirigawa's empirical model.

Wear track zones were further analyzed using Energy Dispersive X-Ray spectroscopy to study elemental compositions inside and outside wear track as shown in Figure 2.9 (top images) for samples A and C. It was observed that inside wear track, the zones were mainly Fe and oxygen rich (zone A and B in both samples) and outside wear track the zones were mainly carbon, Mn and Cr rich (Zone C and D in both samples).

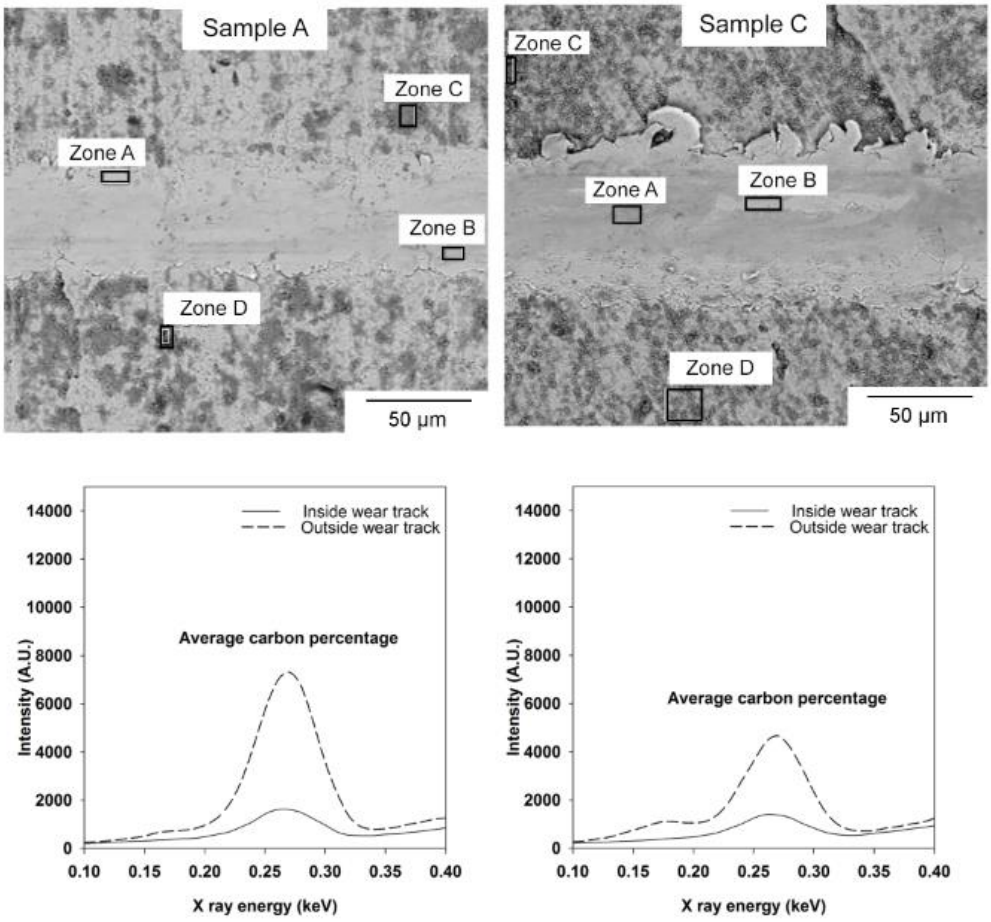

Figure 2.9: Energy Dispersive X-ray Spectroscopy point analysis study on wear track zones for selected samples subjected to sliding against a diamond probe at 7.5 GPa contact stress condition.

There was also some amount of Si and Mo since they are also key compositional element for AISI 8620 steel. Signals acquired from inside wear tracks (zones A and B) and outside wear tracks (zones C and D) for both samples were averaged out for X-ray energy levels of 0.1 to 0.4 keV range to show carbon peak inside and outside wear track. Outside the wear track, sample A has a significant carbon peak signal than sample C which is attributed to the higher carbon potential used for sample A. Previous studies [41-43] showed that at high temperature (900-1000°C) alloying elements of steel can influence

carbon activity on surface in the following way: Ni and Si help to increase whereas Cr, Mn and Mo decrease surface carbon concentration.

For present study, all carburized samples were prepared from same bar stock of AISI 8620 steel to avoid external effect from alloying elements on carbon activity. This higher carbon content contributes to the higher hardness for sample A. Both samples however show comparable amount of carbon inside the wear track. The wear track depths are ~ 400nm for sample A and ~650nm for sample C. For both samples, the darker zones outside wear track are the Mn and Cr enriched zones. During heat treatment Mn-Cr elements may have migrated towards the surface. A negligible content of Mn and Cr observed inside the wear track due to removal of top layer during wear test.

The wear studies suggest that above a certain contact pressure, the higher amount of hardness and RA helps to enhance abrasive wear resistance. Although austenite tends to have lower hardness than martensite, in this study the sample with highest RA also exhibited the highest hardness due to increased carbon potential during carburizing. It is known that austenite can undergo strain-induced transformation to the harder martensite during sliding [21]. Figure 2.7 showed the occurrence of ploughing and wedge formation on different carburized samples. This plastic deformation based mechanism occurring over 750 cycles can plausibly create conditions conducive to the martensitic transformation during our tests. The increase in wear resistance for sample A was most likely aided by strain-induced transformation of the austenite to martensite. Thus, it is likely that the higher RA% for sample A seems to further enhance the wear resistance as compared to sample B and C. The RA contribution also helps sample B exhibit a slightly better wear resistance compared to sample C.

2.6 Conclusions

A 3-15% range of RA with varied hardness and residual stress in AISI 8620 steel was achieved by varying carbon potential (0.45% to 1.05%) during carburizing as well as by employing different end-quenching routes (from air-cooling to deep freezing). Table 2.2 shows a summary of the resulting tribomechanical properties of samples subjected to different heat treatment routes (as described in Figure 2.1).

Table 2.2: Summary of experimental results

Heat treatment scheme[a]	Hardness (GPa)	RA %	Residual stress (MPa)	Wear[b] (μm)	Friction[c] coefficient
A	8.61±0.87	15.3±1.08	746±176	0.38±0.11	0.11±0.01
B	6.77±0.5	5±0.92	715±59	0.62±0.11	0.12±0.01
C	7.16±0.48	3.5±0.36	662±38	0.66±0.05	0.1±0.01
Non- heat-treated	2.52±0.07	3±0.3	452±98	7.74±0.75	0.11±0.01

[a] for refer to Figure 2.1
[b] for 7.5 GPa contact pressure condition against diamond probe
[c] for friction test against steel probe for a ramped test at maximum contact pressure of 600 MPa

Varying the carbon potential impacted the resulting range of RA% more than varying quenching routes. The higher carbon potential resulted in higher hardness due to increased carbon near the surface. The carburizing technique generates compressive residual stress which is beneficial for wear resistance. The hardness and amount of RA contribute more to the differences in wear behavior of samples as compared to the residual stresses. The results show that the combined effect of RA and hardness on the abrasive wear resistance is highly dependent on the contact stress. Below a certain pressure level, the effect of RA is insignificant. At higher contact pressures, a higher hardness and higher RA% result in superior wear resistance. This is attributed to the

higher hardness resulting from the heat treatment route to generate higher RA% as well as martensitic transformation of austenite during sliding. The role of RA increases at higher penetration depths where the effect of carbon potential (and hence hardness) plays a lesser role. The heat treatments did not significantly affect the coefficient of friction of the samples when subjected to dry sliding against a steel probe.

The findings indicate that heat treatment technique for 8620 steels modelled in such a way as to produce higher hardness as well as moderately higher RA (~15%), through carburizing and quenching will yield increased abrasive wear resistance. This study also provides some insight into varying the RA in AISI 8620 steel, which is commonly used in drivetrains, and the effect that the RA can have on abrasive wear resistance.

2.7 Acknowledgements

The authors would like to thank W. Martinek in the Mechanical Engineering Department for his help with sample preparation, W. Straszheim in the Materials Analysis and Research Laboratory (MARL) for help with SEM imaging and S.M. Schlorholtz for assisting with the XRD measurements. Partial funding for this work was provided by a grant from John Deere, Product Engineering Center, Waterloo, Iowa.

2.8 References

1. Kim, S.Y., S. Kubota, and M. Yamanaka, *Application of CAE in cold forging and heat treatment processes for manufacturing of precision helical gear part.* Journal of Materials Processing Technology, 2008. **201**(1-3): p. 25-31.

2. Ferguson, B.L., Z. Li, and A.M. Freborg, *Modeling heat treatment of steel parts.* Computational Materials Science, 2005. **34**(3): p. 274-281.

3. Atraszkiewicz, R., et al., *High pressure gas quenching: Distortion analysis in gears after heat treatment.* Materials Science and Engineering a-Structural Materials Properties Microstructure and Processing, 2012. **558**: p. 550-557.

4. Cho, J.R., et al., *Distortions induced by heat treatment of automotive bevel gears.* Journal of Materials Processing Technology, 2004. **153**: p. 476-481.

5. Matlock, D.K., et al., *Surface Processing to Improve the Fatigue Resistance of Advanced Bar Steels for Automotive Applications.* Materials Research, 2005. **8**: p. 453-459.

6. Harmer, S. *Heat Treatment of Steels-The Processes*. 2001; Available from: http://www.azom.com/article.aspx?ArticleID=543.

7. Siepak, J., *The Influence of Contact Stress on the Wear of a Carburized Steel Case with a High Content of Retained Austenite.* Wear, 1982. **80**(3): p. 301-305.

8. Asi, O., et al., *The relationship between case depth and bending fatigue strength of gas carburized SAE 8620 steel.* Surface & Coatings Technology, 2007. **201**(12): p. 5979-5987.

9. Scheuer, C.J., et al., *Low temperature plasma carburizing of martensitic stainless steel.* Materials Science and Engineering a-Structural Materials Properties Microstructure and Processing, 2012. **539**: p. 369-372.

10. Scheuer, C.J., et al., *Low-temperature plasma carburizing of AISI 420 martensitic stainless steel: Influence of gas mixture and gas flow rate.* Surface & Coatings Technology, 2012. **206**(24): p. 5085-5090.

11. Krauss, G., *Microstructure and Fracture of a Carburized Steel.* Metallurgical Transactions a-Physical Metallurgy and Materials Science, 1978. **9**(11): p. 1527-1535.

12. Parrish, G., *Carburizing: Microstructures and properties.* Heat Treatment of Metals, 2000. **27**(2): p. 38-38.

13. Colaco, R. and R. Vilar, *On the influence of retained austenite in the abrasive wear behaviour of a laser surface melted tool steel.* Wear, 2005. **258**(1-4): p. 225-231.

14. Coronado, J.J. and A. Sinatora, *Abrasive wear study of white cast iron with different solidification rates.* Wear, 2009. **267**(11): p. 2116-2121.

15. Li, C.G., et al., *Influence of Carbon Content of Martensitic Matrix and Retained Austenite on Wear of Martensitic Ductile Iron.* Wear, 1993. **162**: p. 75-82.

16. Kim, H.J. and Y.G. Kweon, *The effects of retained austenite on dry sliding wear behavior of carburized steels.* Wear, 1996. **193**(1): p. 8-15.

17. Xi, J.T., et al., *Influence of Retained Austenite on the Wear-Resistance of High Chromium Cast-Iron under Various Impact Loads.* Wear, 1993. **162**: p. 83-88.

18. Abareshi, M. and E. Emadoddin, *Effect of retained austenite characteristics on fatigue behavior and tensile properties of transformation induced plasticity steel.* Materials & Design, 2011. **32**(10): p. 5099-5105.

19. Jeddi, D. and H.P. Lieurade, *Effect of retained austenite on high cycle fatigue behavior of carburized 14NiCr11 steel.* Fatigue 2010, 2010. **2**(1): p. 1927-1936.

20. Hu, Z.Z., et al., *The effect of austenite on low cycle fatigue in three-phase steel.* International Journal of Fatigue, 1997. **19**(8-9): p. 641-646.

21. Gahr, K.-H.Z., *Microstructure and Wear of Materials*. Tribology Series. Vol. 10. 1987: Elsevier.

22. *AISI 8620 Steel, normalized, machined to 13.7 mm, pseudocarburized, oil quenched, 150°C temper*. Available from: http://www.matweb.com/search/datasheet.aspx?matguid=fd4eba76fdeb4a0a9fcbbc0129250761.

23. Verhoeven, J.D., *Steel Metallurgy for the Non-Metallurgist*. 2007: ASM International.

24. Yaso, M., et al., *Characteristics of Retained Austenite in Quenched High C-High Cr Alloy Steels.* Materials Transactions, 2009. **50**(2): p. 275-279.

25. Zhao, L., et al., *Magnetic and X-ray diffraction measurements for the determination of retained austenite in TRIP steels.* Materials Science and Engineering a-Structural Materials Properties Microstructure and Processing, 2001. **313**(1-2): p. 145-152.

26. *Standard Practice for X-Ray Determination of Retained Austenite in Steel with Near Random Crystallographic Orientation*, in *ASTM E975-13*.

27. Bruker, *TOPAS V4.2 User's Manual*. 2009.

28. Sturm, R., M. Stefanikova, and D.S. Petrovic, *Influence of pre-heating on the surface modification of powder-metallurgy processed cold-work tool steel during laser surface melting.* Applied Surface Science, 2015. **325**: p. 203-210.

29. Prevéy, P., *Current Applications of X-ray Diffraction Residual Stress Measurement*. 1996, Lambda Technologies.

30. *Standard Test Method for Residual Stress Measurement by X-Ray Diffraction for Bearing Steels*, in *ASTM E2860-12*.

31. Fitzpatrick, M., et al., *Determination of Residual Stresses by X-ray Diffraction – Issue 2*. 2005, National Physics Laboratory.

32. Bensely, A., et al., *Effect of cryogenic treatment on tensile behavior of case carburized steel-815M17.* Materials Characterization, 2007. **58**(5): p. 485-491.

33. Bensely, A., et al., *Effect of cryogenic treatment on distribution of residual stress in case carburized En 353 steel.* Materials Science and Engineering a-Structural Materials Properties Microstructure and Processing, 2008. **479**(1-2): p. 229-235.

34. Kulka, M., A. Pertek, and N. Makuch, *The importance of carbon concentration-depth profile beneath iron borides for low-cycle fatigue strength.* Materials Science and Engineering a-Structural Materials Properties Microstructure and Processing, 2011. **528**(29-30): p. 8641-8650.

35. Rowan, O.K. and R.D. Sisson, *Effect of Alloy Composition on Carburizing Performance of Steel.* Journal of Phase Equilibria and Diffusion, 2009. **30**(3): p. 235-241.

36. Liu, H.H., et al., *Effects of cryogenic treatment on microstructure and abrasion resistance of CrMnB high-chromium cast iron subjected to sub-critical treatment.* Materials Science and Engineering a-Structural Materials Properties Microstructure and Processing, 2008. **478**(1-2): p. 324-328.

37. Ulutan, M., et al., *Effect of Different Surface Treatment Methods on the Friction and Wear Behavior of AISI 4140 Steel.* Journal of Materials Science & Technology, 2010. **26**(3): p. 251-257.

38. Totik, Y., et al., *The effects of induction hardening on wear properties of AISI 4140 steel in dry sliding conditions.* Materials & Design, 2003. **24**(1): p. 25-30.

39. Hokkirigawa, K. and K. Kato, *An Experimental and Theoretical Investigation of Plowing, Cutting and Wedge Formation during Abrasive Wear.* Tribology International, 1988. **21**(1): p. 51-57.

40. Hokkirigawa, K., K. Kato, and Z.Z. Li, *The Effect of Hardness on the Transition of the Abrasive Wear Mechanism of Steels.* Wear, 1988. **123**(2): p. 241-251.

41. Przylecka, M., M. Kulka, and W. Gestwa, *The Activity of Carbon in the 2-Phase Fields of the Fe-Cr-C, Fe-Mn-C and Fe-Si-C Alloys at 1173-K.* Proceedings of the Second Asm Heat Treatment and Surface Engineering Conference in Europe, Pts 1 and 2, 1994. **163-**: p. 87-92.

42. Wada, T., et al., *Thermodynamics of Fcc Fe-Mn-C and Fe-Si-C Alloys.* Metallurgical Transactions, 1972. **3**(6): p. 1657-1662.

43. Wada, T., et al., *Activity of Carbon and Solubility of Carbides in Fcc Fe-Mo-C, Fe-Cr-C, and Fe-V-C Alloys.* Metallurgical Transactions, 1972. **3**(11): p. 2865-2872.

CHAPTER 3. EFFECT OF LASER TREATMENT PARAMETERS ON SURFACE MODIFICATION AND TRIBOLOGICAL BEHAVIOR OF AISI 8620 STEEL

Modified from a paper published in *Tribology International*

Sougata Roy, Jingnan Zhao, Pranav Shrotriya, Sriram Sundararajan

3.1 Abstract

In this study, the effect of different shielding gas and laser scanning velocity on the resulting retained austenite (RA) content and tribomechanical properties of AISI 8620 steel were investigated. RA generation was comparatively lower at higher scanning velocity and with argon as the shielding gas due to lower beam interaction time and inert environment. Varied heat input and differing reaction volume resulted in different hardness levels on these samples. Air shielded samples showed slightly higher friction coefficient than the other samples due to higher surface roughness and shearing of oxide layers. The nitrogen shielded samples exhibited the best wear resistance among all samples, which was attributed to nitride formation on surface and to high hardness resulting from the laser treatment.

3.2 Introduction

Laser surface treatment is a widely used technique to enhance microstructural properties, surface hardness and wear resistance of different engineering materials. By varying the pertinent laser parameters, different regimes of laser-material interaction (e.g. heating, melting and evaporation) [1] can be achieved. Laser heat treatment relies on transformation based hardening where a laser beam travels across workpiece resulting in rapid heating of the top surface layers [2]. The bulk material works as a heat sink during the quenching

phase transformation. Thus, a harder surface layer is realized while keeping the bulk material properties (e.g. ductility, toughness etc.) unaffected. The positive aspects of laser surface heat treatment are minimal part distortion, high repeatability, controlled depth of hardened layers without use of any external quenchant and minimal to no requirement for final machining of part. In laser heat treatment processes, it is crucial to observe the effect of several process parameters [3, 4] such as, laser power, beam diameters, overlapping percentage and scanning velocity to achieve the desired laser material interaction.

An important microstructural property for steels that is affected during the phase transformation process is the amount of retained austenite (RA). RA is important because it has significant effect on wear resistance [5-7], dimensional stability [8, 9] and fatigue behavior [10-12] of machine elements made from steel. Colaco and Villar observed that an increase in RA from 15% to 100% during laser surface melting process can show deleterious effect on wear resistance [13]. On the other hand, Dogan et al. [14] studied effect of RA on abrasion resistance of high-Cr white cast irons using a pin abrasion test where he observed better abrasive wear resistance when the matrix was composed of mixture of austenite & martensite. Thus, it is better to modulate steel microstructure in such a way as to contain moderate to less amount of RA, thereby leading to better wear resistance and dimensional stability. Although Colaco and Villar [13, 15, 16] have contributed significantly in this area, their studies addressed tool steel with high chromium percentage and focused mainly on the laser melting regime. There is also a need to understand the effect of laser heat treatment on RA formation and tribological behavior of steel during laser heating regime.

Scanning velocity and choice of shielding gas during laser processing can affect the resulting properties and quality of the treated sample. Scanning velocity is known to affect RA stabilization [17] during laser melting process, hardened depth [3] as well as residual stress and crack population [4] in steels during laser surface treatment. The choice of shielding gas has been studied in the context of laser welding [18, 19] and has been shown to affect the formability, weld microstructure and mechanical properties in steels [18] and titanium [19].

The objective of this study was to investigate the effect of different shielding gas (nitrogen, argon and air) and laser scanning velocity (70-110 inch/min) on the resulting retained austenite content (RA%) and the tribomechanical properties of AISI 8620 steel. The rationale was to utilize parameters resulting in moderate to low RA% in the samples in order to avoid the issues related to poor wear resistance and dimensional stability encountered in the case of excessively high RA levels.

3.3 Materials

AISI 8620 steel was chosen for this study since this steel is widely used in various drivetrain components which are generally heat treated to achieve desired mechanical properties. Chemical analysis of used raw material was conducted using Optical Emission Spectroscopy (according to ASTM E415 standard). The chemical composition of AISI 8620 steel is given in table 1.

For this study, circular discs (20 mm diameter, 10 mm thick) were cut from a long bar of AISI 8620 steel (supplier: McMaster Carr). Both surfaces were CNC-milled followed by surface ground to minimize initial surface roughness before laser treatment. A Zygo NewView 7100 non-contact profilometer was used to measure surface roughness of the

samples. All samples exhibited an average surface roughness (Ra) in the range of 0.4-0.5 μm over a scan size of 1.88 mm×1.41 mm.

Table 3.1: Composition of AISI 8620 steel

Component	**Wt%**
C	0.22
Cr	0.52
Fe	97.37
Mn	0.85
Mo	0.15
Ni	0.41
P	0.008
S	0.026
Si	0.25
Cu	0.17
Al	0.024

Laser surface heat treatment was carried out with a CNC controlled continuous wave CO_2 laser. The sample surfaces were cleaned with acetone before being mounted on X-Y positioning stage. Figure 3.1 shows a schematic representation of laser heat treatment process used for this study. The heat treatment was performed using a defocused beam of 1 mm diameter with an overlap of 50% to cover a circular surface area of 20 mm diameter surface. The overlapping percentage was calculated using the equation as follows [20, 21]:

$$\text{Overlapping percentage} = \frac{d-f}{d}\times 100\% = \frac{1-0.5}{1}\times 100\% = 50\%$$

Where: d is the laser beam diameter (mm) and f is the distance between the axes of adjacent tracks (mm).

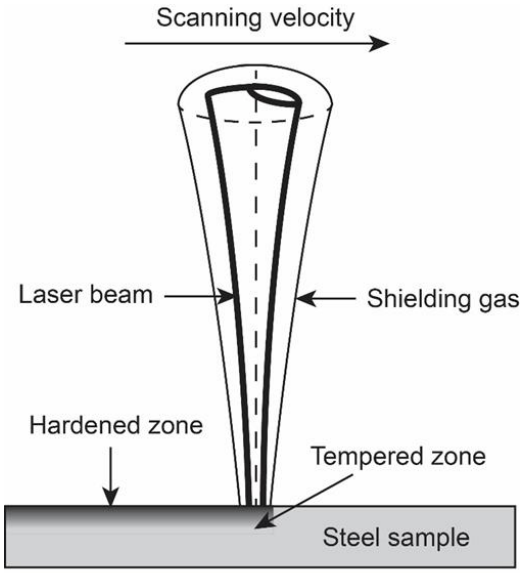

Figure 3.1: Schematic for laser heat treatment of steel described in the study

Laser power, beam diameter and scanning velocity are the most important parameters which dictate the regime of laser material interaction i.e. whether the process will result in heating, melting or vaporization. Previous studies [1, 2, 22] have helped to establish guidelines based on interaction time and power density to ensure the occurrence of transformation hardening during laser heat treatment. Based on those, for the present study a power of 920 watts, a scanning velocity of 70-110 inch/min and three different shielding gases - air, nitrogen and argon were used so that laser material interaction remains in the heat treatment regime. Following heat treatment, the samples were cleaned again with acetone and then subjected to metallographic and tribological analysis. Each laser treatment condition was repeated three times to help ensure statistical significance of the results.

3.4 Methods

3.4.1 Measurement of Retained Austenite (RA)

X-ray diffraction (XRD) is one of techniques used to accurately quantify the amount of RA [23-25]. In this study, a Bragg-Brentano type Siemens D 500 X-ray diffractometer with a graphite monochromator and point detector was used to quantify RA percentage of the samples after heat treatment. A Cu Kα target was used (wavelength 0.15418 nm) with a target voltage of 40 kV and current 30 mA. XRD scan data for a range of 40 to 90 degrees (2θ angle) was analyzed using TOPAS software to determine the amount of RA in those samples. An estimation of the penetration depth of the Cu-X-ray as per Beer-Lambert's law [26] yielded a value of 4.2μm. Thus, the RA measurement zone was well within the phase transformed zone during laser heat treatment. Laser treated samples were ultrasonically cleaned before conducting XRD study. TOPAS uses the Rietveld method which helps to fit theoretical data to a measured pattern using analytical profile functions & least square methods [27]. During quantitative study, structure information files of iron alpha (ICDD # 60696), iron gamma (ICDD # 310619), magnetite (ICDD # 190629) and wustite (ICDD # 60615) files were used for measurement of RA% on the samples. For each experimental condition, three repetitions were conducted and mean value of calculated RA% along with error bars showing 90% confidence interval was plotted. Some studies calculate and report the RA% while ignoring the amount of magnetite or other phases present in the sample [6] while others include other phases also in the calculations [28]. In this case RA% was calculated including the presence of third and fourth phases (magnetite and wustite in air shielded case) in the samples.

3.4.2 Micro-hardness tests

Surface hardness is influenced by heat treatments and often can correlate to wear resistance. Hardness for each sample was evaluated using a Leco LM247AT microhardness tester with a Vickers diamond indenter and associated Amh43 software. Ten measurements at a load of 200 gf were made on each sample and mean of those measurements were calculated and reported along with a 90% confidence interval. The dwell time for each measurement was 13 seconds.

3.4.3 Microstructural study on laser treated samples

After laser heat treatment the samples were cut perpendicular to the treated surface to prepare metallographic specimens. The samples were polished starting with 400, 600, 800, 1200 SiC grits papers and subsequently with 5, 3, 1 μm diamond suspension. In order to reveal the microstructure, the samples were etched with 2.5% nital solution. The microstructures of polished and etched cross-sections of the specimens were observed by a field emission scanning electron microscope to evaluate reaction volume of laser treatment.

3.4.4 Finite element modelling of laser heat treatment process

In order to understand the effect of scanning velocity on the resulting microstructure and tribomechanical properties finite element based modelling was conducted. The use of numerical and computational approaches has been shown to predict surface temperatures during laser material interaction [29-31]. Based on operating parameters and sample geometry used, an axisymmetric model was developed to observe the effect of different scanning velocities on the maximum surface temperature generated on the surface of sample. The finite element analysis (FEA) package ABAQUS/Standard was used to

incorporate static heat flux and material properties to simulate the laser-material interaction in laser heating regime. The sample cross-section (10 mm×10 mm) was modelled and partitioned appropriately to get better approximation to surface temperature generation as shown in Figure 3.6. As can be seen, element sizes were biased from the top left corner (input heat flux zone) to the bottom right to study heat dissipation in sample. Beam interaction times were calculated based on scanning velocity levels and beam diameter used for this study. A Gaussian intensity profile was used to calculate input heat flux during laser treatment. Saleh and Teich model [29, 32] was used to estimate the emitted intensity of a Gaussian beam, according to;

$$I(x) = \frac{2P}{\pi r^2} e^{\frac{-2x^2}{r^2}} \tag{3.1}$$

where, P is total power emitted and r is beam radius. An effective absorptivity factor of 0.1 was used for ground steel surface [33]. To simulate the laser heating during experiments, the FEA model introduced a heat flux for a period of time equivalent to the beam interaction time (e.g. at a specific scanning velocity). This was followed by a dwell time of 0.02 sec to observe the effect of the heat input on temperature generation on the sample surface.

3.4.5 Microscale friction and wear tests

Friction and wear tests were conducted using a universal benchtop tribometer (RTEC Multi-Functional Tribometer, USA) using ball-on-flat arrangement that can produce a microscale multi-asperity contact. Test setup and schematic diagram of its major components are shown in Figure 3.2. A desired probe of specific radius was placed at the end of a specific diameter probe holder, which was lowered using a linear stage to apply a desired normal load to the sample attached to a reciprocating horizontal stage. Six degrees

of freedom (DoF) load cells were used to simultaneously measure force and torque along three orthogonal axes: X, Y and Z. Normal load range for the tribometer was nN to 5000N. The resolution for forces (F_x, F_y and F_z) in three directions was around 0.001N and the sampling rate for data collection was 1000 Hz. All friction and wear experiments were conducted in a direction perpendicular to that produced by laser tracks for maintaining consistency between tests.

Friction tests were conducted to be mainly in the adhesive regime to understand the effect of laser treatment on the sample surface. Coefficient of friction between the samples and a spherical AISI 52100 steel probe (radius of 2 mm and an approximate hardness of 60 HRC) with an average Ra surface roughness 0.005 μm (over a scan size of 0.47 mm × 0.35 mm) was determined from a sliding test. Here the applied normal load was constant at 10N (maximum Hertzian contact pressure of 1.8 GPa) for a specific sliding distance of 5 mm at a speed of 1 mm/s while the lateral force and resulting friction coefficient were recorded. An average value of instantaneously recorded friction coefficient numbers during sliding test provided coefficient of friction.

Next, reciprocating sliding tests were conducted against a SiC probe (spherical tip with a radius of 2 mm for 15 cycles with a stroke speed of 1 mm/s at constant load of 88N (maximum Hertzian contact pressure of 4.5 GPa). One of the main failure modes in drive train components made of AISI 8620 steel is abrasive wear. Thus, it was our intent to conduct wear tests in an abrasive wear regime.

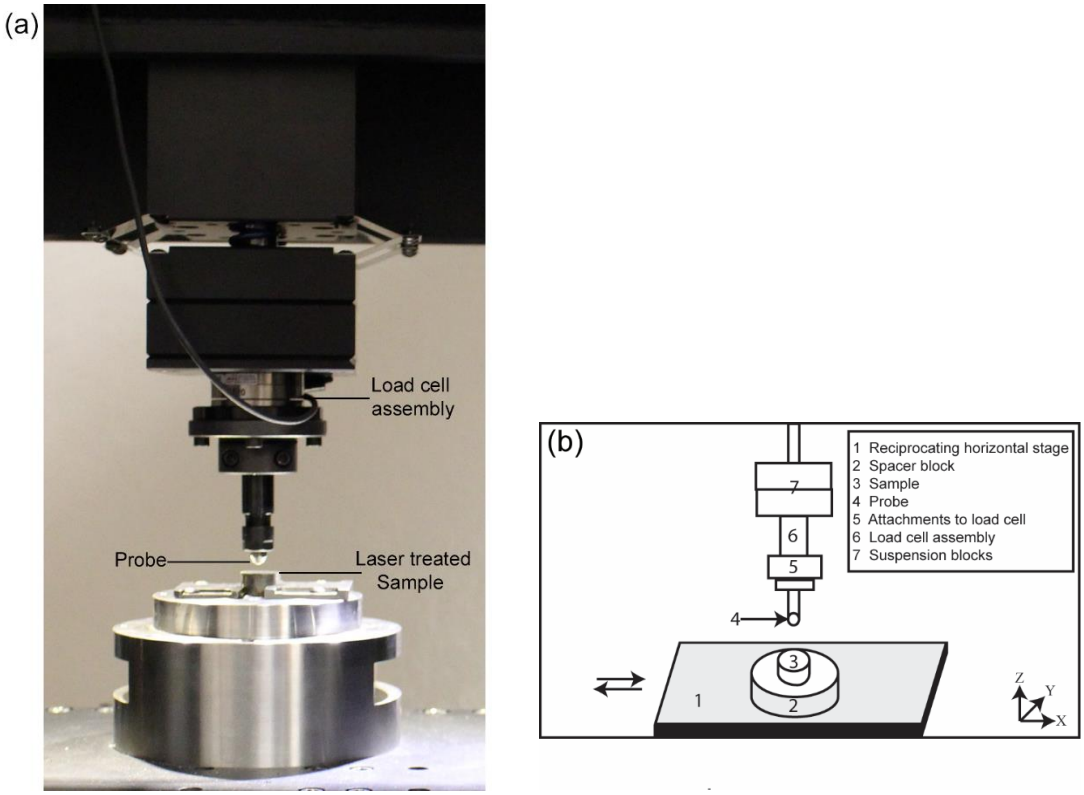

Figure 3.2: (a) RTEC tribometer for ball on disc friction and wear tests and (b) schematic diagram of tribometer

Accordingly, the probe was chosen to be a harder material (SiC) and the applied load (input pressure) and sliding distance were higher than that of the friction tests. All friction and wear tests were conducted under dry sliding conditions. Three repetitions were conducted for each test condition and mean values and 90% confidence intervals are reported for each case.

Wear track depths were measured using a non-contact surface profilometer (Zygo NewView 7100). Wear depth was measured at three regions along each wear track. To get an accurate and representative wear depth, at each region, three rectangular zones (areas) were created where the wear track zone was assigned as the test region and the

zones adjacent to the wear track on either side were assigned as the reference region. The test zone's average height was subtracted from reference zone's average height to get an averaged wear depth between wear track zone and its neighborhood zone.

An FEI Quanta-250 Scanning Electron Microscope (FESEM) was used to obtain high resolution images of wear tracks and an Oxford Aztec energy-dispersive x-ray analysis was used to perform elemental mapping of the SiC probe to confirm prevailing wear mechanisms.

3.5 Results & discussion

3.5.1 Effect of laser treatment on RA%

Figure 3.3 shows a comparison of the RA% levels for the different samples treated with different scanning velocity and shielding gas conditions. Colaco and Villar [17] showed that increasing scanning velocity from 1 to 20 mm/sec helped increase RA in laser melting of tool steel. But further increase beyond 20 mm/sec didn't result in further increase in RA. For the present study, effect of scanning velocity was studied in the laser heat treatment zone (without melting). It was observed that increasing scanning velocity from 70 to 110 inch/min resulted in slightly lower RA levels on surface. Increasing scanning velocity decreases beam interaction time with material which in turn decreases heat input to surface [34]. The decreased heat input contributes to lower RA due to lower surface temperature generation as will be discussed in detail later.

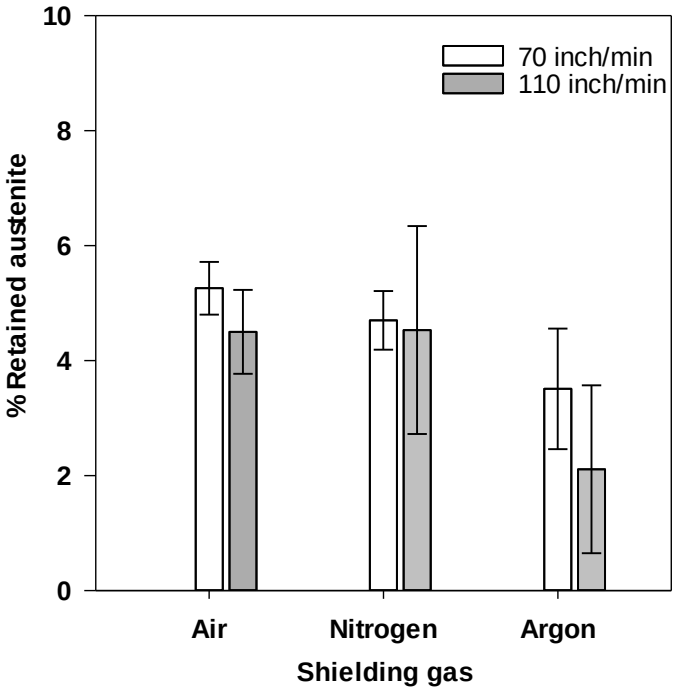

Figure 3.3: Retained austenite percentages of the samples. Mean values from three samples at each test condition are shown. Error bars represent 90% confidence intervals

Figure 3.4 shows the effect of shielding gas on the resulting RA%. It can be seen that for the nitrogen and air shielded cases, RA% on surface was higher than argon shielded case irrespective of scanning velocity. This is attributed to the fact that during the argon shielding, the laser material interaction zone becomes more inert than for the samples shielded by nitrogen and air. This results in a lower maximum temperature on surface for the argon shielded samples which in turn leads to a lower RA% on surface compared to the nitrogen and air shielded samples.

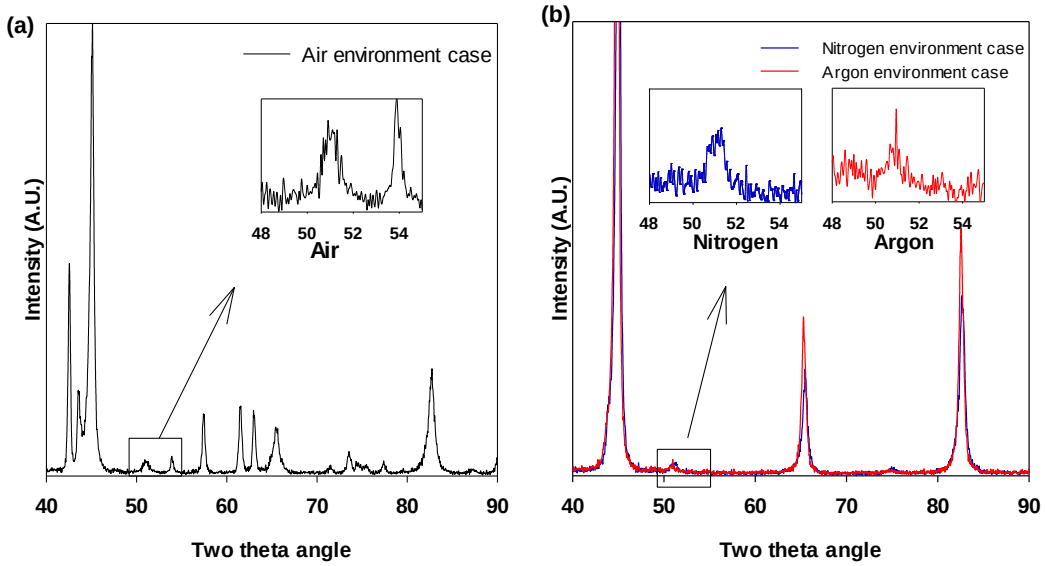

Figure 3.4: XRD analysis of laser treated steel in (a) air shielded condition and (b) in nitrogen and argon shielded condition

Figure 3.4 shows XRD data for laser treated samples with different shielding gases at a scanning velocity of 70 inch/min. For the air shielded case, peaks due to magnetite (Fe_3O_4) and wustite (FeO) phases were observed. These extra oxides (FeO or Fe_2O_3, Fe_3O_4) peaks were also observed by Pereira et al. [35] in their laser treatment of steel in ambient air. But for the argon and nitrogen shielded cases, there were no oxide peaks due to the inert environment during the treatment which confirms no oxygen contamination on treated surface. If the oxides are not taken into account, the RA% shows higher value for air shielded condition but for the present study, all phases on surface were included for calculating the RA%. Consequently, air and nitrogen shielded samples yielded higher RA% compared to argon shielded samples in both scanning velocity conditions.

3.5.2 Effect of laser heat treatment on microhardness

Figure 3.5 shows microhardness values exhibited by the various laser treated samples.

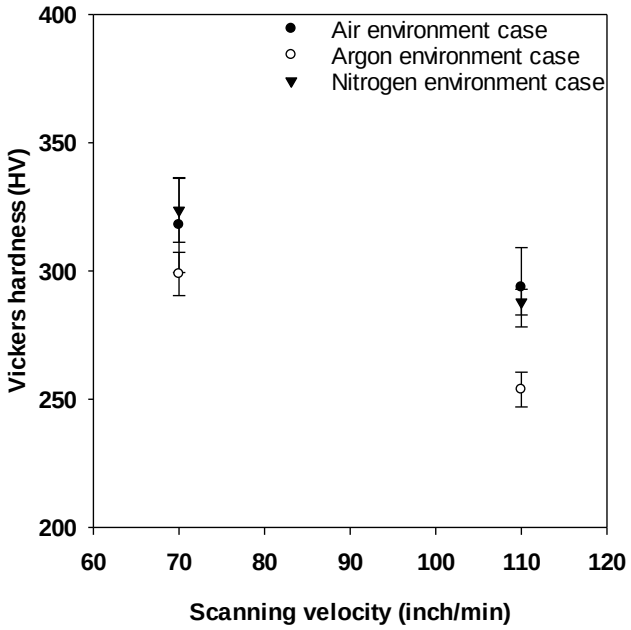

Figure 3.5: Microhardness test results for the laser-treated samples. Mean values from ten measurements are shown. For each condition three samples were heat treated using laser. Error bars represent 90% confidence intervals

The average hardness for the non-treated samples was around 220 HV. It was observed for the lower scanning velocity (70 inch/min) that the average surface hardness for air and nitrogen shielded case was around 320 HV. The surface hardness decreased with increasing scanning velocity. Also, surface hardness levels were lower for the argon shielded case compared to the nitrogen and air shielded cases.

Figure 3.6 shows cross sectional microstructures of samples treated with different shielding gases (scanning velocity 70 inch/min).

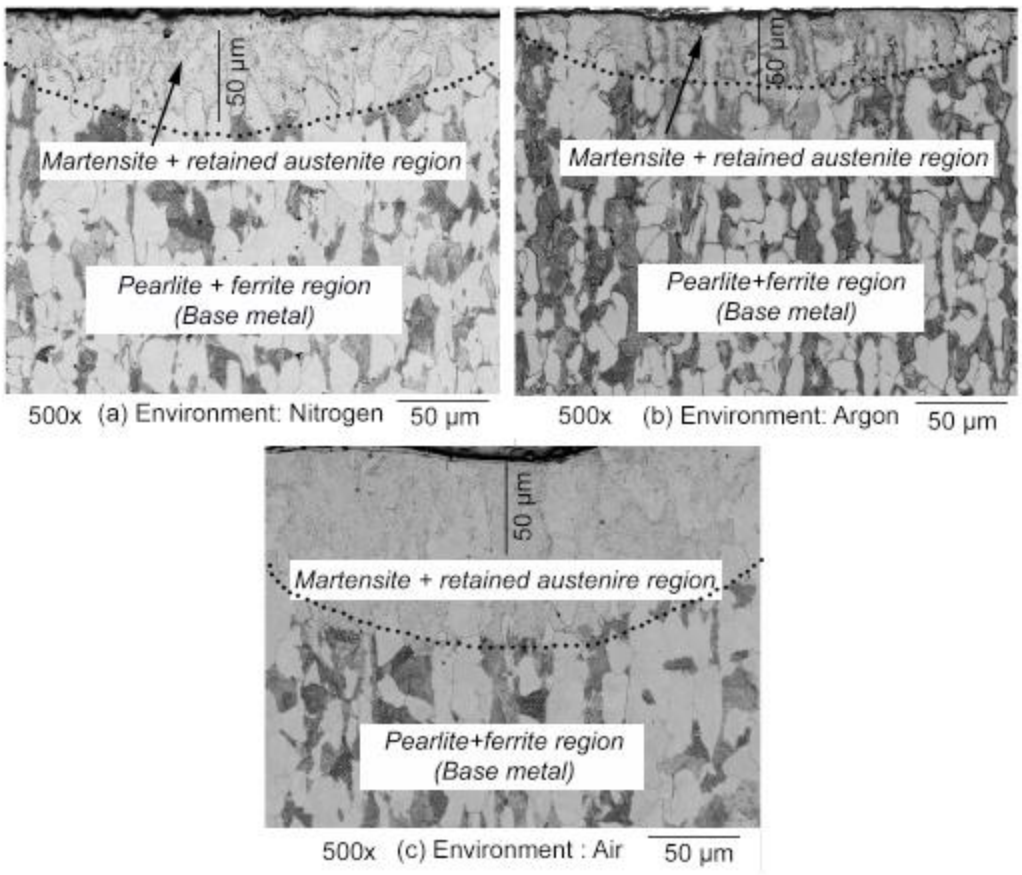

Figure 3.6: SEM micrograph of the cross section of the laser treated steel in (a) nitrogen (b) argon and (c) air shielded conditions

It can be observed in each case, phase transformation and grain refinement have taken place up to a certain depth from the surface. The laser treated zones closer to the surface are mainly composed of martensite and retained austenite whereas the base metal is composed of pearlite and ferrite. It can be observed the depth of the changed microstructure zone is lowest for argon shielded case which results in comparatively lower surface hardness in those samples.

Figure 3.7 shows the temperature distribution in the sample for a scanning velocity of 70 inch/min.

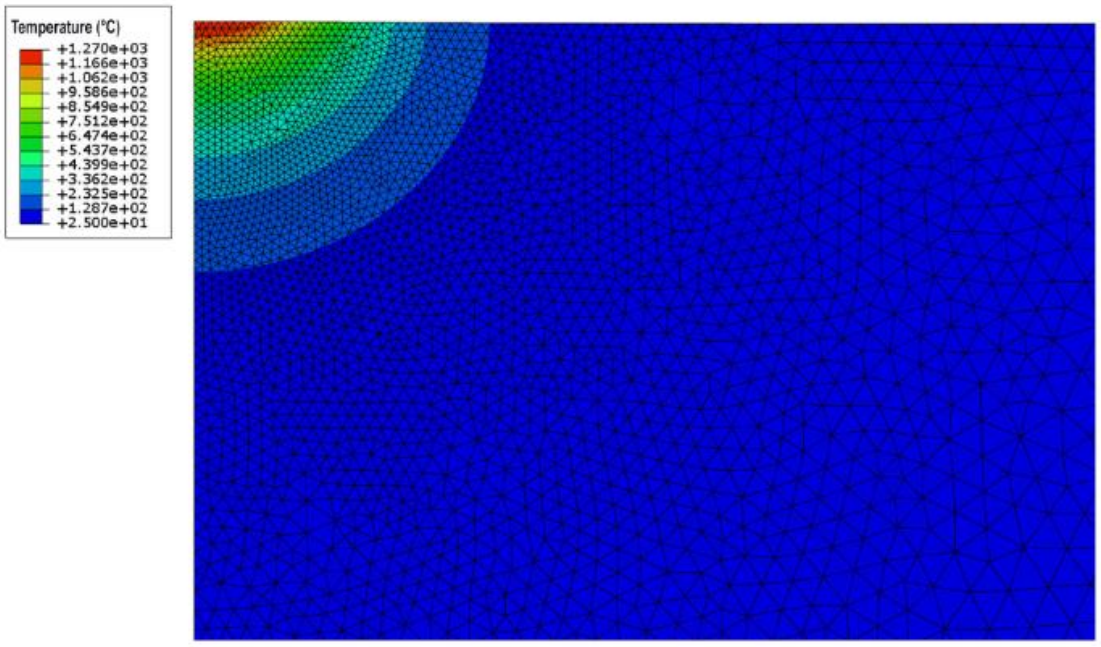

Figure 3.7: Temperature (°C) distribution (zoomed view) in sample due to laser heating at a scanning velocity of 70 inch/min

The maximum temperature level shows there should be phase transformation on the surface which was observed in the microstructure study (Figure 3.6). It can be observed that a very small area close to laser beam was exposed to high temperature levels but most of the sample worked as a heat sink. Thus, rapid heating and cooling occurred during laser treatment process. Figure 3.8 shows a quick drop in temperature from the surface to depth.

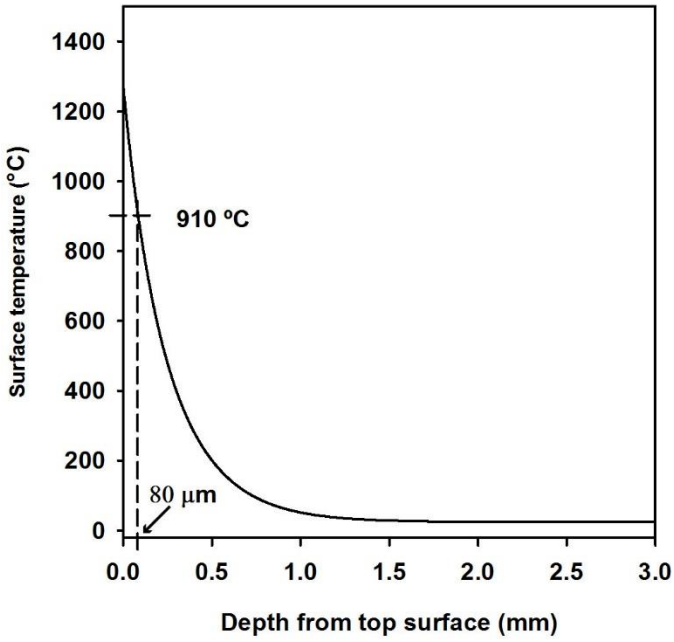

Figure 3.8: Temperature distribution along the sample depth due to laser heating at a scanning velocity of 70 inch/min

From 912 to 1394 °C alpha iron undergoes a phase transformation to austenite. Later, during rapid quenching, austenite converts to martensite and RA. Based on Figure 3.8, the depth at which surface temperature drops to around 910 °C was around 80 µm which is of same order of magnitude as observed from microstructure observation shown in Figure 3.6. The different shielding gases helped alter the depth at a scanning velocity of 70 inch/min. Figure 3.9 shows a significant difference in the maximum surface temperature generated between a scanning velocity of 70 inch/min and 110 inch/min.

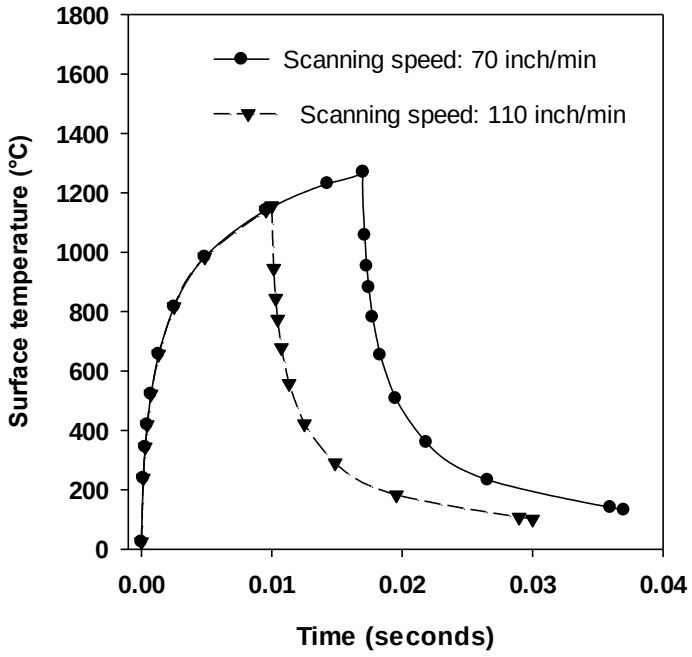

Figure 3.9: Temperature profiles of laser treated steel at different scanning velocities

Thus, there is significant reduction in heat input at higher scanning velocity which results in decreasing surface hardness. This is consistent with our experimental findings and that of Santhanakrishnan and Kovacevic [34] on laser heat treated tool steel.

3.5.3 Effect of laser treatment on surface roughness

A contact type Mahr profilometer was used to measure the surface roughness after laser treatment with a cut off length 0.8 mm and traverse length 5.6 mm. Figure 3.10 shows the resulting surface roughness of the laser treated samples.

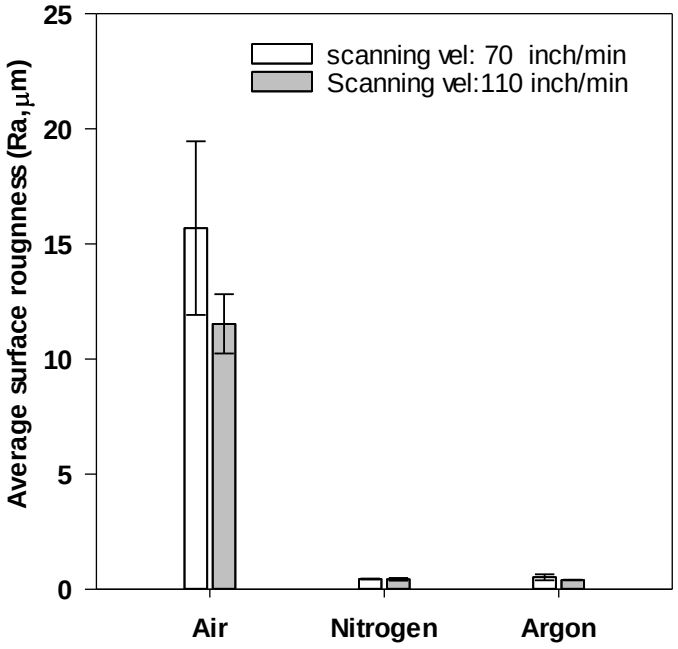

Figure 3.10: Surface roughness (Ra) values of laser treated samples. Mean values from three samples on each test conditions are shown. Error bars represent 90% confidence intervals

It was observed that for air shielded case, the surface roughness was significantly higher than the values for the nitrogen and argon shielded cases. However, oxygen content helps to increase the reaction volume as observed in the microstructure study. It therefore appears that oxygen content in air results in higher values of surface roughness since it is highly reactive to sample surface. Scanning velocity does not have an effect on nitrogen and argon shielded cases but for air shielded cases higher scanning velocity helps to reduce resulting surface roughness. Iwao et al. [36] showed that thicker oxide layer can result higher surface roughness. XRD results showed that the amount of magnetite and wustite (iron oxides) formation at surface for higher scanning velocity condition was comparatively lower due to less interaction time. This in turn might help to reduce surface roughness at higher scanning velocity case for the air shielded case.

3.5.4 Effect of laser treatment on friction & wear

In order to minimize the effect of surface roughness, air treated samples were ground to decrease the surface roughness values around 10 μm or below (as compared to ~15 μm) before conducting friction and wear tests. Figure 3.11 shows the coefficient of friction data exhibited laser treated samples against a steel probe under dry sliding condition.

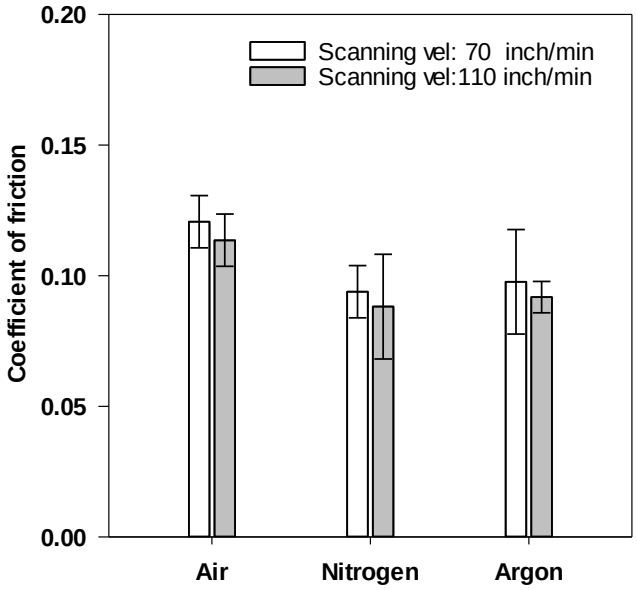

Figure 3.11: Friction coefficient values of laser treated samples. Mean values from three repetitions on each test conditions are shown. Error bars represent 90% confidence intervals

It can be observed that air shielded samples exhibited higher friction coefficient than nitrogen and argon shielded samples which have comparable friction coefficients. This trend is seen at both scanning velocities. The higher friction levels for the air-shielded samples are attributed to the shearing of oxidized layers [37] as well as topographical contributions from the higher surface roughness as compared to the other samples.

Figure 3.12 shows the wear track depth results from the reciprocating wear tests against SiC probe.

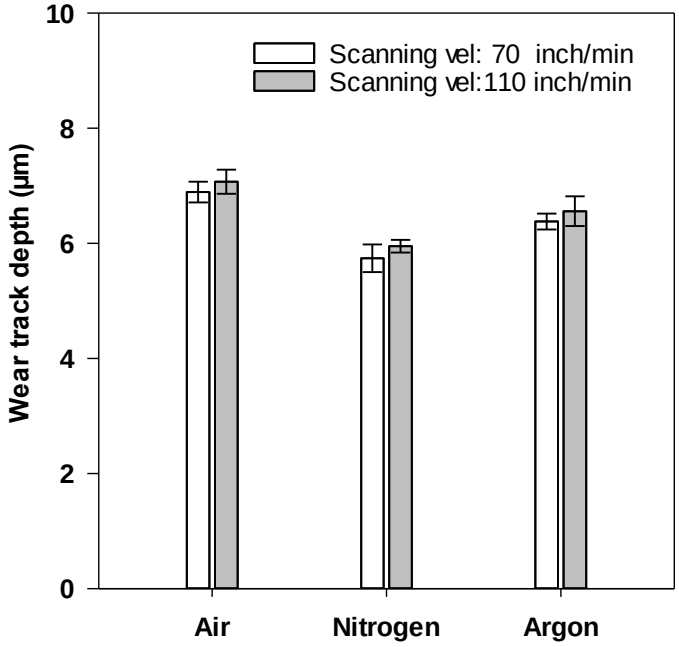

Figure 3.12: Wear track depth comparison between laser treated samples. Mean values from three repetitions of wear tests are shown. Error bars represent 90% confidence intervals

The nitrogen shielded samples exhibited the highest wear resistance followed by the argon shielded samples and the air shielded samples, which showed the poorest wear resistance. RA% variation within the samples were comparatively less (2-6%). Thus, RA is not the main factor in effecting the wear resistance among different samples. EDS elemental mapping study was conducted on the SiC probes revealed no material transfer onto the

probe, indicating that the prevalent wear mechanism during the tests was abrasive rather than adhesive. In order to understand the type of abrasive wear mechanisms, the wear tracks were analyzed using field emission scanning electron microscopy. Figure 3.13 shows representative images of wear tracks of samples laser treated with different shielding gases (scanning velocity 70 inch/min).

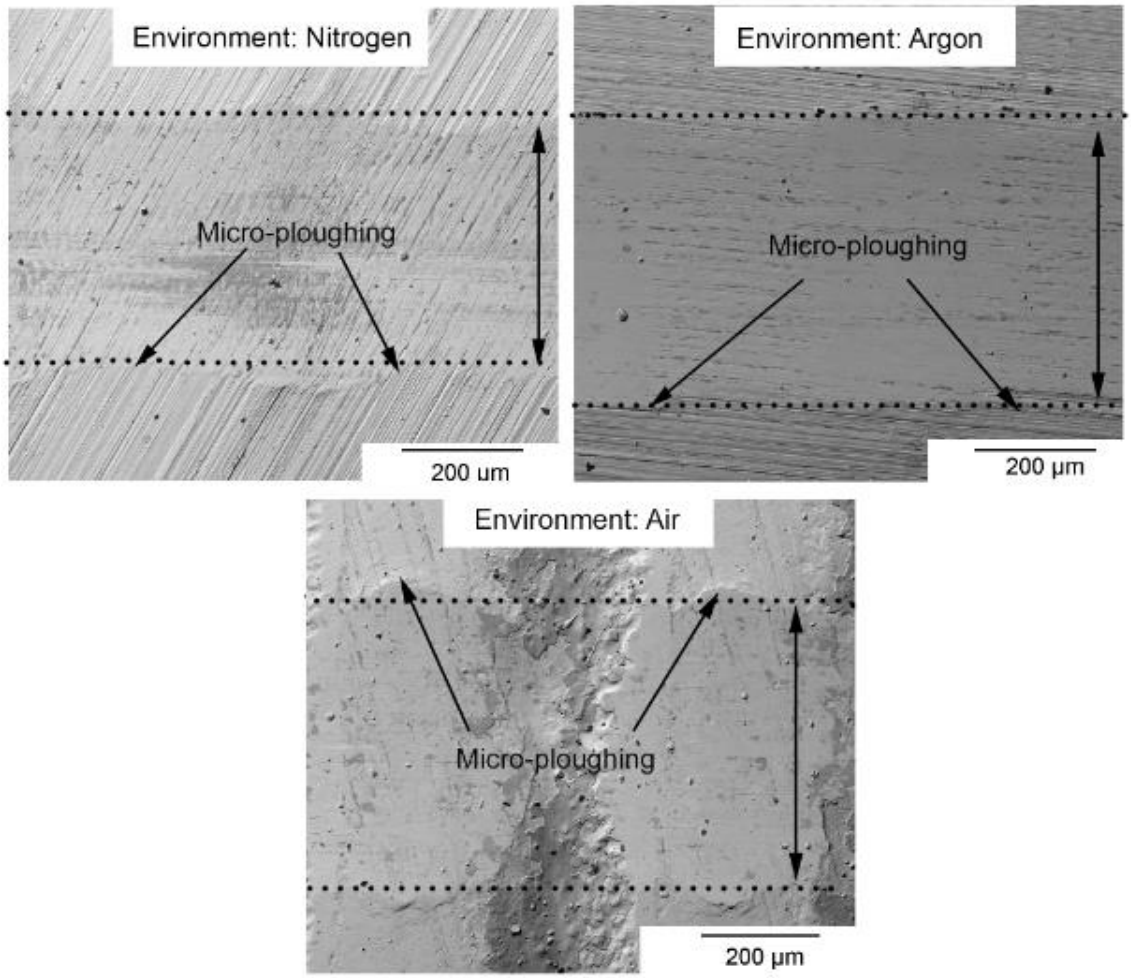

Figure 3.13: Field Emission Scanning Electron Microscope (FESEM) images of wear tracks from sliding tests against a SiC probe at 4.5 GPa contact stress condition. Prominent features indicating dominant wear mechanisms are highlighted

Three dominant wear mechanisms in abrasive wear are micro-cutting, wedge formation and micro-ploughing. In case of micro-ploughing mode, shallow grooves are formed due to repeated sliding and accumulation of plastic flow on sample surface. In this study, the dominant wear mechanism observed in all the three samples was micro-ploughing as evidenced by the shifting of material to the sides of the wear tracks. In order to verify the observed wear mechanisms, Hokkirigawa and Kato's empirical relationship for abrasive wear [38, 39] was used to predict the abrasive wear mode. In this model, the degree of penetration, defined by ratio of depth of groove and radius of contact, was calculated for each case. A degree of penetration of 0.12 or lower is indicative of micro-ploughing; values of 0.12-0.18 are indicative of wedge formation and values above 0.18 point to micro-cutting as dominant wear mechanism. At contact pressure of 4.5 GPa, the degree of penetration was 0.11 for air shielded sample and 0.09 for nitrogen shielded sample. The argon shielded sample had a degree of penetration in between those two. These indicate that the dominant wear mechanism is micro-ploughing only, which again consistent with the SEM observations. The higher probability of formation of nitrides and the resulting higher hardness are the main reasons for the better wear resistance of the nitrogen shielded samples. Although air treated samples also had higher hardness and reaction volume, they also had significantly higher surface roughness. Higher surface roughness can be detrimental to wear resistance as observed by Al-Samarai et al.[40]. Nitrogen shielded sample also exhibited a lower wear track width compared to the other samples. The results show similar trend observed by Majumdar et al. [41] in their laser surface melting of tool steel study where they observed 100% nitrogen atmosphere laser melted sample had shown superior wear resistance compared to 100% argon atmosphere sample. All samples showed

a slight increase in mean wear track depth for samples treated at higher scanning velocity. This is attributed to the fact that at higher scanning velocity, there is lower heat input into the material, resulting in lower interaction volume and less enhancement of tribomechanical properties.

3.6 Conclusions

This study provides some insight to proper selection of scanning velocity and shielding gases during laser heat treatment to control the mechanical properties in AISI 8620 steel, which is commonly used in drivetrains. The results showed that it is possible to control RA levels below 10% by proper selection of power density and scanning velocity levels. Phase transformation based hardening occurs in this regime resulting in martensite and RA on the laser treated layer close to the surface. Generated RA% due to laser treatment is higher at lower scanning velocity and with air and nitrogen as a shielding gas compared to argon. The air and nitrogen shielded environments along with lower scanning velocity result in a higher hardness due to combination of deeper interaction volume and higher heat input. Oxygen content in air results higher surface roughness on laser treated sample but air shielded laser treatment showed largest interaction volume. This suggests that, nitrogen and oxygen can be blended to achieve a larger reaction volume along with reasonable surface roughness. However, air shielded samples showed higher friction levels due to shearing of oxide layers and high surface roughness compared to other samples. The nitrogen shielded samples with lower scanning velocity result in the most promising wear resistance behavior which is attributed to nitride formation on surface.

The findings indicate that by proper selection of laser heat treatment parameters such as a nitrogen shielded environment with comparatively lower scanning velocity can result in a

good combination of surface properties such as moderate RA% with higher surface hardness, lower surface roughness and better wear resistance for AISI 8620 steel.

3.7 Acknowledgements

The authors would like to thank Wyman Martinek and Jim Shelledy in the Mechanical Engineering Department for his help with sample preparation, Warren Straszheim in the Materials Analysis and Research Laboratory (MARL) for help with SEM imaging and Scott Schlorholtz for assisting with the XRD measurements. The authors gratefully acknowledge Dr. Cris Schwartz and Mark Placette for allowing to access RTEC tribometer for friction and wear study. Partial funding for this work was provided by a grant from John Deere, Product Engineering Center, Waterloo, Iowa.

3.8 References

1. Breinan, E.M., B.H. Kear, and C.M. Banas, *Processing Materials with Lasers - Laser, Clean Source of Thermal-Energy with High-Power Density, Can Melt Metallic and Ceramic Alloys to Produce Novel and Useful Microstructures - It Also Adapts Well to Automated Processing Techniques.* Physics Today, 1976. **29**(11): p. 44-&.

2. Ion, J.C., *Laser transformation hardening.* Surface Engineering, 2002. **18**(1): p. 14-31.

3. Shi, B. and H. Attia, *Integrated Process of Laser-Assisted Machining and Laser Surface Heat Treatment*. Journal of Manufacturing Science and Engineering-Transactions of the Asme, 2013. **135**(6).

4. Vanbrussel, B.A., et al., *Development of Residual-Stress and Surface Cracks in Laser Treated Low-Carbon Steel.* Scripta Metallurgica Et Materialia, 1991. **25**(4): p. 779-784.

5. Siepak, J., *The Influence of Contact Stress on the Wear of a Carburized Steel Case with a High Content of Retained Austenite.* Wear, 1982. **80**(3): p. 301-305.

6. Kim, H.J. and Y.G. Kweon, *The effects of retained austenite on dry sliding wear behavior of carburized steels.* Wear, 1996. **193**(1): p. 8-15.

7. Roy, S. and S. Sundararajan, *The effect of heat treatment routes on the retained austenite and Tribomechanical properties of carburized AISI 8620 steel.* Surface & Coatings Technology, 2016. **308**: p. 236-243.

8. Lehnhoff, G.R. and K.O. Findley, *Influence of austenite stability on predicted cyclic stress-strain response of metastable austenitic steels.* 11th International Conference on the Mechanical Behavior of Materials (Icm11), 2011. **10**: p. 1097-1102.

9. Xie, Z.J., et al., *Stability of retained austenite in multi-phase microstructure during austempering and its effect on the ductility of a low carbon steel.* Materials Science and Engineering a-Structural Materials Properties Microstructure and Processing, 2014. **603**: p. 69-75.

10. Abareshi, M. and E. Emadoddin, *Effect of retained austenite characteristics on fatigue behavior and tensile properties of transformation induced plasticity steel.* Materials & Design, 2011. **32**(10): p. 5099-5105.

11. Jeddi, D. and H.P. Lieurade, *Effect of retained austenite on high cycle fatigue behavior of carburized 14NiCr11 steel.* Fatigue 2010, 2010. **2**(1): p. 1927-1936.

12. Hu, Z.Z., et al., *The effect of austenite on low cycle fatigue in three-phase steel.* International Journal of Fatigue, 1997. **19**(8-9): p. 641-646.

13. Colaco, R. and R. Vilar, *On the influence of retained austenite in the abrasive wear behaviour of a laser surface melted tool steel.* Wear, 2005. **258**(1-4): p. 225-231.

14. Dogan, O.N., J.A. Hawk, and G. Laird, *Solidification structure and abrasion resistance of high chromium white irons.* Metallurgical and Materials Transactions a-Physical Metallurgy and Materials Science, 1997. **28**(6): p. 1315-1328.

15. Colaco, R., C. Pina, and R. Vilar, *Influence of the processing conditions on the abrasive wear behaviour of a laser surface melted tool steel.* Scripta Materialia, 1999. **41**(7): p. 715-721.

16. Vilar, R., R. Colaco, and A. Almeida, *Laser surface treatment of tool steels.* Laser Processing: Surface Treatment and Film Deposition, 1996. **307**: p. 453-478.

17. Colaco, R. and R. Vilar, *Stabilisation of retained austenite in laser surface melted tool steels.* Materials Science and Engineering a-Structural Materials Properties Microstructure and Processing, 2004. **385**(1-2): p. 123-127.

18. Keskitalo, M., et al., *The influence of shielding gas and heat input on the mechanical properties of laser welds in ferritic stainless steel.* 15th Nordic Laser Materials Processing Conference, Nolamp 15, 2015. **78**: p. 222-229.

19. Li, X., J. Xie, and Y. Zhou, *Effects of oxygen contamination in the argon shielding gas in laser welding of commercially pure titanium thin sheet.* Journal of Materials Science, 2005. **40**(13): p. 3437-3443.

20. Kulka, M., et al., *Wear resistance improvement of austenitic 316L steel by laser alloying with boron.* Surface & Coatings Technology, 2016. **291**: p. 292-313.

21. Piasecki, A., M. Kulka, and M. Kotkowiak, *Wear resistance improvement of 100CrMnSi6-4 bearing steel by laser boriding using CaF2 self-lubricating addition.* Tribology International, 2016. **97**: p. 173-191.

22. Santhanakrishnan, S. and N. Dahotre, *Laser Surface Hardening*, in *ASM Handbook of Heat Treating Irons and Steels*. 2013, American society for Materials (ASM) International: Materials park, Ohio.

23. Yaso, M., et al., *Characteristics of Retained Austenite in Quenched High C-High Cr Alloy Steels.* Materials Transactions, 2009. **50**(2): p. 275-279.

24. Zhao, L., et al., *Magnetic and X-ray diffraction measurements for the determination of retained austenite in TRIP steels.* Materials Science and Engineering a-Structural Materials Properties Microstructure and Processing, 2001. **313**(1-2): p. 145-152.

25. *Standard Practice for X-Ray Determination of Retained Austenite in Steel with Near Random Crystallographic Orientation*, in *ASTM E975-13*.

26. Brown, M.S. and C.B. Arnold, *Fundamentals of Laser-Material Interaction and Application to Multiscale Surface Modification*, in *Laser Precision Microfabrication*. 2010, Springer Series in Materials Science. p. 91-120.

27. Guirado, F. and S. Gali, *Quantitative Rietveld analysis of CAC clinker phases using synchrotron radiation.* Cement and Concrete Research, 2006. **36**(11): p. 2021-2032.

28. Sturm, R., M. Stefanikova, and D.S. Petrovic, *Influence of pre-heating on the surface modification of powder-metallurgy processed cold-work tool steel during laser surface melting.* Applied Surface Science, 2015. **325**: p. 203-210.

29. Roberts, I.A., et al., *A three-dimensional finite element analysis of the temperature field during laser melting of metal powders in additive layer manufacturing.* International Journal of Machine Tools & Manufacture, 2009. **49**(12-13): p. 916-923.

30. Kalyanasundaram, D., P. Shrotriya, and P. Molian, *Fracture mechanics-based analysis for hybrid laser/waterjet (LWJ) machining of yttria-partially stabilized zirconia (Y-PSZ).* International Journal of Machine Tools & Manufacture, 2010. **50**(1): p. 97-105.

31. Goldak, J., A. Chakravarti, and M. Bibby, *A New Finite-Element Model for Welding Heat-Sources.* Metallurgical Transactions B-Process Metallurgy, 1984. **15**(2): p. 299-305.

32. Mixon, D.G. and W.P. Roach, *A thermal model of laser absorption - art. no. 643506.* Optical Interactions with Tissue and Cells XVIII, 2007. **6435**: p. 43506-43506.

33. Hoffman, J., *The absorption coefficients of CO_2-laser radiation for metals and overlays.* Journal of Technical Physics, 1995. **36**(1): p. 11-16.

34. Santhanakrishnan, S. and R. Kovacevic, *Hardness prediction in multi-pass direct diode laser heat treatment by on-line surface temperature monitoring.* Journal of Materials Processing Technology, 2012. **212**(11): p. 2261-2271.

35. Pereira, A., et al., *Laser treatment of a steel surface in ambient air.* Thin Solid Films, 2004. **453**: p. 16-21.

36. Iwao, T., et al., *Oxide-layer thickness effect for surface roughness using low-pressure arc.* Ieee Transactions on Plasma Science, 2006. **34**(4): p. 1223-1228.

37. Svahn, F., A. Kassman-Rudolphi, and E. Wallen, *The influence of surface roughness on friction and wear of machine element coatings.* Wear, 2003. **254**(11): p. 1092-1098.

38. Hokkirigawa, K. and K. Kato, *An Experimental and Theoretical Investigation of Plowing, Cutting and Wedge Formation during Abrasive Wear.* Tribology International, 1988. **21**(1): p. 51-57.

39. Hokkirigawa, K., K. Kato, and Z.Z. Li, *The Effect of Hardness on the Transition of the Abrasive Wear Mechanism of Steels.* Wear, 1988. **123**(2): p. 241-251.

40. Al-Samarai, R.A., et al., *Evaluate the Effects of Various Surface Roughness on the Tribological Characteristics under Dry and Lubricated Conditions for Al-Si Alloy.* Journal of Surface Engineered Materials and Advanced Technology, 2012. **2**: p. 167-173.

41. Majumdar, J.D., A.K. Nath, and I. Manna, *Studies on laser surface melting of tool steel - Part II: Mechanical properties of the surface.* Surface & Coatings Technology, 2010. **204**(9-10): p. 1326-1329.

CHAPTER 4. EFFECT OF RETAINED AUSTENITE ON MICROPITTING BEHAVIOR OF CARBURIZED AISI 8620 STEEL UNDER BOUNDARY LUBRICATION

Modified from a paper under review in *Materialia*

Sougata Roy, George Theng Ching Ooi and Sriram Sundararajan

4.1 Abstract

The objective of this study was to investigate the effect of retained austenite (RA) on the micropitting behavior of carburized AISI 8620 steel under boundary lubrication condition. Samples with RA ranging from approximately 0 to 70% were prepared using specific carburizing schemes. Rolling contact fatigue tests were carried out at maximum contact pressure 1.5 GPa using a benchtop test rig. Samples were subsequently analyzed using noncontact white light profilometry and micro X-Ray Diffraction to observe the evolution of micropitting and RA respectively. An increase in RA% resulted in increased micropitting life. The failure mechanism for the lowest RA samples was dominated by early crack initiation and rapid crack propagation, whereas samples with medium and high RA showed initiation and propagation of micropitting with clear evidence of RA transforming to martensite. Higher levels of RA% to ensure a stable amount remains after this transformation is desirable for extended micropitting life. An extended finite element method (XFEM) which included a Voronoi tessellation to randomly generate the steel microstructure was used to simulate the experiments, and showed that consistent with experimental findings, crack propagation was increasingly hindered in the case of microstructure with increasing RA%.

4.2 Introduction

Micropitting and macropitting or spalling are the two most crucial rolling contact fatigue failure modes observed in drive train components. Various factors contribute to the occurrence of these modes such as slide to roll ratio, slide-to-roll direction, internal defects (crack, void, inclusions) and lubrication conditions. Based on the literature, shallower (less than 10 micron) pits are referred to as micropits and deeper pits (10 to 200 micron) are called macropits or spalls [1]. These two terms are often used indiscriminately when the resulting failure appearance is due to micropitting leading to eventually spalling [2]. Most researchers have observed that micropitting is typically a surface initiated phenomenon [3, 4] but spalling can be surface or sub-surface initiated [5-7]. Tallian mentioned that micropitting is associated to mainly superficial damage but in case of spalling, subsurface fatigue cracks propagate to the surface detaching a significant chunk of material [8].

In modern drivetrain components, sub-surface initiated failures have decreased significantly due to improved manufacturing processes. On the other hand, surface initiated failures have increased significantly, primarily due to reduction in lubricant viscosity and increase in power density [9]. Gears in heavy machinery (i.e. earth moving equipment, agriculture machineries etc.) and wind turbines are run under high load and low speed condition. This boundary lubrication regime promotes surface initiated failures since the surface protection by the lubricant is minimal due to lower film thickness.

Much research has been aimed at alleviating rolling contact fatigue by modifying material properties including retained austenite [10], residual stress [11] and employing different heat treatment techniques [1] and coatings [12]. While recent studies have

focused on the effect of different surface coatings [12, 13] and lubricants [14-17] on micropitting, there is comparatively a dearth of literature that addresses the microstructural implications on micropitting [18]. In case of retained austenite, Rivero and Rudd observed higher initial RA in bearings can lower their service life [19]. On the other hand, Dommarco et al. showed superior rolling contact fatigue life for samples with increased RA [10]. These contradictory results suggest that the role of RA on RCF needs further detailed investigation.

The objective of this study is to investigate the effect of different levels of retained austenite (RA) on the micropitting behavior of carburized AISI 8620 steel under boundary lubrication condition. AISI 8620 steel samples were subjected to different carburizing and tempering techniques to achieve a wide range of retained austenite levels in the samples. Rolling contact fatigue tests were conducted using a designed experimental scheme to evaluate micropitting behavior. A two-dimensional finite element rolling contact fatigue (RCF) model was created to simulate the experiments at different levels of retained austenite and residual stress. The impact of the microstructure on the observed RCF life is discussed.

4.3 Materials

Experiments were conducted on AISI 8620 steel which is widely used in drive train components. Heat treatment schemes can be utilized to vary RA levels on steel samples [20-22]. In this study, RA was varied using different carbon potential (1.2-2%) during carburizing and by varying the tempering schemes. The tempering temperature and time were varied from 50°C for 1 hour to 400°C for 2 hours. All samples were oil quenched at 40°C for 1 hr. between carburizing and tempering steps. Subsequently, the samples were

ground and polished to achieve average surface roughness level 0.22±0.2 μm over a scan size of 1 mm × 0.6 mm.

4.4 Experimental Methods

4.4.1 Retained austenite and residual stress measurement

X-ray diffraction was used to measure retained austenite and residual stress of the samples. To capture phase transformation during our RCF tests using X-ray diffraction (XRD), it was necessary to analyze a 1 mm wide contact zone (see Figure 4.1c). A Rigaku SmartLab XRD with micro-XRD, X-Y mapping stage and hybrid pixel array detector was used to collect data from a 500-micron area on the face-width of sample. A Cu Kα target was used (wavelength 1.54 Å) with a target voltage of 40 KV and current 44 mA. XRD scan data for a range of 40 to 90 degrees (2θ angle) was analyzed using TOPAS software to determine the amount of RA [20, 21]. TOPAS uses the Rietveld method which helps to fit theoretical data to a measured pattern using analytical profile functions & least square methods [23, 24]. Average RA percentage was calculated based on four measurements on each type of sample. The residual stress levels were measured using Cr XRD (wavelength 2.29 Å) with a target voltage of 35KV and current of 1.5 mA. For these measurements, the (211)-peak of Cr Kα radiation was used to determine the peak positions that were used for residual stress determination. The residual stress was calculated based on peak positions measured in 16 different tilt angles (psi) between 0-45° (each 3° apart).

RA and residual stress on the samples prepared by three different heat treatment schemes are mentioned in Table 4.1. For further discussion, these three levels of RA are referred to as 70%, 15% and 0% RA, representing high, medium and low levels of RA

respectively. Increasing carbon potential suppressed martensite start (M_s) and martensite finish (M_f) temperature [22]. This resulted in incomplete conversion of austenite to martensite and helped to increase retained austenite content on surface. Increasing tempering temperature and time helped to convert existing retained austenite to martensite [25].

Table 4.1: RA and residual stress levels on carburized samples

Heat treatment scheme	RA level	RA%	Residual stress (MPa)
2% C potential carburizing with tempering at 50°C for 1 hr.	'High RA' (~70%)	69.7±3.7	155.4±41.9
1.2% C potential carburizing with tempering at 190°C for 1.5 hrs.	'Medium RA' (~15%)	14.5±1.9	268±42.4
1.2%C potential carburizing with tempering at 400°C for 2hrs	'Low RA' (~0%)	0.4±0.2	479.6±15.6

Carburizing helped to generate compressive residual stress on all sample surfaces. High temperature tempering resulted phase transformation of austenite to martensite. This helps in expansion of surface layer due to volumetric expansion during phase transformation. Consequently, higher compressive residual stresses were observed in lower RA samples.

4.4.2 Rolling contact fatigue test

Rolling contact fatigue tests were performed using a Micro Pitting Rig (MPR) from PCS instruments (London, UK) [26]. A schematic representation of the experimental setup is shown Figure 4.1a. The MPR is a computer controlled disc-on-disc contact instrument in which a central roller (sample) is in contact with three harder counter face rings as shown in Figure 4.1b. The roller therefore experiences three contact cycles per revolution at a constant contact pressure. The speeds of the rings and rollers are controlled independently which allows different combinations of rolling and sliding contact. The MPR utilizes a dip lubrication system, with the oil level 27.8 millimeters below the center of the roller and a sump volume of 150 milliliters. The unit is also temperature controlled to maintain the desired operating temperature of the lubricant sump. A chamfered roller with a 1mm face-width (see Figure 4.1c) was used for the tests performed in this study. The diameter for roller was 12 mm and for rings 54.15 mm. The relative amount of rolling and sliding during testing is determined by the slide-to-roll ratio (SRR) and is defined as follows:

$$\text{SRR}\ (\%) = \frac{U_1 - U_2}{1/2(U_1 + U_2)} \cdot 100 \tag{4.1}$$

where U_1 is the speed of the rings and U_2 is the speed of the roller. All tests were conducted using the conditions listed in Table 4.2.

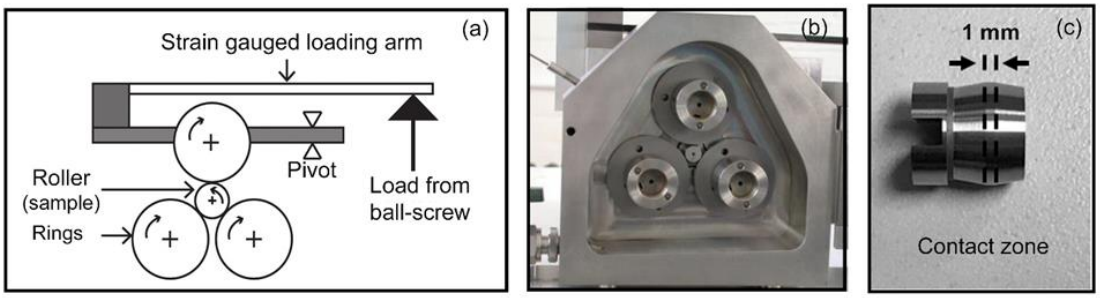

Figure 4.1: a- Schematic diagram of micropitting test rig (MPR); b-Experimental setup of roller and rings inside MPR chamber; c-Representative image of roller (test sample)

Table 4.2: Operating test conditions

Test parameter	
Entrainment velocity (m/sec)	1.75
Slide to roll ratio (%)	20
Normal Load (N)	311
Maximum Hertzian contact pressure (GPa)	1.5
Lubricant sump temperature (°C)	80
Oil film thickness (nm)[a]	80
Lambda ratio	0.16

[a] Estimated using Eq. (4.2)

The lubricating oil used in this study was an API group II base oil with ZDDP anti-wear and other additives, one of which was a viscosity index (VI) improver. Hence the lubricating oil was sheared before testing by running it through a piston pump for 48 hours to ensure no change in viscosity would occur due to shearing during rolling contact fatigue tests. The kinematic viscosity of the sheared oil was 50.51–51.44cSt at 40 °C and 7.56–7.81cSt at 100 °C.

Minimum oil film thickness (H_{min}) for the experiments was calculated using the Pan-Hamrock equation mentioned below,

$$H_{min} = 1.714\, U^{0.694} G^{0.568} W^{-0.128} \qquad (4.2)$$

where, U is dimensionless speed parameter, G is the dimensionless material parameter, and W is the dimensionless load parameter. The film thickness ratio (λ) was calculated using H_{min} and measured initial composite roughness (Rq) to verify tests were run under boundary lubrication.

An accelerometer attached to the instrument provides peak to peak (P/P) and center-line-average (CLA) values of vibration experienced by the roller. Crack propagation and surface deformation during RCF tests lead to increased vibrations. All experiments were run up to 50 million contact cycles or till the system detected a P/P accelerometer signal of 10g, whichever occurred first. Each experiment was associated with a 2-min time duration 'ramp-up' step where the test parameters were ramped to preset conditions (as mentioned in Table 4.2) for the upcoming fatigue step.

4.4.3 Micropitting quantization and characterization

We attempted to quantify the evolution of micropits using non-contact profilometry. The RCF tests were interrupted periodically to analyze the roller samples and quantify the amount of micropitting. The steps used to quantify micropitting are depicted in Figure 4.2. Topographical images from six different locations around the roller circumference (approximately 60° apart) were obtained using interferometry. Each image from these six locations were post-processed using the texture analysis software to detect micropitted regions. In this study, a surface region with depth greater than 1 μm and a contiguous area above 25 μm^2 was considered to be a micropit. For each specific period of RCF cycles, the depth and area information of the micropits based on data from all six locations around the roller circumference were reported as histograms to provide a relatively comprehensive snapshot of the contact surface.

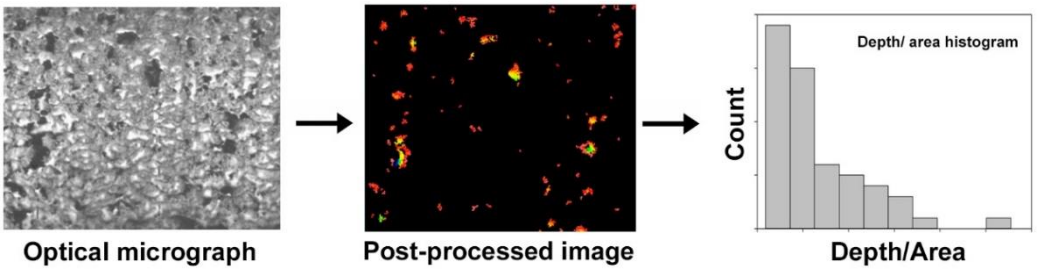

Figure 4.2: Postprocessing protocol to quantize micropitting. An optical image is converted to micropitted regions and subsequently reported as an area/depth histogram.

In addition, an FEI Quanta-250 Scanning Electron Microscope (FESEM) was used to obtain high resolution images of micropits using Back Scattered Electron topography mode with an excitation voltage of 10 kV.

4.4.4 Cross sectional microstructure study

Baseline samples and micropitted samples were cross-sectioned for further metallographic analysis.

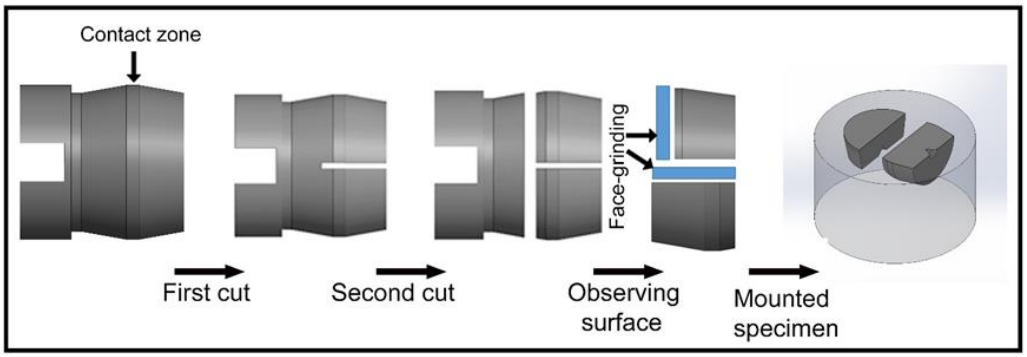

Figure 4.3: Cross-sectioning procedure and mounting of test samples for microstructure study

Figure 4.4 shows the cross-sectional plan to study surface and sub-surface regions of each roller sample. The samples were polished sequentially with 600, 800, 1200 SiC grit papers and subsequently with 3 and 1 μm diamond suspension. In order to reveal the microstructure, the samples were etched with 2.5% nital solution. The microstructure was subsequently observed using a field emission scanning electron microscope.

4.5 Finite Element Modelling

4.5.1 Model Setup

Finite element (FE) modeling was conducted to further investigate the effect of microstructure on rolling contact fatigue (RCF) of carburized AISI 8620 steel. As shown in Figure 4.4a, the finite element model was based on the experimental MPR setup. The setup of a two-dimensional (2D) plane strain RCF model was created in commercial FE software, ABAQUS 6.14 as shown in Figure 4.4b. The dimension of the RCF model is 7*a* (height) by 10*a* (width), where '*a*' represents the half contact width of 100μm to match experimental conditions. The 2D quadrilateral, reduced element (CPE4R) was used in this model. A load corresponding to a maximum Hertzian pressure of 1.5 GPa was applied on the surface with repeated moving distance of 6*a*, in order to simulate the rolling contact between the ring and roller. The Hertzian load was defined by UTRACLOUD user-defined subroutine in ABAQUS. UTRACLOUD was created as a virtual surface load for the purpose of simplifying the simulations, so that the modeling of the ring and the contact interaction between the ring and roller can be eliminated. Residual stress was also incorporated in the model from the contact surface down to a depth of 30 μm, which is the reference zone measured by the XRD in experiment [27].

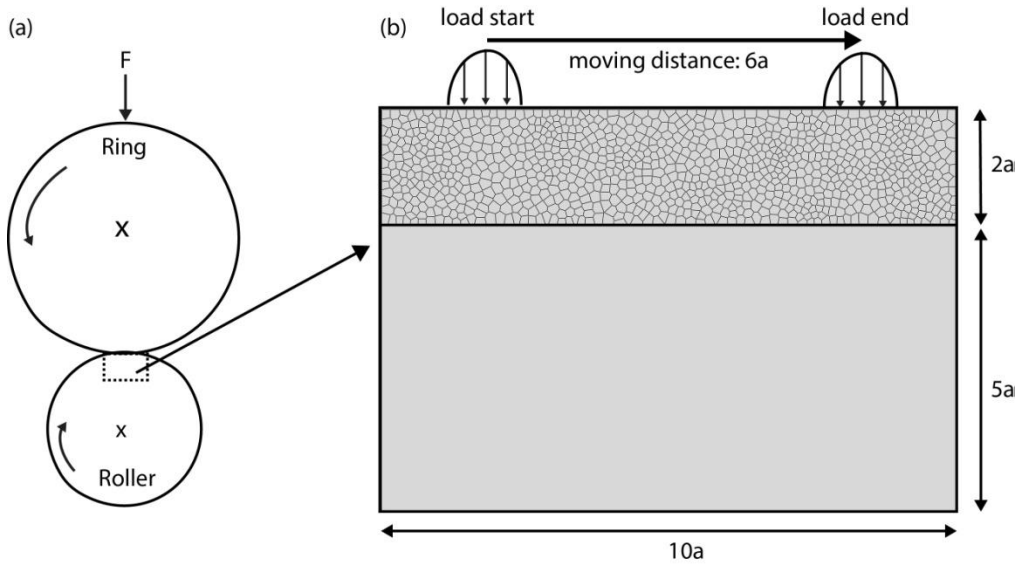

Figure 4.4. Finite element model setup: (a) Schematic diagram of a simplified rolling contact fatigue test from experiment; (b) a two-dimensional rolling contact fatigue model in ABAQUS

4.5.2 Microstructure modeling with Voronoi Tesselation

In order to capture the random nature of microstructure distribution of the material through the modeling approach, Voronoi Tesselation was utilized. Voronoi Tesselation is a mathematical method that divides a space into many regions with a number of convex polygons, which depends on the closest Euclidean distance between the unique seed points and all points in space [28]. Those points in space that are closer to a particular seed point compare to the other seed points form a region or so-called the Voronoi cell. Previous studies have applied Voronoi Tesselation to represent the microstructure within the materials [29-31].

In this study, Voronoi Tesselation was applied at the top part of the area (2*a* x 10*a*) near the contact zone of roller as shown in Figure 4.4b. This area was partitioned into 1000 Voronoi cells with an average grain size of 15 µm [32]. Each cell represents a single

microstructure with different shapes and orientations. Retained austenite and martensite, which were the two phases observed in experiments, were randomly scattered among the 1000 Voronoi cells. The elastic modulus of martensite and austenite used were 228 GPa [33] and 200 GPa [34] respectively. Both of them had the same Poisson's ratio of 0.3. In each simulation, a new randomized Voronoi Tessellation and the scattered distribution of microstructure were generated in MATLAB before importing into ABAQUS.

4.5.3 XFEM and parameters identification

The eXtended finite element method (XFEM) was implemented to model discontinuities such as cracks in ABAQUS. XFEM is an extension of conventional finite element that allows discontinuity to be presented in the elements by implementing the special enriched functions with additional degrees of freedom coupled with the concept of partition of unity [35]. The approximation for a displacement vector function with the partition of unity enrichment consists of a standard finite element and the enrichments, which is shown in the equation below [35]:

$$u = \sum_{I=1}^{N} N_I(x)[u_I + H(x)a_I + \sum_{\propto=1}^{4} F_{\propto}(x)b_I^{\propto}] \quad (4.3)$$

The first term is the continuous part of FE, where $N_I(x)$ is the nodal shape function and u_I is the nodal displacement vector. The second term is for nodes whose shape function support is cut by the crack interior, where $H(x)$ is a discontinuous jump function across crack surfaces. The third term is applied to the nodes whose shape function support is cut by the crack tip [36], where $F_\alpha(x)$ is the elastic asymptotic crack-tip function and b_I^α is the nodal enriched degree of freedom vector. The cohesive segments method and phantom nodes were also applied in the model to simulate moving cracks [37, 38]. Since

the crack propagation cuts through an entire element at a time in ABAQUS, equation (3) can be simplified into:

$$u = \sum_{I=1}^{N} N_I(x)[u_I + H(x)a_I] \tag{4.4}$$

The XFEM-based cohesive segment method was coupled with traction-separation law (TSL), which is defined by a damage initiation criterion and a damage evolution law for degradation of material stiffness. The materials lose their stiffness when the damage initiation criterion reaches 1 within a given tolerance and then followed by the linear damage evolution response [37]. The maximum normal stress criterion (MAXS) is used as the damage initiation criterion whereas the fracture energy dictates the degradation of material stiffness. MAXS for martensite and austenite were set as 225 and 460 MPa respectively with a critical crack length of 10 μm. The fracture energy can be calculated from the fracture mechanics equation:

$$Gc = K_c^2(1 - v^2)/E \tag{4.5}$$

Where K_c is the fracture toughness, v is the Poisson's ratio and E is the elastic modulus. The fracture toughness of martensite and austenite were assumed to be 17.6 and 33 MPa-m½ respectively [39, 40]. In this model, the simulations were started with a subsurface initial crack in order to accelerate the process to failure and ended when the cracks reached the surface or with a number of 800 contact cycles, whichever came first. Cracks were induced along the grain boundaries but cracks could propagate along an arbitrary, solution dependent path depending on the weakest points in materials where damage initiation occurred [37]. A new, randomly selected crack was created in each simulation with an average initial crack length of 10 μm.

4.6 Results and discussion

4.6.1 Effect of retained austenite during rolling contact fatigue

Table 4.3 shows the results of the RCF tests. Samples with three different levels of RA exhibited very distinct RCF life, with increasing levels RA resulting in increased life. 15% RA provided an enhancement of about 5 times compared to the 0% RA sample. 70% RA exhibited about 12 times the life compared to 0% RA. Despite having the lowest initial residual stress, the 70% RA sample showed the best micropitting life. While it has been previously observed that both RA and residual stress help to enhance RCF life [10, 11], the results in this study suggest that the initial RA content plays a much more significant role in affecting micropitting behavior compared to the initial residual stress.

Table 4.3: Rolling contact fatigue life (P/P accelerometer to reach 10g)

Sample		RCF life
70% RA	Test 01	> 50 million
	Test 02	> 50 million
15% RA	Test 01	15 million
	Test 02	17.5 million
0% RA	Test 01	4 million
	Test 02	2.5 million

Figure 4.5 shows a representative evolution of the accelerometer P/P signal and the surface condition for all the samples during RCF testing. Figure 4.5a shows the image of the surface prior to tests (baseline condition). Initially, run-in occurred for all samples during the first 0.01 million cycles during which the surface roughness (Ra) dropped significantly. The accelerometer signal in Figure 4.5b shows no change for all samples during this run-in period. After that there was an incubation period when the surface

changed with number of cycles but without formation of any significant micropits or cracks. The accelerometer signal showed a flat response during this period as well. In case of the 0% RA sample, the incubation period lasted to about 0.3 million cycles and then started to increase quickly. For 15% RA sample, this period lasted around 1.1 million cycles and for 70% RA sample it was above 5 million cycles. In case of 0% RA sample, the signal reached the 10g trip limit within 4 million cycles. The increase in the accelerometer signal was a result of transverse cracks forming early on the surface (Figure 4.5b). These samples then exhibited rapid crack propagation to failure, since there was almost no RA.

Figure 4.5c shows that beyond 2 million cycles the 15% RA samples exhibited a gradual increase in the accelerometer signal and eventually reached the trip limit of 10g around 15 million cycles. Surfaces exhibited micropits with the amount of micropitting increasing after 5 million cycles. In case of the 70% RA samples, the accelerometer signal increased slightly between 5-10 million cycles after which it stabilized and remained stable up to 50 million cycles at which point the tests were stopped. Micropitting was observed in these samples after 5 million cycles similar to the 15% RA samples but unlike those samples micropitting did not increase over time for the 70% RA samples.

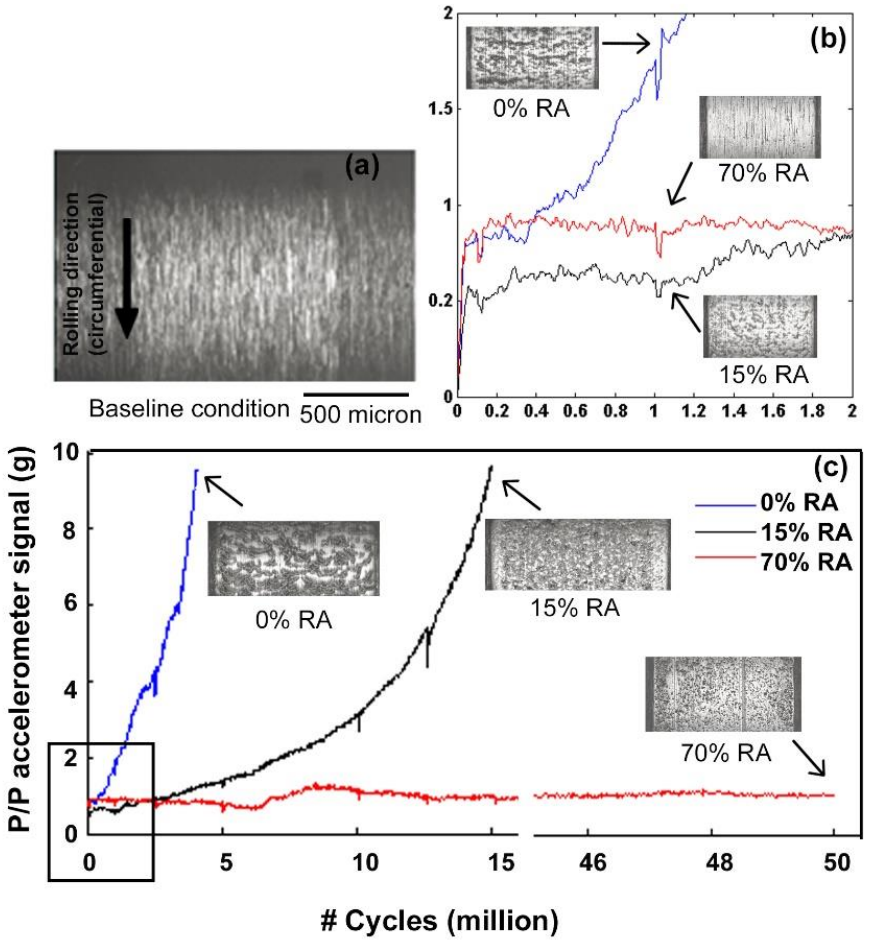

Figure 4.5: Evolution of different RA roller samples at different phase of their RCF life including P/P accelerometer signal: (a) Optical micrograph of roller surface after 1 million cycles and P/P accelerometer signal till 2 million cycles (b) optical micrograph of roller surface at baseline condition (c) Optical micrograph of roller surface at the end of their RCF life

To verify these visual observations, we quantified the evolution of micropits using non-contact profilometry. Figure 4.6 shows a histogram of the number of micropits as a function of depth and area for the 15% and 70% RA samples at 5, 10 and 15 million cycles. Recall that the analysis counts regions with a depth greater than 1 μm and a contiguous area of more than 25 μm^2 as micropits. It can be observed that, at 5 million

cycles both samples displayed micropits less than 3 μm deep and less than 100 μm^2 in area. The 70% RA sample exhibited comparatively more number of pits than the 15% RA sample at this stage of testing. Micropits became deeper, larger and increased in number with number of cycles for both samples. At 10 million cycles, the 15% RA sample showed comparatively lesser number of pits with larger depth and size as compared to the 70% RA sample. However, the maximum size of micropits for 70% RA sample was around half of the size of the large micropits in 15% RA sample. The 70% RA sample exhibited three times the number of micropits with area below 60 μm² compared to the 15% RA sample.

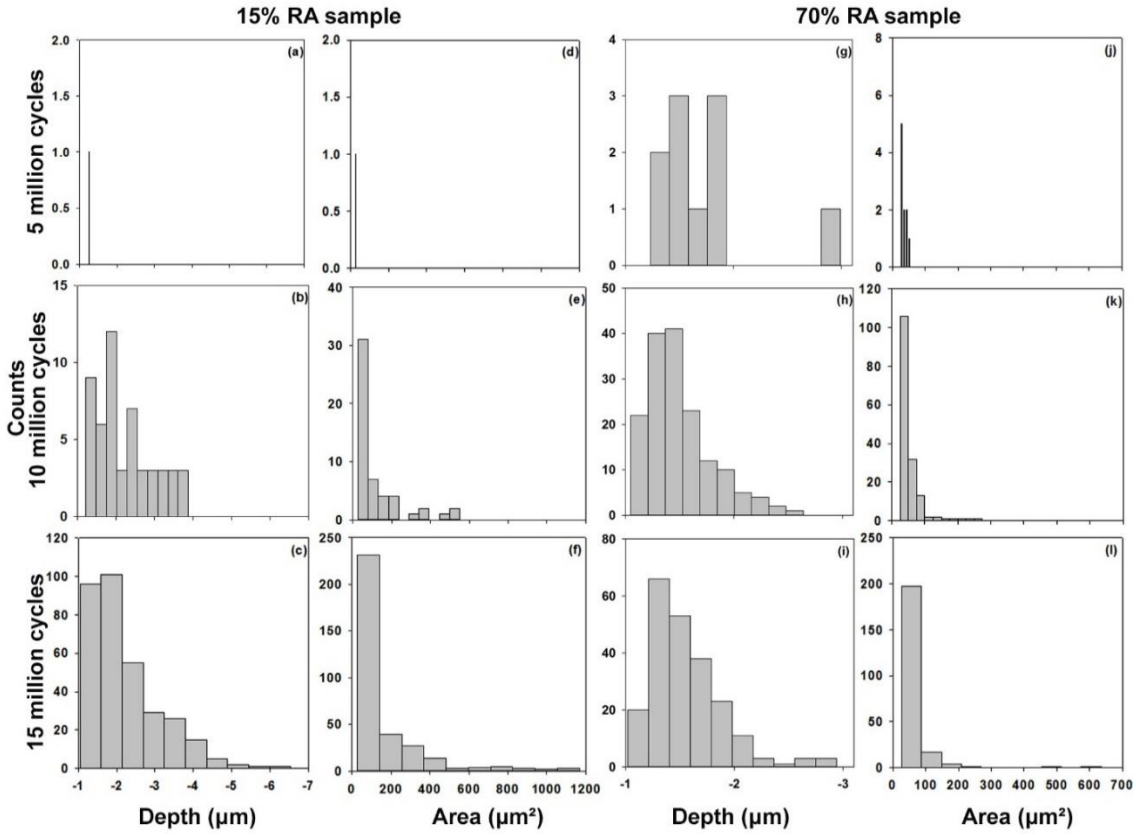

Figure 4.6: Micropits depth and area histogram after 5, 10 and 15 million cycles for 15% RA and 70% RA samples

At 15 million cycles, the micropits in the 15% RA sample propagated rapidly leading to a large number of micropits with depths up to 6.5 μm and area above 1100 μm^2. In case of 70% RA sample, the micropits stabilized after 10 million cycles and didn't grow in size like the 15% RA sample. The observations from the histogram study confirms a good correlation between increase in pit size and depth and increase in the P/P accelerometer signal shown in Figure 4.5 for the various samples.

4.6.2 Morphology of micropitting on different samples

Figure 4.7 shows scanning electron microscopy images of micropitted surfaces for different RA samples. The BSE images help understand the characteristics of the micropits and surface damage. For the 0% RA sample, the images clearly show transverse directional cracks. In some areas, where multiple cracks coalesce, occurrence of pitting was also observed. Due to almost no RA, these samples failed due to early crack initiation and rapid crack propagation. For 15 % and 70% RA samples, the occurrence of micropitting was confirmed. Micropitting usually begins by attacking high points on surface by localized plastic deformation at those asperities. Eventually they coalesce each other and grow bigger in size and depth. In its initial phase, it forms numerous microscale cracks close to the surface. These cracks later propagate from the surface to the bulk at a shallow angle until rupture occurs to form a pit of shallow depth (generally less than 10 μm) pit on surface. As also observed in the histogram data (Figure 4.6), Figure 4.7 shows that in the case of the 15% RA samples, the pit sizes were larger but the number of pits was less compared to the 70% RA samples.

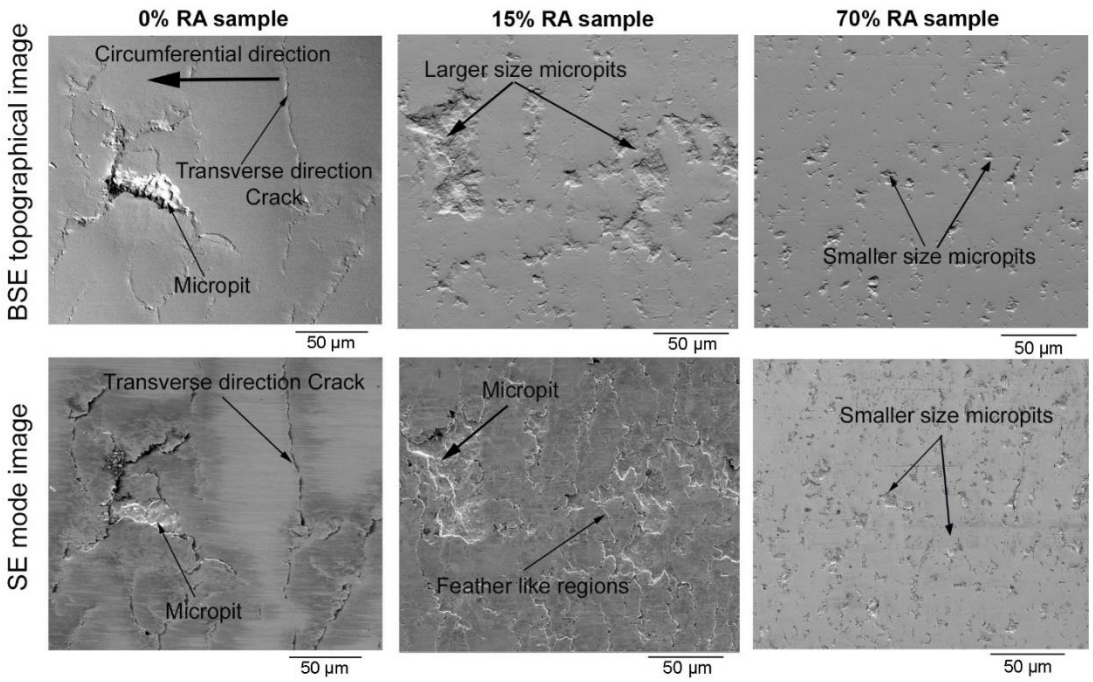

Figure 4.7: BSE topographical and SE images of micropitted regions on sample surface

In secondary electron mode, the damaged surface show featherlike edges beside micropit craters. The featheredge forms the back of the crater due to plastic flow of material over the crater rim. The feather edge appears white under SEM due to charging of electron on those uneven areas [41]. Transverse directional cracks were significantly less in 70% RA sample compared to the 15 % and 0% RA samples.

4.6.3 Phase transformation

Figure 4.8 shows the evolution of the RA in the samples as a function of contact cycles, as measured using micro-XRD. In the case of the 15% RA samples, almost all RA was transformed to martensite within 0.01 million cycles.

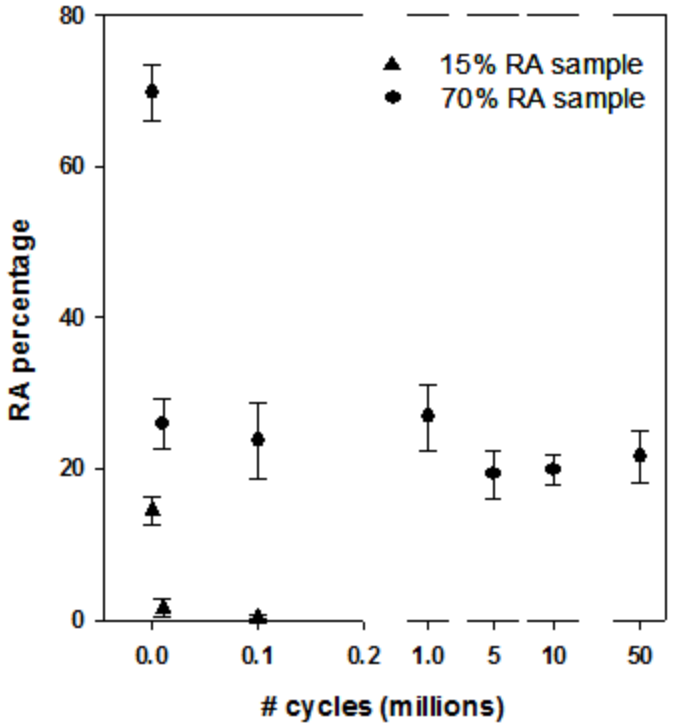

Figure 4.8: Evolution of RA during micropitting test for medium RA sample. Error bars represent 90% confidence intervals

For 70% RA samples, the maximum phase transformation occurred in first 0.01 million cycles as well. This suggests that there is a breaking-in or running-in period during which the maximum amount of austenite to martensite phase transformation occurs [42]. This is consistent with previous observations reported by Dommarco et al. [10]. Subsequently, in the case of the 70% RA samples, the RA amount stabilizes at approximately 20% after 5-10 million cycles. This is the point beyond which the 70% RA sample begins to show stabilized levels of micropit formation and subsequent enhanced life compared to the 15% RA sample. The stabilized 20% RA in the microstructure helped improve micropitting life in two ways. First, inherent ductility of RA helps to delay crack growth by blunting tips of crack while growing. Second, martensitic phase transformation can

generate increased compressive residual stresses in the case depth, which also contribute to delayed crack growth by promoting crack closure.

4.6.4 Microstructural observation

The baseline and post experiment microstructure for all three levels of RA samples are depicted in Figure 4.9. Prior to experiments, samples showed blocky islands of RA and needle like martensite zones. MnS based inclusions were also detected in all samples. These inclusions are sometimes added to steel microstructure intentionally to increase machinability of steel [43]. In case of the 0% RA sample, high temperature tempering transformed remaining austenite to martensite. Martensite is formed by a shear mechanism where many atoms moves cooperatively and almost simultaneously. It has been previously observed that the high carbon plate martensite is sensitive to micro cracking due to the non-parallel plate formation [44]. The micro cracks are generally formed in the largest martensite plates. Our 0% RA samples exhibited such microcracks in the martensite plate regions as shown in Fig 10. For 15% RA samples, no internal cracks were observed. In the case of the 70% RA samples, long internal subsurface cracks were observed in some regions. Due to the high carbon potential carburizing for the 70% RA samples, carbide precipitation at grain boundary regions occurred. Generally, stress concentration occurs at the sharp or uneven edges of carbide particles and this may result in micro-crack initiation [45].

In all samples, the surface initiated cracks propagated in the contact surface motion direction at a shallow angle to the surface, consistent with previous observations [5, 46]. Generally, these surface generated cracks initiate at plastically deformed high asperity zones and propagate in the contact surface motion direction [9]. After travelling some

distance, they change their direction and turn back towards surface. This causes delamination or pit formation on surface leading to micropits.

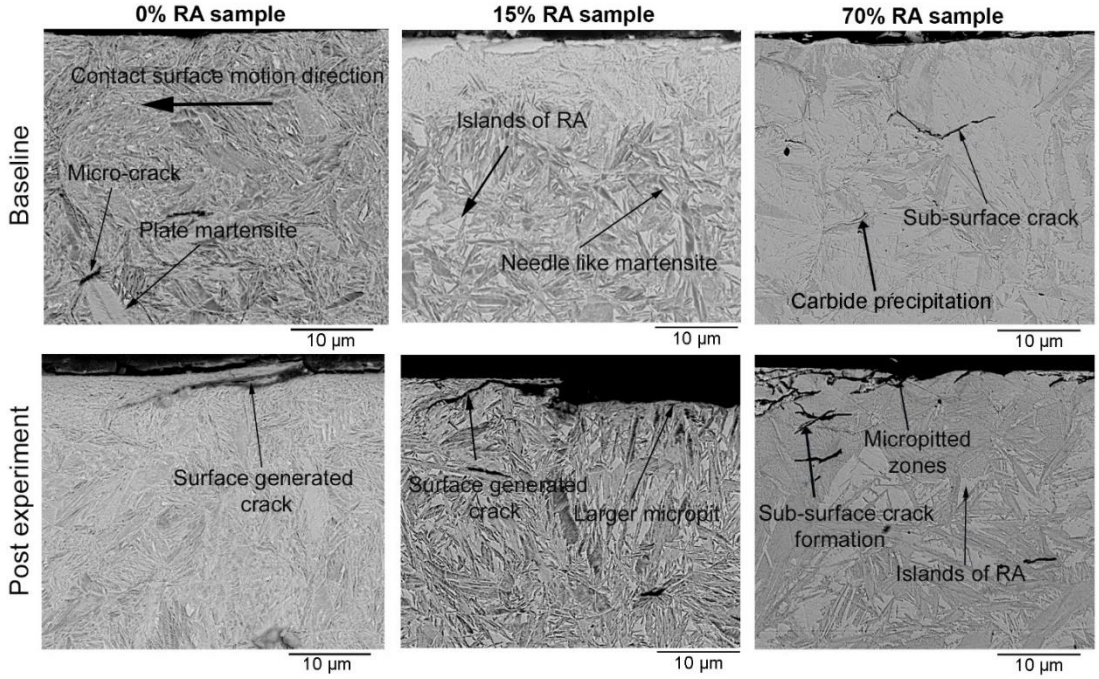

Figure 4.9: SEM micrograph of cross sections of the samples at baseline and post experiment condition

After being subjected to RCF tests, the 70% RA samples exhibited less blocky zones close to the surface compared to the baseline condition which point to martensitic phase transformation during the tests. Several subsurface crack formations were also observed mainly in the 15% and 70% RA samples. Due to the rapid failure of low RA samples, sub-surface crack formation was not observed. Although the 70% RA samples had subsurface cracks, they showed maximum life. This also suggests that the observed micropitting is most likely surface generated failure mode and high RA content impedes sub-surface crack growth.

4.6.5 Modeling results

The finite element modeling focused on evaluating the impact of RA on sub-surface crack growth. The simulations were based on the amount of RA and residual stress measured and the parameters provided in the experiments which were 0% RA with 500 MPa compressive residual stress; 15% RA with 285 MPa compressive residual stress and 70% RA with 155 MPa compressive residual stress. A total of 9 simulations for each case were performed at randomly located sub-surface crack locations. These crack locations were at 3 different depths (0.25a, 0.5a and 0.75a) from the surface with a repetition of 3 at each depth.

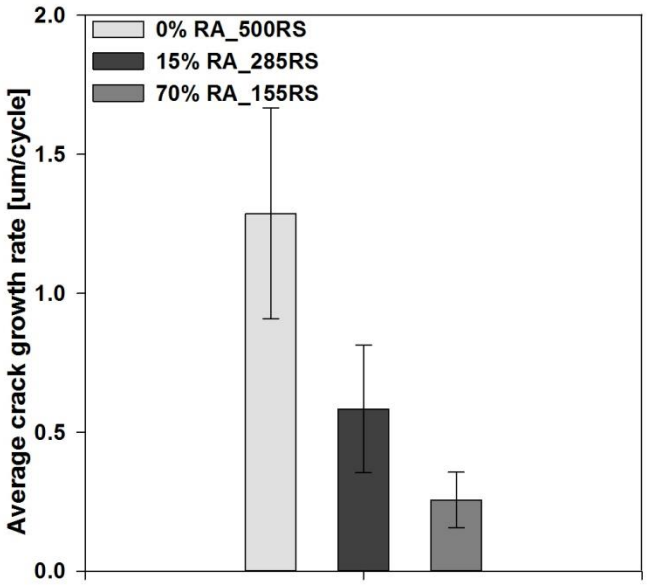

Figure 4.10: The average crack growth rate in (a) 0 RA% with 500 MPa RS; (b) 15% RA with 285 MPa RS; and (c) 70% RA with 155 MPa. RA= retained austenite and RS = compressive residual stress. Error bars represent 90% confidence intervals.

Figure 4.10 shows the average crack propagation rate measured from beginning to the end of simulations for the three samples. The average crack propagation rate decreases as

the level of RA increases from 0% to 70%. The results indicate that increasing level of RA mitigates crack propagation. While the failures observed in the experiments were surface initiated, the simulation nevertheless shows that increasing RA mitigates crack propagation, contributing to higher RCF life, consistent with experimental results.

4.7 Conclusions

Steel samples with an RA range of 0-70% were prepared to evaluate the effect of RA on micropitting by varying carbon potential (1.2 to 2%) and tempering temperature and time. Experiments revealed that increasing RA% contributed to significant increase in micropitting life. The failure mechanism for the lowest RA samples was dominated by early crack initiation and rapid crack propagation, whereas samples with medium and high RA showed initiation and propagation of micropitting with clear evidence of RA transforming to martensite. It was observed that in case of 70% RA samples the RA was transformed to around 20% in 5 million cycles after which the transformation stabilized. Evolution of the phase transformation indicated that at 15% RA, almost all the RA is transformed to martensite within 10^4 cycles. XFEM simulations showed that higher amounts of RA delays fatigue crack growth and therefore micropitting life is improved. Secondly, inherent ductility of austenite also plays a beneficial role to delay crack initiation and propagation. Although 70% retained austenite sample exhibited the lowest compressive residual stress, it showed the maximum micropitting life. This indicates that the role of retained austenite had greater impact than that of initial residual stress in affecting the micropitting life. Thus, ensuring a sufficiently high level of RA% at the start to enable a stable level remains after martensitic transformation is desirable for improved micropitting life.

Overall, the findings provide valuable input for the design and manufacturing of drivetrain components for a wide range of applications under low lambda conditions ranging from agricultural equipment to the wind energy sectors.

4.8 Acknowledgements

The authors would like to thank Matt Smeeth from PCS Instruments and Ian Griffin from Wallwork for their help with sample preparation, Warren Straszheim in the Materials Analysis and Research Laboratory (MARL) for help with SEM imaging and Erina Kagami in Rigaku Corporation for assisting with the XRD measurements. Partial funding for this work was provided by John Deere Product Engineering Center in Waterloo, Iowa and Iowa State University.

4.9 References

1. D'Errico, F., *Micropitting Damage Mechanism on Hardened and Tempered, Nitrided, and Carburizing Steels.* Materials and Manufacturing Processes, 2011. **26**(1): p. 7-13.

2. Alban, L.E., *Systematic Analysis of Gear Failure*. 1985: ASM International: Metals Park, OH.

3. Clarke, A., H.P. Evans, and R.W. Snidle, *Understanding micropitting in gears.* Proceedings of the Institution of Mechanical Engineers Part C-Journal of Mechanical Engineering Science, 2016. **230**(7-8): p. 1276-1289.

4. Brandao, J.A., J.H.O. Seabra, and J. Castro, *Surface initiated tooth flank damage. Part II: Prediction of micropitting initiation and mass loss.* Wear, 2010. **268**(1-2): p. 13-22.

5. Santus, C., et al., *Surface and subsurface rolling contact fatigue characteristic depths and proposal of stress indexes.* International Journal of Fatigue, 2012. **45**: p. 71-81.

6. Ding, Y. and J.A. Gear, *Spalling depth prediction model.* Wear, 2009. **267**(5-8): p. 1181-1190.

7. Ding, Y. and N.F. Rieger, *Spalling formation mechanism for gears.* Wear, 2003. **254**(12): p. 1307-1317.

8. Tallian, T.E., *Failure Atlas for Hertz Contact Machine Elements*. 1992: ASME Press: New York.

9. Rycerz, P., A. Olver, and A. Kadiric, *Propagation of surface initiated rolling contact fatigue cracks in bearing steel.* International Journal of Fatigue, 2017. **97**: p. 29-38.

10. Dommarco, R.C., et al., *Residual stresses and retained austenite evolution in SAE 52100 steel under non-ideal rolling contact loading.* Wear, 2004. **257**(11): p. 1081-1088.

11. Shen, Y., et al., *Effect of retained austenite - Compressive residual stresses on rolling contact fatigue life of carburized AISI 8620 steel.* International Journal of Fatigue, 2015. **75**: p. 135-144.

12. Mahmoudi, B., et al., *Influence of a WC/a-C:H Coating on Micropitting Wear of Bearing Steel.* Tribology & Lubrication Technology, 2015. **71**(4): p. 24-27.

13. Bakoglidis, K.D., et al., *Rolling performance of carbon nitride-coated bearing components in different lubrication regimes.* Tribology International, 2017. **114**: p. 141-151.

14. Soltanahmadi, S., et al., *Investigation of the effect of a diamine-based friction modifier on micropitting and the properties of tribofilms in rolling-sliding contacts.* Journal of Physics D-Applied Physics, 2016. **49**(50).

15. Moallem, H., S. Akbarzadeh, and A. Ariaei, *Prediction of micropitting life in spur gears operating under mixed-lubrication regime using load-sharing concept.* Proceedings of the Institution of Mechanical Engineers Part J-Journal of Engineering Tribology, 2016. **230**(5): p. 591-599.

16. Wei, J., A.Q. Zhang, and P. Gao, *A study of spur gear pitting under EHL conditions: Theoretical analysis and experiments.* Tribology International, 2016. **94**: p. 146-154.

17. Soltanahmadi, S., et al., *Tribochemical study of micropitting in tribocorrosive lubricated contacts: The influence of water and relative humidity.* Tribology International, 2017. **107**: p. 184-198.

18. Evans, R.D., et al., *Influence of Steel Type on the Propensity for Tribochemical Wear in Boundary Lubrication with a Wind Turbine Gear Oil.* Tribology Letters, 2010. **38**(1): p. 25-32.

19. Rivero, I.V. and C.O. Ruud, *Deviation of residual stress patterns in 52100 bearing steel due to inherent microstructural transformations after rolling contact.* Materials Characterization, 2004. **53**(5): p. 381-393.

20. Roy, S. and S. Sundararajan, *The effect of heat treatment routes on the retained austenite and Tribomechanical properties of carburized AISI 8620 steel.* Surface & Coatings Technology, 2016. **308**: p. 236-243.

21. Roy, S., et al., *Effect of laser treatment parameters on surface modification and tribological behavior of AISI 8620 steel.* Tribology International, 2017. **112**: p. 94-102.

22. Kim, H.J. and Y.G. Kweon, *The effects of retained austenite on dry sliding wear behavior of carburized steels.* Wear, 1996. **193**(1): p. 8-15.

23. Bruker, *TOPAS V4.2 User's Manual*. 2009.

24. Evans, M.H., *An updated review: white etching cracks (WECs) and axial cracks in wind turbine gearbox bearings.* Materials Science and Technology, 2016. **32**(11): p. 1133-1169.

25. Verhoeven, J.D., *Steel Metallurgy for the Non-Metallurgist*. 2007: ASM International.

26. Jenson, A.D., S. Roy, and S. Sundararajan, *The evolution of hardness and tribofilm growth during running-in of case carburized steel under boundary lubrication.* Tribology International, 2018. **118**: p. 1-10.

27. Prevey, P.S., *X-ray diffraction residual stress techniques.* ASM International, ASM Handbook., 1986. **10**: p. 380-392.

28. Okabe, A., *Spatial tessellations*. 1992: Wiley Online Library.

29. Nygards, M. and P. Gudmundson, *Three-dimensional periodic Voronoi grain models and micromechanical FE-simulations of a two-phase steel.* Computational Materials Science, 2002. **24**(4): p. 513-519.

30. Bruckner-Foit, A. and X.Y. Huang, *Numerical simulation of micro-crack initiation of martensitic steel under fatigue loading.* International Journal of Fatigue, 2006. **28**(9): p. 963-971.

31. Slack, T. and F. Sadeghi, *Explicit finite element modeling of subsurface initiated spalling in rolling contacts.* Tribology International, 2010. **43**(9): p. 1693-1702.

32. Giordani, T., et al., *Mechanical and Metallurgical Evaluation of Carburized, Conventionally and Intensively Quenched Steels.* Journal of Materials Engineering and Performance, 2013. **22**(8): p. 2304-2313.

33. Hatem, T.M. and M.A. Zikry, *Shear pipe effects and dynamic shear-strain localization in martensitic steels.* Acta Materialia, 2009. **57**(15): p. 4558-4567.

34. Hatem, T.M. and M.A. Zikry, *A model for determining initial dislocation-densities associated with martensitic transformations.* Materials Science and Technology, 2011. **27**(10): p. 1570-1573.

35. Melenk, J.M. and I. Babuska, *The partition of unity finite element method: Basic theory and applications.* Computer Methods in Applied Mechanics and Engineering, 1996. **139**(1-4): p. 289-314.

36. Belytschko, T. and T. Black, *Elastic crack growth in finite elements with minimal remeshing.* International Journal for Numerical Methods in Engineering, 1999. **45**(5): p. 601-620.

37. ABAQUS, V., *6.14 Documentation*. 2014, Dassault Systemes Simulia Corporation.

38. Remmers, J.J.C., R. de Borst, and A. Needleman, *The simulation of dynamic crack propagation using the cohesive segments method.* Journal of the Mechanics and Physics of Solids, 2008. **56**(1): p. 70-92.

39. *440C Martensitic Stainless Steel (UNS S44004)*. Available from: http://www.matweb.com/search/datasheet.aspx?matguid=850c5024f8d844af8ef95afab1a08792.

40. *AISI 8620 Steel, carburized, box cooled, reheated and double quenched, 150°C (300°F) temper, 13 mm (0.5 in.) round*.

41. Errichello, R.L., *Morphology of Micropitting*. 2012: Gear Technology. p. 75-81.

42. Sadeghi, F., et al., *A Review of Rolling Contact Fatigue.* Journal of Tribology-Transactions of the Asme, 2009. **131**(4).

43. Aring;nmark, N., A. Karasev, and P.G. Jonsson, *The Effect of Different Non-Metallic Inclusions on the Machinability of Steels.* Materials, 2015. **8**(2): p. 751-783.

44. Marder, A.R., Benscote.Ao, and G. Krauss, *Microcracking Sensitivity in Fe-C Plate Martensite.* Metallurgical Transactions, 1970. **1**(6): p. 1545-&.

45. Wang, Y.H., et al., *Rolling Contact Fatigue Performances of Carburized and High-C Nanostructured Bainitic Steels.* Materials, 2016. **9**(12).

46. Moorthy, V. and B.A. Shaw, *An observation on the initiation of micro-pitting damage in as-ground and coated gears during contact fatigue.* Wear, 2013. **297**(1-2): p. 878-884.

CHAPTER 5. CORRELATION BETWEEN EVOLUTION OF SURFACE ROUGHNESS PARAMETERS AND MICROPITTING OF CARBURIZED STEEL UNDER BOUNDARY LUBRICATION CONDITION

Modified from a paper accepted in *Surface and Coatings Technology*

Sougata Roy, Derek White and Sriram Sundararajan

5.1 Abstract

This paper investigates the evolution of amplitude and spatial roughness parameters during rolling contact fatigue experiments on carburized samples with around 0%, 15% and 70% retained austenite (RA) under boundary lubrication condition. The 0% RA samples failed due to early crack initiation and rapid crack propagation. The 15% and 70% RA samples showed initiation and propagation of micropitting. Four amplitude surface parameters (R_a, R_{RMS}, R_{sk} and R_{ku}) and one spatial parameter (2D auto-correlation length) were analyzed for correlations between micropitting initiation and propagation during RCF cycles. It was observed that during run-in, a significant decrease in R_a and R_{RMS} were observed, while the correlation length increased and stabilized for all samples. The evolution of the 2D autocorrelation length correlated well with the evolution of crack propagation. It was observed that, while R_a and R_{RMS} values follow the same trend as propagation of micropitting, skewness and kurtosis can be used to better predict initiation and propagation of micropitting on the surface. Significant propagation of micropitting was accompanied by a decreasing trend of skewness and increasing trend of kurtosis. Transverse directional correlation length also showed good correlation with propagation of micropitting, with the correlation length decreasing during increase of micropitting on sample surfaces.

5.2 Introduction

Rolling contact fatigue (RCF) is the failure process of a hardened surface subjected to cyclic loading as it undergoes sliding-rolling contact with its mating surface. Depending on the contact condition, different failure modes such as micropitting, macropitting, scuffing, and wear can be observed as a result of RCF [1]. Micropitting is one of the most prevalent RCF failure modes for drivetrain components such as gear and bearings [2]. The process consists of the accumulation of surface stresses at small-scale asperities which results in localized surface damage. Eventually it leads to generation of microscale cracks that initiate at or close to the surface. These cracks then propagate at shallow angle from the surface into the material. Finally, it deviates its direction and ruptures through the surface causing damage in the form of micron size pits [3]. Research on micropitting has focused on understanding the effect of different surface coatings [2, 4], lubricants [5-8] and material aspects [9] on micropitting. It has been observed that surface roughness parameters are very crucial factors to impact micropitting life [10-13]. Clarke et al. studied evolution of asperity heights during run-in and micropitting of steel surfaces under mixed lubrication conditions [14]. They observed that surface modification was limited to the asperity tips of the surface. Most of these studies concentrated on the impact of baseline surface roughness parameters on micropitting and there is comparatively a dearth of literature that addresses the evolution of surface roughness parameters during micropitting.

When analyzing a sample's surface, it is common practice to provide the primary amplitude parameters such as average roughness (Ra) or the root mean square average (R_{RMS}). However, the amplitude parameters alone might not be sufficient enough for the complete

characterization of a surface [15] and spatial parameters are required as well. A random and isotropic surface can be completely characterized by two functions — the height distribution and autocorrelation functions [16]. Spatial characteristics include the areal autocorrelation function (AACF) and areal power spectrum density (APSD) [17, 18] The AACF is particularly useful when testing for isotropy, and in the case of this study, for tracking surface evolution due to micropitting. For a residual surface η(x,y) the AACF can be defined accordingly:

$$R(\tau_x, \tau_y) = \lim_{l_x, l_y \to \infty} \frac{1}{4 l_x l_y} \int_{-l_y}^{l_y} \int_{-l_x}^{l_x} \eta(x, y) \eta(x + \tau_x, y + \tau_y) dx\, dy \tag{5.1}$$

In brief, the AACF is the convolution of the surface with itself and from it, a characteristic length known as the fastest decay autocorrelation length (S_{al}) can be extracted. This quantity describes the distance between two points on a surface at which there is no longer statistically significant correlation. That is, for a random surface, the AACF decays rapidly in all directions and the S_{al} is relatively short whereas a ground surface with a defined lay will exhibit a rapid decay and periodicity against the lay and exhibit a substantially longer S_{al} along the lay.

The paper examines the evolution of amplitude and spatial roughness parameters of steel samples during rolling contact fatigue (RCF) experiments under boundary lubrication conditions. Samples were prepared with different levels of retained austenite (RA) to influence the failure mode and the surface evolution during the RCF tests. Correlations between the initiation and propagation of micropitting and changes in the surface roughness parameters are discussed.

5.3 Materials

Experiments were conducted on AISI 8620 steel which is a widely used material in drive train components. The amount of retained austenite (RA) in steel can influence the performance of the material and is often a specification in industrial applications. Heat treatment schemes can be utilized to vary RA levels on steel samples [19-21]. In this study, RA was varied using different carbon potentials during carburizing and by varying the tempering schemes. Heat treatment schemes to prepare samples with different RA levels are mentioned in Table 5.1.

Table 5.1: Heat treatment schemes and resulting RA levels in samples

Heat treatment scheme	RA level	RA%
2% C potential carburizing with tempering at 50°C for 1 hr.	'High RA'	69.7±3.7 (~70%)
1.2% C potential carburizing with tempering at 190°C for 1.5 hrs.	'Medium RA'	14.5±1.9 (~15%)
1.2%C potential carburizing with tempering at 400°C for 2hrs	'Low RA'	0.4±0.2 (~0%)

The carbon potential was varied from 1.2 to 2% during carburizing while the tempering temperature and time were varied from 50°C for 1 hour to 400°C for 2 hours. All samples were oil quenched at 40°C for 1 hr. between the carburizing and tempering step. Increasing carbon potential results in decreased martensite start (M_s) and martensite finish (M_f) temperature [21]. This results in incomplete conversion of austenite to martensite and helps to increase retained austenite content on surface. Increasing tempering temperature and

time help to convert existing retained austenite to bainite or pearlite depending on tempering time and temperature [22]. A Rigaku SmartLab micro-XRD with X-Y mapping stage and hybrid pixel array detector was used to measure the baseline RA levels on samples. The heat treatment schemes resulted in samples with RA levels of approximately 70%, 15% and 0%. These three levels are referred to as high, medium and low-level RA samples respectively. The samples were subsequently ground and polished to achieve an average surface roughness level of 0.22 ±0.02 μm over a scan size of 1 mm × 0.6 mm.

5.4 Methods

5.4.1 Rolling contact fatigue test

Rolling contact fatigue (RCF) tests were performed using a Micro Pitting Rig (MPR) by PCS instruments (London, UK) [23]. A schematic representation of the experimental setup is shown Figure 5.1a. The MPR is a computer controlled disc-on-disc contact instrument in which a central roller (sample) is in contact with three harder counter face rings in a planetary configuration as shown in Figure 5.1b. The roller therefore experiences three contact cycles per revolution at a constant contact pressure. The speeds of the rings and rollers are controlled independently which allows different combinations of rolling and sliding contact. The MPR utilizes a dip lubrication system, with the oil level 27.8 millimeters below the center of the roller and a sump volume of 150 milliliters. The unit is also temperature controlled to maintain the desired operating temperature of the lubricant sump. A chamfered roller with face-width 1mm (see Figure 5.1c) was used for the tests performed in this study. The diameter for roller and rings were 12 mm and 54.15 mm respectively.

The relative amount of rolling and sliding is determined by the slide-to-roll ratio (SRR) and is defined as follows:

$$\text{SRR}\ (\%) = \frac{U_1 - U_2}{{}^1\!/_2 (U_1 + U_2)} \cdot 100 \tag{5.2}$$

where U_1 is the speed of the rings and U_2 is the speed of the roller.

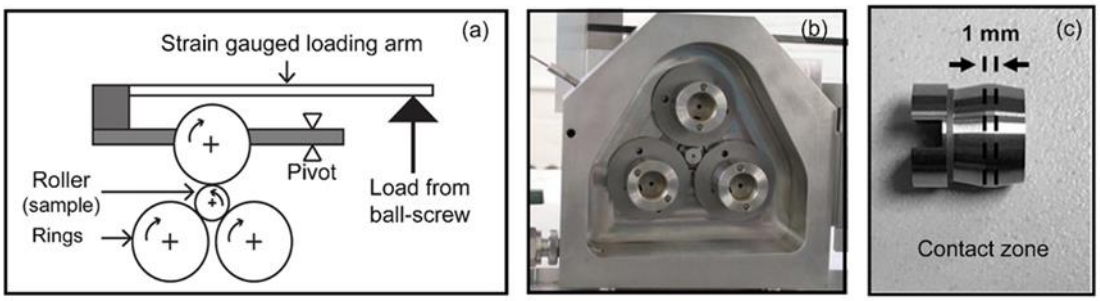

Figure 5.1: (a) Schematic diagram of micropitting test rig (MPR); (b) Experimental setup of roller and rings inside MPR chamber; (c) Image of the roller (test sample) showing the contact zone

All tests were conducted using the conditions listed in Table 5.2. Tests were conducted with maximum Hertzian contact pressure level of 1.5 GPa. The lubricating oil used in this study an API group II base oil with ZDDP anti-wear and other additives, one of which was a viscosity index (VI) improver. Hence the lubricating oil was sheared before testing by running it through piston pump for 48 hours to ensure no change in viscosity occurred due to shearing during rolling contact fatigue tests. The kinematic viscosity of the sheared oil was 0.5051–0.5144 cm^2/s at 40 °C and 0.0756–0.0781 cm^2/s at 100 °C.

Table 5.2: Operating test conditions

Test parameter	
Entrainment velocity (m/sec)	1.75
Slide to roll ratio (%)	20
Normal Load (N)	311
Maximum Hertzian contact pressure (GPa)	1.5
Lubricant sump temperature (°C)	80
Oil film thickness (nm)[a]	80
Lambda ratio	0.16

[a] Estimated using Eq. (5.3)

Minimum oil film thickness (H_{min}) for the experiments was calculated using the Pan-Hamrock's equation mentioned below,

$$H_{min} = 1.714\, U^{0.694} G^{0.568} W^{-0.128} \tag{5.3}$$

where, U is dimensionless speed parameter, G is the dimensionless material parameter, and W is the dimensionless load parameter. The film thickness ratio (λ) was calculated using H_{min} and measured initial composite roughness (Rq) to verify tests were run under boundary lubrication.

An accelerometer attached to the instrument provides peak to peak (P/P) and center-line-average (CLA) values of vibration due to crack propagation and surface deformation during RCF tests. All experiments were run up to 50 million contact cycles or till the system detected a P/P accelerometer signal of 10g, whichever occurred first. Each experiment was associated with a 2-min 'ramp-up' step where the test parameters were ramped to preset conditions (as mentioned in Table 5.2) for the upcoming fatigue step.

5.4.2 Micropitting quantization and characterization

The RCF tests were interrupted periodically to obtain topographical data for roughness analysis and to quantify the amount of micropitting on the rollers. Depending on the RCF life of the samples, data was obtained after 0.01, 0.1, 1, 2.5, 5, 10, 12.5, 15, 20, 25, 32.5, 40 and 50 million cycles. Most of the studies conducted previously on micropitting utilize microscopic imaging to provide a qualitative evaluation of surface damage [2, 8, 24-26]. In this study, we attempted to capture evolution of micropitting quantitively using a novel technique based on data collected using white light non-contact profilometry. A Zygo NewView 7100 microscope with a white light interferometer was used to obtain topographical data from six different locations around the roller circumference (approximately 60° apart) as shown in Figure 5.2. Images from those six locations were post-processed using the texture analysis software to detect micropitted regions. In this study, a surface region with depth greater than 1 μm and an area above 25 μm^2 was considered to be a micropit. Subsequently, the total micropitted area was calculated by accumulating data from the six circumferential locations.

For each location, Ra, $R_{RMS,}$ R_{sk} (skewness) and R_{ku} (kurtosis) values were captured from a scan size of 1×0.6 mm^2 area. Surface scan data were collected and exported into MATLAB as an MxN matrix of height values to calculate spatial parameters. Calculation of the X (transverse direction) and Y (circumferential direction) correlation length was performed by selecting the center (m, n) of the matrix and calculating the 1D autocorrelation function along the m^{th} row and n^{th} column, respectively. The autocorrelation is defined as follows:

$$r_k = \frac{c_k}{c_0} \tag{5.4}$$

where

$$c_k = \frac{1}{T-1}\sum_{t=1}^{T-k}(y_t - \bar{y})(y_{t+k} - \bar{y}) \tag{5.5}$$

The surface autocorrelation map was calculated using the 2D autocorrelation function using the same center point as with the 1D calculation. Subsequently, it was plotted with all values greater than the threshold (1/e) highlighted.

In addition, an FEI Quanta-250 Scanning Electron Microscope (FESEM) was used to obtain high resolution images of micropits using Back Scattered Electron topography mode with an excitation voltage of 10 kV.

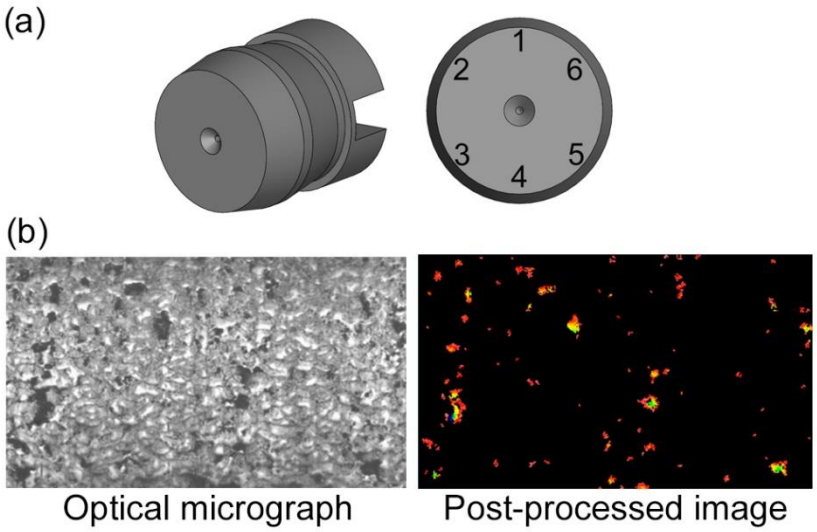

Figure 5.2: (a) Surface images were obtained at six locations around the sample circumference (b) Optical micrographs were converted to quantized maps of micropitted regions

5.5 Results & discussions

5.5.1 Evolution of sample surface during RCF life

Samples with three different levels of RA exhibited very distinct RCF life as shown in Table 5.3. Increasing RA helped to enhance the RCF life of test samples. 15% RA provided an enhancement of about 5 times compared to the 0% RA sample. 70% RA exhibited about 12 times the life compared to 0% RA.

Table 5.3: Rolling contact fatigue life (P/P accelerometer to reach 10g)

Sample		RCF life
70% RA	Test 01	> 50 million
	Test 02	> 50 million
15% RA	Test 01	15 million
	Test 02	17.5 million
0% RA	Test 01	4 million
	Test 02	2.5 million

Figure 5.3 shows the surface evolution for the samples during rolling contact fatigue tests. The 0% RA sample developed transverse directional cracks within the first 10^4 cycles. These cracks continued to grow in size and number as the test progressed. This resulted in a notable increase in accelerometer signal which reached the trip limit of 10g after 4 million cycles, stopping the tests. Thus the 0% RA sample failed before initiation of micropitting due to early crack initiation and rapid crack propagation.

Figure 5.4 shows the amount of micropitting as a percentage of the contact area after 5 million cycles for 15% and 70% RA samples. This quantitative data together with the images in Figure 5.3 provide a better understanding of the evolution of micropitting. In the case of the 15% RA sample, significant amount of micropitting was observed after 5

million cycles. The number and size of micropits increased rapidly between 5-15 million cycles. This resulted in a significant increase in the accelerometer signal, which reached the trip condition (10g) after 15 million cycles.

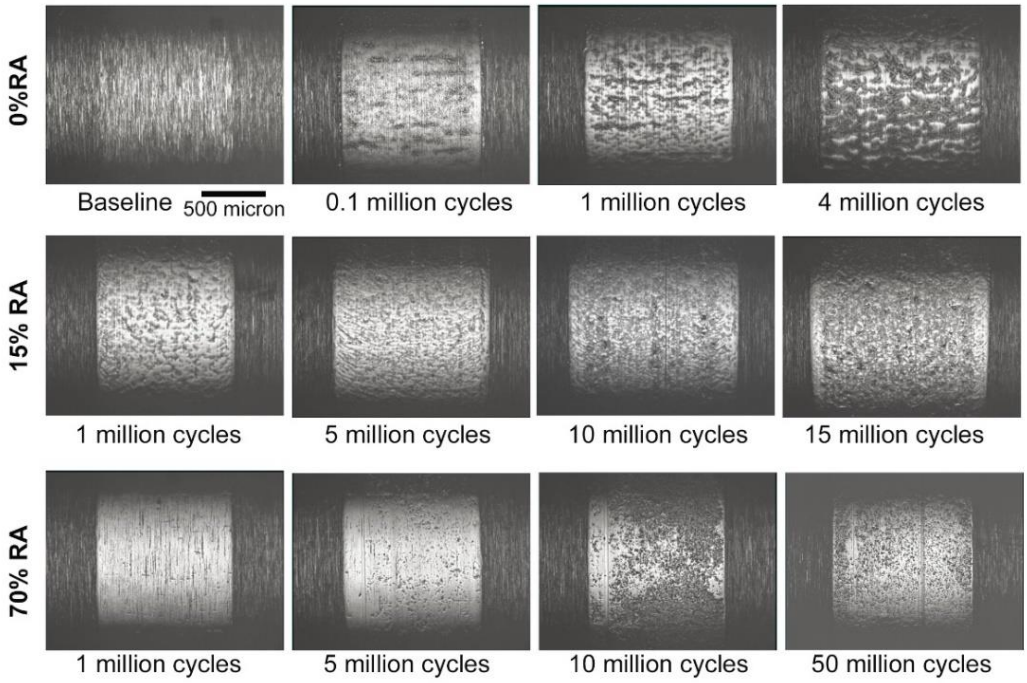

Figure 5.3: Optical micrographs showing surface evolution on roller samples

In the case of the 70% RA sample, pitting was observed initially between 2.5-5 million cycles. Between 5-10 million cycles, the pitting became more significant. For this sample, the number of pits were higher but of smaller size compared to the 15% RA sample. After 10 million cycles, the pits appeared to stabilize. The accelerometer signal also did not reach the trip limit even after 50 million cycles. The stabilization in pit formation and growth is due to the greater RA content in microstructure, which helps to hinder crack initiation and propagation [19, 27]. Consequently, the micropits did not propagate significantly. But after

about 32.5 million cycles, increased wear resulted in a decrease in pit depth and size, resulting in decreased micropitted area.

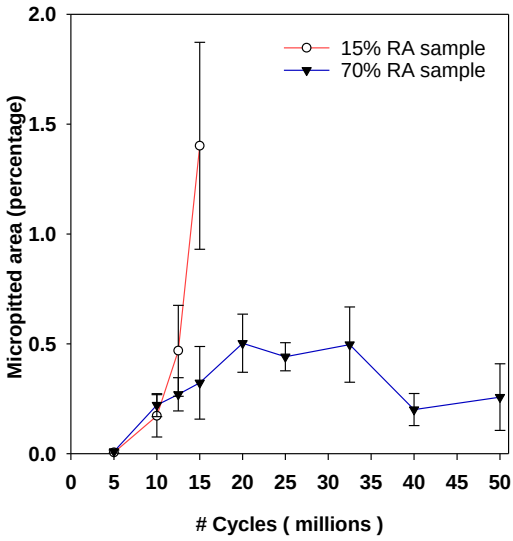

Figure 5.4: Progression of micropitting on 15% and 70% RA samples. Error bars represent 90% confidence intervals

Micropits were characterized in terms of depth and surface area to get better understanding on change of surface roughness parameters. Figure 5.5 shows representative depth and area information of the micropits after 15 million cycles in the form of histograms, based on data from all six locations around the roller circumference to provide a relatively comprehensive snapshot of the contact surface. It can be observed that pit depth and area for 15% RA sample were significantly larger than those of 70% RA sample. This resulted in increased overall micropitted area for 15% RA sample as showed in Figure 5.4.

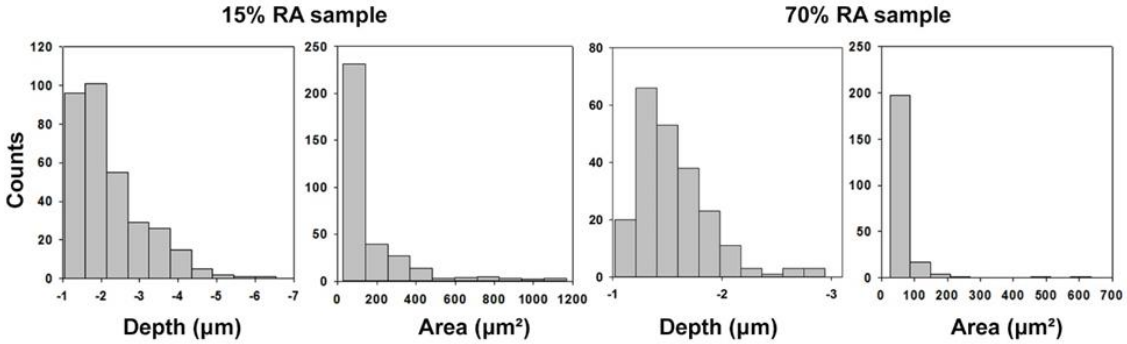

Figure 5.5: Micropits depth and area histogram after 15 million cycles for 15% RA and 70% RA samples

5.5.2 SEM imaging of micropitted surfaces

Figure 5.6 shows the back scattered electron topographical images of failed sample surface. Large number of small size micropits can be observed for 70% RA sample. The 15% RA sample surface was covered with larger micropits. This is consistent with the micropitted area data in Figure 5.4 where the 15% RA sample showed more micropitted area compared to 70% RA sample. In case of 0% RA sample, transverse directional cracks were observed throughout the contact zone. Some delaminated regions were observed due to coalescence of multiple cracks.

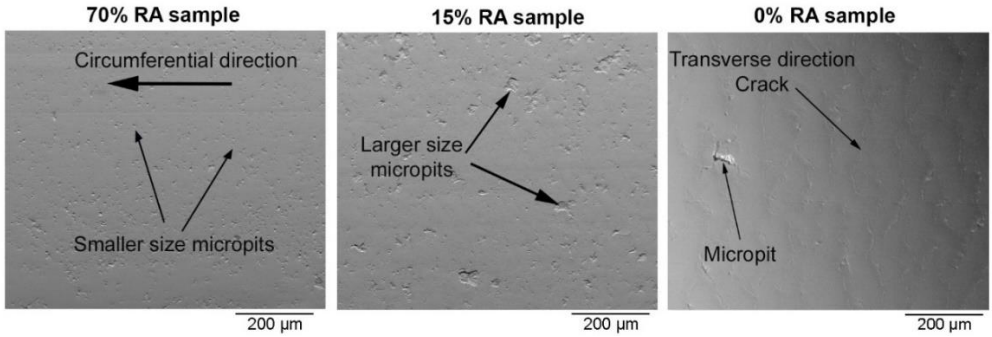

Figure 5.6: BSE topographical images of roller surface at the end of RCF life

5.5.3 Evolution of surface roughness parameters

Figure 5.7 shows the evolution of Ra and R_{RMS} and X-autocorrelation length for the first one million cycles of the RCF tests. Within the first 0.01 million cycles, both Ra and R_{RMS} values dropped to around 50 percent of their baseline values signifying a typical 'run-in' phase [23, 28, 29]. After this period, there was no significant change in both surface roughness parameters up to 1 million cycles for all samples. This observation is consistent with previous findings made by Jenson et al. [23] where significant decrease in surface roughness and work hardening were observed in the order of 10^4 cycles for tests under boundary lubrication. During this run-in time period, the tip of asperities in both tribological bodies deform plastically until the increased bearing area becomes sufficient to bear the applied load.

There is an inverse relationship between the RMS roughness and the correlation length during the run-in period. Initially, the correlation length is quite short due to high asperities on the randomized surface generated after surface grinding and polishing. However, the asperities are quickly worn away within the first ten thousand cycles creating a smoother surface and subsequently diminishing surface variation. As a result, for each case, the correlation length rapidly increases until it stabilizes around 10^4 cycles as observed in Figure 5.7.

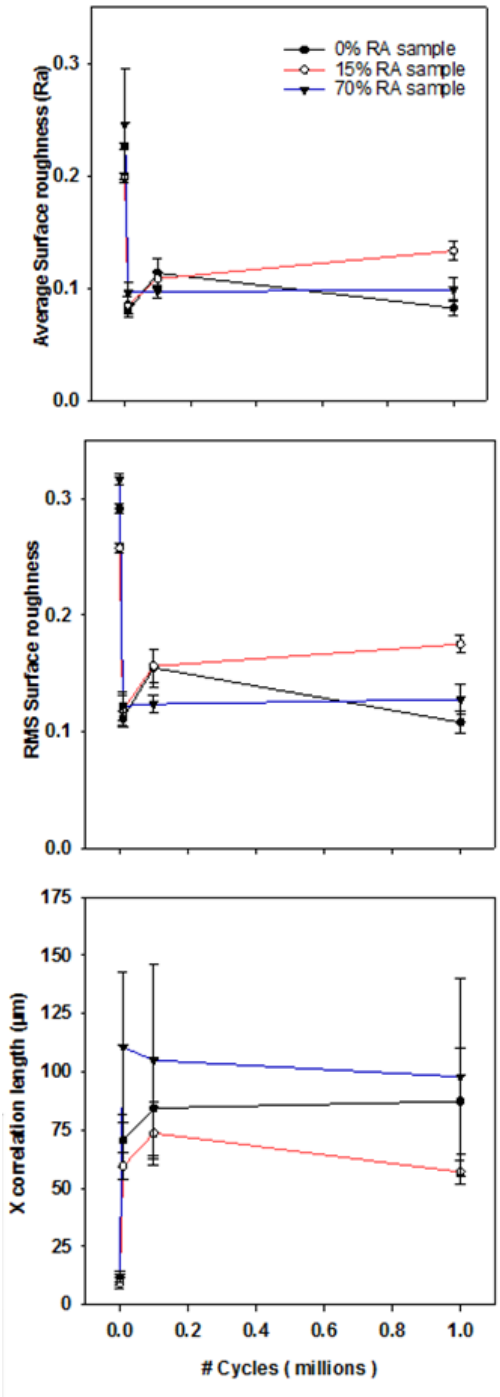

Figure 5.7: Evolution of surface roughness parameters during the first 1 million cycles. Amplitude parameters Ra and R_{RMS} and spatial parameter correlation length shown. Error bars represent 90% confidence intervals

Figure 5.8 shows the evolution of Ra and R_{RMS} for all three roller samples for their entire test duration beyond 1 million cycles. For the 0% RA sample, both roughness parameters

increased significantly between 1 to 2.5 million cycles due to transverse direction crack initiation and propagation. It has been observed that RA helps significantly to hinder crack initiation and propagation [1, 19]. Due to almost no RA for 0% RA samples, crack initiation and propagation rate was significant. This resulted in removal of material from cracked surface and eventually welding of removed material of nearby area of cracked surface. This crack formation, material removal and material welding to nearby surface resulted significant increase in Ra and R_{RMS} value for 0% RA samples.

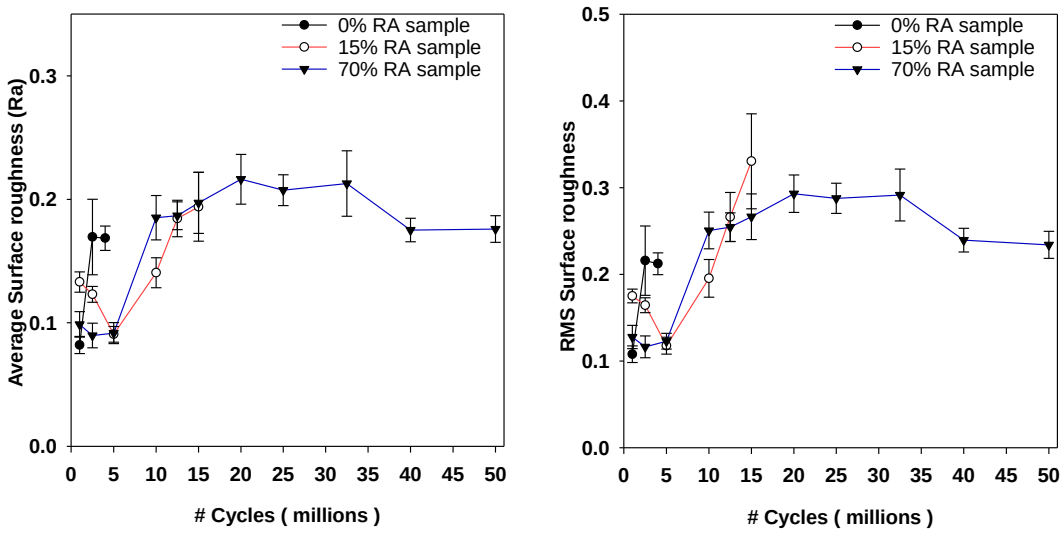

Figure 5.8: Ra and R_{RMS} evolution after run-in period. Error bars represent 90% confidence intervals

Figure 5.8 shows that for the 15% and 70% RA samples, the roughness values didn't change significantly between 1 and 5 million cycles. After 5 million cycles, both Ra and R_{RMS} had increased significantly. If we compare this trend with that of micropitted area for both the samples (Fig. 4), micropitting initiated and significantly propagated over the surface between 5 to 10 million cycles. For 15% RA sample, Ra and R_{RMS} increased constantly from 5 to 15 million cycles due to propagation of micropitting as observed in

Figure 5.4. In the case of 70% RA sample, Ra and R_{RMS} significantly increased between 5 to 10 million cycles after which the values stabilized. This is consistent with the micropitted area calculation as observed in Fig 4. This shows there is a significant correlation between these roughness parameters and propagation of micropitting. After a certain number of cycles (in this case 32.5 million cycles), mild wear from the surface might occurred but since there was no significant propagation of micropits, the micropitted area decreased. As a result, both Ra and R_{RMS} also showed a decreasing trend between 32.5 to 50 million cycles.

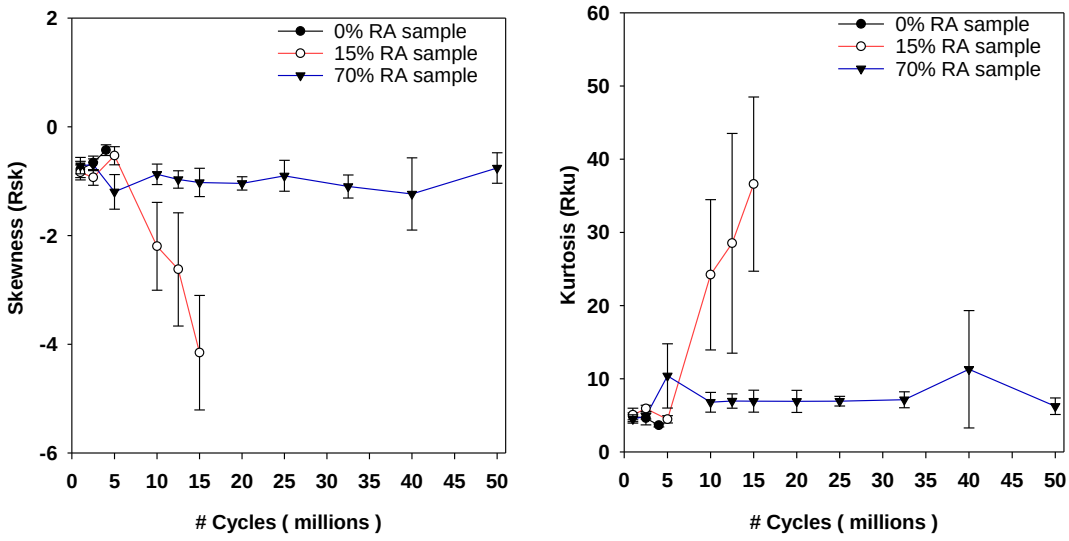

Figure 5.9: Evolution of R_{sk} (skewness) and R_{ku} (kurtosis) after run-in. Error bars represent 90% confidence intervals

Figure 5.9 shows the evolution of skewness and kurtosis for all three samples after 1 million cycles till failure. In the case of the 0% RA sample which failed due to early crack initiation and propagation rather than micropitting, both skewness and kurtosis remain relatively unchanged. In the case of the 15% RA sample, significant micropitting started

after 5 million cycles and propagated significantly between 5-15 million cycles. The decreasing trend of skewness tracked the initiation and propagation of micropits effectively. The kurtosis data showed increase in kurtosis value with propagation of micropitting. For the 70% RA sample, significant pitting was first observed after 2.5 million cycles. This resulted in a slight decrease in the skewness value. Overall, there was no significant change in skewness since the pits didn't propagate significantly. The data shows that skewness and kurtosis data can be used to track initiation and propagation of micropitting.

The evolution of the correlation length along the X axis (transverse direction) after run-in is shown in Figure 5.10. An inverse relationship can be found between the propagation of micropitting and the correlation length. This observation can be reasoned by the degree of randomness with which the micropits develop. For the 15 and 70% RA cases, the micropits are generated quite randomly and as a result, an increase in surface variation results in a shorter correlation length and vice versa. However, for the 0% RA sample, pitting was not observed. As a result, the correlation length didn't decrease with increasing number of cycles. In this case, the cracks in the transverse direction are readily noticeable. These cracks created channels by coalescing with each other with increasing number of cycles. This subsequently increased the correlation length in the transverse direction. This is more evident when examining the AACF of the 0% RA sample in Figure 5.11.

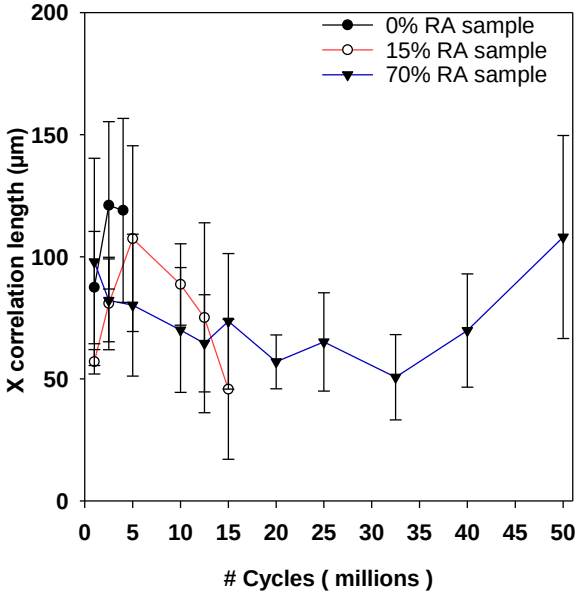

Figure 5.10: Evolution of the correlation length along the X axis after run-in. Error bars represent 90% confidence intervals

In Figure 5.11, a 2D analysis based on autocorrelation length is presented to observe crack initiation and propagation in axial or transverse direction for 0% RA sample. As expected with a ground surface, the baseline case shows rapid decay in the axial direction against the lay pattern followed by random fluctuation. As formation of cracks starts, a periodicity can be observed in the X direction in which frequency increases as more cracks coalesce. This continues until most of the surface becomes covered with cracks, and ultimately by 4 million cycles, the surface cracks are nearly random with little periodicity perceptible. This is more evident by observing the lack of eccentricity in the correlation length with respect to surface orientation. That is, the surface became isotropic with the propagation of cracks towards failure.

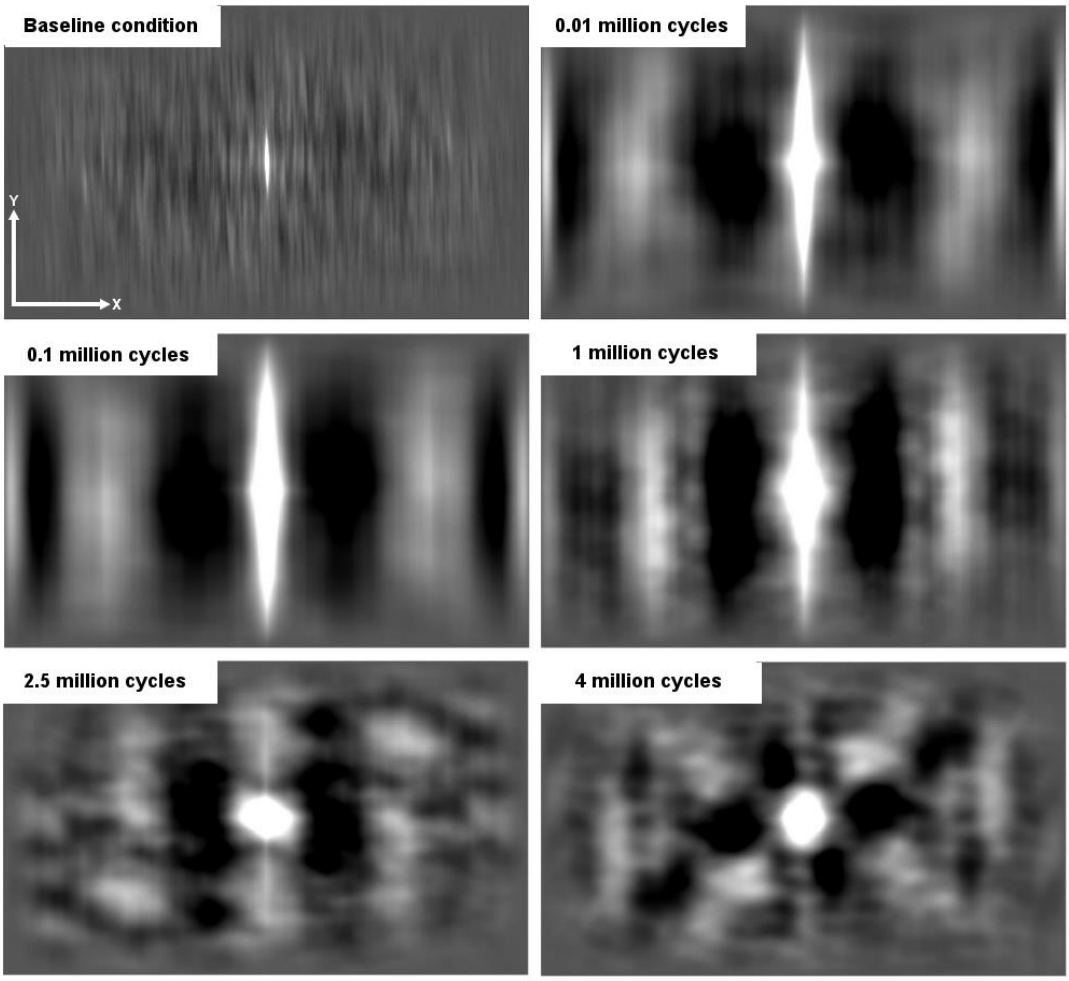

Figure 5.11: Aerial autocorrelation function (AACF) of the 0% RA Sample

5.6 Conclusions

- Four different amplitude roughness parameters and a spatial parameter were studied to investigate correlation between micropitting initiation and propagation and surface roughness parameter evolution during rolling contact fatigue test of carburized AISI 8620 steel.
- Run-in occurred within the first 10^4 cycles of RCF tests for all samples, during which the Ra and R_{RMS} values dropped to around 50% of their initial value due to plastic deformation of asperity tips.

- After run-in, 0% RA samples failed very quickly due to early crack initiation and rapid crack propagation. These cracks developed a channel-like formation in transverse direction, which caused a consistent increase in the correlation length until the surface became fully covered with cracks and resulted a nearly random surface in the axial direction.
- An inverse relationship exists between RMS roughness and correlation length. Similarly, this trend continued after run-in for the 15 and 70% RA cases. The propagation of micropitting and correlation length also showed an inverse relationship in those samples. Skewness and kurtosis were found to be reliable indicators to detect initiation and propagation of micropitting.

The observed correlation between surface roughness parameter evolution and micropitting can be used to monitor and effectively predict the long-term performance of components subject to rolling contact fatigue under boundary lubrication regime.

5.7 Acknowledgements

Partial funding for this work was provided by John Deere Product Engineering Center in Waterloo, Iowa and Iowa State University. The authors would like to thank Anvay Pradhan for his assistance in surface topography data postprocessing and calculations.

5.8 References

1. Sadeghi, F., et al., *A Review of Rolling Contact Fatigue.* Journal of Tribology-Transactions of the Asme, 2009. **131**(4).

2. Mahmoudi, B., et al., *Influence of a WC/a-C:H Coating on Micropitting Wear of Bearing Steel.* Tribology & Lubrication Technology, 2015. **71**(4): p. 24-27.

3. Rycerz, P., A. Olver, and A. Kadiric, *Propagation of surface initiated rolling contact fatigue cracks in bearing steel.* International Journal of Fatigue, 2017. **97**: p. 29-38.

4. Bakoglidis, K.D., et al., *Rolling performance of carbon nitride-coated bearing components in different lubrication regimes.* Tribology International, 2017. **114**: p. 141-151.

5. Soltanahmadi, S., et al., *Investigation of the effect of a diamine-based friction modifier on micropitting and the properties of tribofilms in rolling-sliding contacts.* Journal of Physics D-Applied Physics, 2016. **49**(50).

6. Moallem, H., S. Akbarzadeh, and A. Ariaei, *Prediction of micropitting life in spur gears operating under mixed-lubrication regime using load-sharing concept.* Proceedings of the Institution of Mechanical Engineers Part J-Journal of Engineering Tribology, 2016. **230**(5): p. 591-599.

7. Wei, J., A.Q. Zhang, and P. Gao, *A study of spur gear pitting under EHL conditions: Theoretical analysis and experiments.* Tribology International, 2016. **94**: p. 146-154.

8. Soltanahmadi, S., et al., *Tribochemical study of micropitting in tribocorrosive lubricated contacts: The influence of water and relative humidity.* Tribology International, 2017. **107**: p. 184-198.

9. Evans, R.D., et al., *Influence of Steel Type on the Propensity for Tribochemical Wear in Boundary Lubrication with a Wind Turbine Gear Oil.* Tribology Letters, 2010. **38**(1): p. 25-32.

10. Ghribi, D., C. Peyrac, and M. Octrue, *Shot peening of gear tooth flanks: Search for an optimal surface topography against the micropitting.* International Conference on Gears 2017/ International Conference on Gear Production/ International Conference on High Performance Plastic Gears 2017, Vols 1 and 2, 2017. **2294**(1-2): p. 153-162.

11. Blake, G. and J. Reynolds, *Case Study Involving Surface Durability and Improved Surface Finish*, in *Gear Technology*. 2012. p. 66-75.

12. Bell, M., G. Sroka, and R. Benson *The Effect of the Surface Roughness Profile on Micropitting*. 2013. 47-53.

13. Predki, W., K. Nazifi, and G. Lutzig, *Micropitting of Big Gearboxes: Influence of Flank Modification and Surface Roughness*, in *Gear Technology*. 2011. p. 42-46.

14. Clarke, A., et al., *Running-in and micropitting behaviour of steel surfaces under mixed lubrication conditions.* Tribology International, 2016. **101**: p. 59-68.

15. Conwayjones, J.M. and D.R. Eastham, *Parameters for Control of Roughness of Surfaces Operating with Thin Oil Films.* International Journal of Machine Tools & Manufacture, 1995. **35**(2): p. 253-257.

16. Bhusan, B., *Surface Roughness Analysis and Measurement Techniques*, in *Modern Tribology Handbook*. 2001, CRC Press. p. 49-114.

17. *Characterisation of Areal Surface Texture*. 2013: Springer, Berlin, Heidelberg.

18. Dong, W.P., P.J. Sullivan, and K.J. Stout, *Comprehensive study of parameters for characterising three- dimensional surface topography.* Wear, 1994. **178**(1-2): p. 29-43.

19. Roy, S. and S. Sundararajan, *The effect of heat treatment routes on the retained austenite and Tribomechanical properties of carburized AISI 8620 steel.* Surface & Coatings Technology, 2016. **308**: p. 236-243.

20. Roy, S., et al., *Effect of laser treatment parameters on surface modification and tribological behavior of AISI 8620 steel.* Tribology International, 2017. **112**: p. 94-102.

21. Kim, H.J. and Y.G. Kweon, *The effects of retained austenite on dry sliding wear behavior of carburized steels.* Wear, 1996. **193**(1): p. 8-15.

22. Verhoeven, J.D., *Steel Metallurgy for the Non-Metallurgist*. 2007: ASM International.

23. Jenson, A.D., S. Roy, and S. Sundararajan, *The evolution of hardness and tribofilm growth during running-in of case carburized steel under boundary lubrication.* Tribology International, 2018. **118**: p. 1-10.

24. Laine, E., et al., *The Effect of a Friction Modifier Additive on Micropitting.* Tribology Transactions, 2009. **52**(4): p. 526-533.

25. Singh, H., et al., *Fatigue resistant carbon coatings for rolling/sliding contacts.* Tribology International, 2016. **98**: p. 172-178.

26. Al-Tubi, I.S., et al., *Experimental and analytical study of gear micropitting initiation and propagation under varying loading conditions.* Wear, 2015. **328**: p. 8-16.

27. Shen, Y., et al., *Effect of retained austenite - Compressive residual stresses on rolling contact fatigue life of carburized AISI 8620 steel.* International Journal of Fatigue, 2015. **75**: p. 135-144.

28. Wagner, J.J., A.D. Jenson, and S. Sundararajan, *The effect of contact pressure and surface texture on running-in behavior of case carburized steel under boundary lubrication.* Wear, 2017. **376**: p. 851-857.

29. Clarke, A., H.P. Evans, and R.W. Snidle, *Understanding micropitting in gears.* Proceedings of the Institution of Mechanical Engineers Part C-Journal of Mechanical Engineering Science, 2016. **230**(7-8): p. 1276-1289.

CHAPTER 6. EFFECT OF RETAINED AUSTENITE ON SPALLING BEHAVIOR OF CARBURIZED AISI 8620 STEEL UNDER BOUNDARY LUBRICATION

Modified from a paper to be submitted in *International Journal of Fatigue*

Sougata Roy and Sriram Sundararajan

6.1 Abstract

The objective of this study is to investigate the effect of retained austenite (RA) on the macropitting or spalling behavior of carburized AISI 8620 steel under boundary lubrication condition. Samples with RA ranging from approximately 0 to 70% were prepared using specific carburizing schemes. Macropitting tests were carried out at maximum contact pressure 1.9 GPa using a benchtop test rig. Samples were subsequently analyzed using noncontact white light profilometry and micro X-Ray Diffraction to observe the evolution of contact surface and RA respectively. Results indicated that increasing RA and minimizing pre-existing sub-surface cracks in the material help to enhance macropitting life. The failure mechanism for all samples was from spall formation due to sub-surface crack initiation and propagation with clear evidence of RA transforming to martensite. Pre- and post-experiment residual stress showed the impact of phase transformation on enhancement of residual stress during RCF experiments, however residual stress was not a significant factor in impacting the life.

6.2 Introduction

Rolling contact fatigue (RCF) is a typical failure mode observed in drivetrain components which are loaded by repeated high Hertzian contact pressure such as gears and bearings.

Depending on operating conditions different types of RCF failure modes can be observed in those components. During RCF tests these failure modes compete to each other and based on operating conditions, a specific one becomes dominant resulting failure of that component. Abrasive wear, scuffing and pitting are the main failure modes observed in gears [1]. Abrasive wear takes place where hard, foreign particles such as metal grit or metallic oxides penetrate the metal surface and adhere temporarily causing the damage. Scuffing failure occurs due to extreme conditions of adhesive wear. In this case, the oil film is rolled away ahead of the contact due to extreme heat generation in the contact region. Pitting can be divided into two groups, micro and macropitting or spalling. Both failure modes are observed due to rolling-sliding contact motion between two mating contacts. It is very clear that abrasive wear and scuffing can be controlled by avoiding contamination of lubricant or by modifying the test parameters to control the lubricating oil temperature but pitting is purely a contact fatigue phenomenon. Consequently, lots of studies are being conducted recently to observe the pitting phenomena from both lubrication, materials and operating condition viewpoints.

Much research has been aimed at alleviating rolling contact fatigue by modifying material properties including amount of retained austenite [2], residual stress [3] and employing different heat treatment techniques [4] and coatings [5]. In case of retained austenite, Rivero and Rudd observed higher initial RA on bearing balls can lower their service life [6]. On the other hand, Dommarco et al. showed superior rolling contact fatigue life for samples with increased RA [2]. These contradictory results suggest that the role of RA on RCF needs further detailed investigation. Secondly, most of the recent studies focus on the effect of different surface coatings [5, 7] and lubricants [8-11] on

micropitting, but there is comparatively a dearth of literature that addresses the microstructural implications on macropitting or spalling.

It must be noted that there still exists an ambiguity over the term spalling and pitting [12]. In some literatures spalling and pitting are used indiscriminately whereas in some they have been differentiated based on severity of surface damage [13]. Generally, pitting appears as shallow craters at contact surfaces with maximum depth of 10 μm. Spalling appears as deeper cavities typically 20-100 μm at contact surface [14]. One of the main reasons behind the obscurity of the terms is the continued debate on the physical causes of pitting and spalling. Xu and Sadeghi mentioned when debris pass through a contact region, they generate dents on rolling surface [15]. These work as stress raisers to initiate microcracks which will grow into spalls leading to failure of the machine component. Contact fatigue models have been developed based on this theory that spalling is a result of surface crack initiation and propagation [16-18]. Way's hypothesis postulates that spalling formation is driven by entrapment of lubricating oil under surface cracks [19]. But experiments conducted by Cheng et. al showed that surface cracks are generally in the range of 5-10 μm and it is impossible to form a large spall cavity unless there is near surface inclusion [20]. Ding described spalling as a sub-surface initiated failure mode [12]. Ding's definition has been well received by some recent studies conducted on spalling [21-23].

The objective of this study is to investigate the effect of different levels of retained austenite (RA) on the macropitting or spalling behavior of carburized AISI 8620 steel under boundary lubrication condition similar to those observed in gearboxes of wind turbines, agricultural machineries and earth moving equipment. AISI 8620 steel samples

were subjected to different carburizing and tempering techniques to achieve a wide range of retained austenite levels in the samples. Initially, experimental test conditions were finalized to replicate spalling as the dominant failure mode on test samples prior to conducting the study described here.

6.3 Materials

Experiments were conducted on AISI 8620 steel which is widely used in drive train components. Heat treatment schemes can be utilized to vary RA levels on steel samples [24-26]. In this study, RA was varied using different carbon potential (1.2-2%) during carburizing and by varying the tempering schemes. The tempering temperature and time were varied from 50°C for 1 hour to 400°C for 2 hours. All samples were oil quenched at 40°C for 1 hr. between carburizing and tempering steps. Subsequently, the samples were ground and polished to achieve average surface roughness level 0.22±0.2 μm over a scan size of 1 mm × 0.6 mm.

6.4 Methods

6.4.1 Retained austenite and residual stress measurement

X-ray diffraction was used to measure retained austenite and residual stress of the samples. To capture phase transformation during our RCF tests using X-ray diffraction (XRD), it was necessary to collect the data from within the 1 mm wide contact zone (see Figure 6.1c). A Rigaku SmartLab XRD with micro-XRD, X-Y mapping stage and hybrid pixel array detector was used to collect data from 500-micron area on the face-width of sample. A Cu Kα target was used (wavelength 1.54 Å) with a target voltage of 40 KV and current 44 mA. XRD scan data was collected for a range of 40 to 90 degrees (2θ angle). The data was later analyzed using TOPAS software to determine the amount of

RA in those samples similar to previous studies [24, 25]. Average RA percentage was calculated based on four measurements on each type of samples. The residual stress levels were measured using Cr XRD (wavelength 2.29 Å) with a target voltage of 35KV and current of 1.5 mA. For these measurements, the (211)-peak of Cr Kα radiation was used to determine the peak positions that were used for residual stress determination. The residual stress was calculated based peak positions measured in 16 different tilt angles (psi) between 0-45° (each 3° apart).

Table 6.1: RA and residual stress levels on carburized samples

Heat treatment scheme	RA level	RA%	Residual stress (MPa)
2% C potential carburizing with tempering at 50°C for 1 hr.	'High RA'	69.7±3.7	153.2±49.3
1.2% C potential carburizing with tempering at 190°C for 1.5 hrs.	'Medium RA'	14.5±1.9	251±42.9
1.2%C potential carburizing with tempering at 400°C for 2hrs	'Low RA'	0.4±0.2	493.3±11.3

RA and residual stress on the samples prepared by three different heat treatment schemes are mentioned in Table 6.1. For further discussion, these three levels of RA are approximately mentioned as 70%, 15% and 0% RA and/or as high, medium and low levels of RA. Increasing carbon potential suppresses martensite start (M_s) and martensite finish (M_f) temperature [26]. This results in incomplete conversion of austenite to martensite and helps to increase retained austenite content on surface. Increasing tempering temperature and time help to convert existing retained austenite to martensite

[27]. Carburizing helped to generate compressive residual stress on all sample surfaces. High temperature tempering resulted phase transformation of austenite to pearlite or bainite. This helps in expansion of surface layer due to volumetric expansion during phase transformation. Consequently, higher compressive residual stresses were observed in lower RA samples.

6.4.2 Rolling contact fatigue test

Rolling contact fatigue tests were performed using a Micro Pitting Rig (MPR) from PCS instruments (London, UK) [28]. A schematic representation of the experimental setup is shown Figure 6.1a. The MPR is a computer controlled disc-on-disc contact instrument in which a central roller (sample) is in contact with three harder counter face rings as shown in Figure 6.1b. The roller therefore experiences three contact cycles per revolution at a constant contact pressure. The speeds of the rings and rollers are controlled independently which allows different combinations of rolling and sliding contact. The MPR utilizes a dip lubrication system, with the oil level 27.8 millimeters below the center of the roller and a sump volume of 150 milliliters. The unit is also temperature controlled to maintain the desired operating temperature of the lubricant sump. A chamfered roller with a 1mm face-width (see Figure 6.1c) was used for the tests performed in this study. The diameter for roller was 12 mm and for rings 54.15 mm. The relative amount of rolling and sliding during testing is determined by the slide-to-roll ratio (SRR) and is defined as follows:

$$\text{SRR}\ (\%) = \frac{U_1 - U_2}{{}^1\!/_2 (U_1 + U_2)} \cdot 100 \qquad (6.1)$$

where U_1 is the speed of the rings and U_2 is the speed of the roller. All tests were conducted using the conditions listed in Table 6.2.

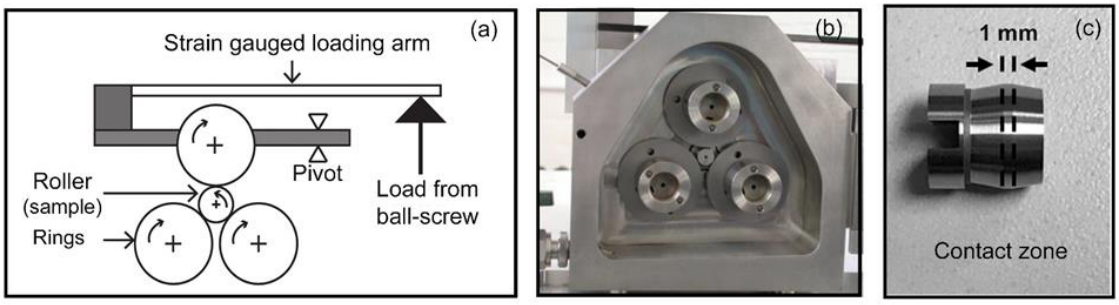

Figure 6.1: a- Schematic diagram of micropitting test rig (MPR); b-Experimental setup of roller and rings inside MPR chamber; c-Representative image of roller (test sample)

Table 6.2: Operating test conditions

Test parameter	
Entrainment velocity (m/sec)	1
Slide to roll ratio (%)	-30
Normal Load (N)	500
Maximum Hertzian contact pressure (GPa)	1.9
Lubricant sump temperature (°C)	80
Oil film thickness (nm)[a]	51
Lambda ratio	0.16

[a] Estimated using Eq. (6.2)

The lubricating oil used in this study was an API group II base oil with ZDDP anti-wear and other additives, one of which was a viscosity index (VI) improver. Hence the lubricating oil was sheared before testing by running it through piston pump for 48 hours to ensure no change in viscosity occurred due to shearing during rolling contact fatigue tests. The kinematic viscosity of the sheared oil was 50.51–51.44cSt at 40 °C and 7.56–7.81cSt at 100 °C.

Minimum oil film thickness (H_{min}) for the experiments was calculated using the Pan-Hamrock equation mentioned below,

$$H_{min} = 1.714\, U^{0.694} G^{0.568} W^{-0.128} \quad (6.2)$$

where, U is dimensionless speed parameter, G is the dimensionless material parameter, and W is the dimensionless load parameter. The film thickness ratio (λ) was calculated using H_{min} and measured initial composite roughness (Rq) to verify tests were run under boundary lubrication.

An accelerometer attached to the instrument provides peak to peak (P/P) and center-line-average (CLA) values of vibration experienced by the roller. Crack propagation and surface deformation during RCF tests lead to increased vibrations. All experiments were run till the system detected a P/P accelerometer signal of 10g. Each experiment was associated with a 2-min time duration 'ramp-up' step where the test parameters were ramped to preset conditions (as mentioned in Table 6.2) for the upcoming fatigue step.

6.4.3 Macropitting quantization and characterization

We attempted to quantify the macropit depth using non-contact profilometry. Interferometry based techniques were unable to capture data from deeper regions of the macropits. A Sensofar 3D optical surface profilometer using focus variation microscopy mode was used to capture the height maps of the macropits at the end of each tests. Along with this, the RCF tests were interrupted periodically (after 0.01, 0.1, 1, 5, 10, 15, 22.5 million cycles based on the RCF life) to analyze the evolution roller samples surface during the tests using a Zygo NewView 7100 white light interferometer.

In addition, an FEI Quanta-250 Scanning Electron Microscope (FESEM) was used to obtain high resolution images of micropits using secondary electron mode with an

excitation voltage of 10 kV. These images help to get size information and topography of fractured surface of the macropits.

6.4.4 Cross sectional microstructure study

Baseline samples and macropitted samples were cross-sectioned for further metallographic analysis.

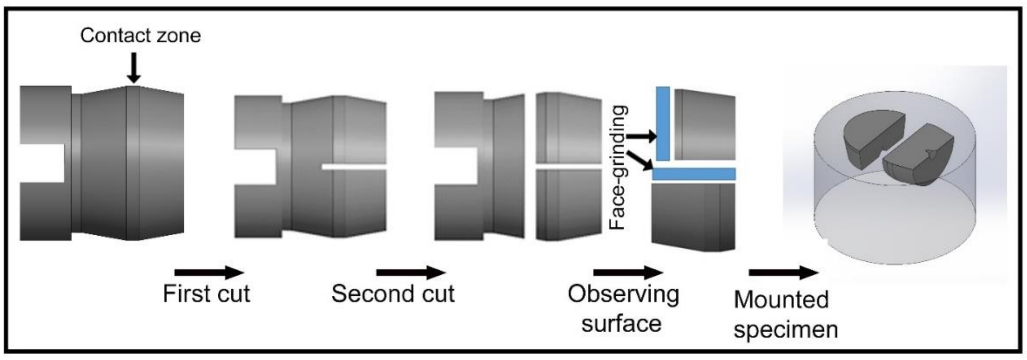

Figure 6.2: Cross-sectioning procedure and mounting of test samples for microstructure study

Figure 6.2 shows the cross-sectional plan to study surface and sub-surface regions of each roller sample. The samples were polished sequentially with 600, 800, 1200 SiC grit papers and subsequently with 3 and 1 μm diamond suspension. In order to reveal the microstructure, the samples were etched with 2.5% nital solution. The microstructure was subsequently observed using a field emission scanning electron microscope.

6.5 Results and discussion

6.5.1 Effect of retained austenite during rolling contact fatigue

Table 6.3 shows the results of the RCF tests. It can be observed that overall the 0% RA samples had lower RCF life compared to 15 and 70% RA samples. The 15% RA sample shows slightly higher life compared to the 70% RA sample.

Table 6.3: Rolling contact fatigue life (P/P accelerometer to reach 10g)

Sample	Test trials	RCF life (million)	Avg. life (mean±CI[b])
70% RA	Test 01	20.4	18±4.8
	Test 02	18.9	
	Test 03	14.7	
15% RA	Test 01	23	21.56±2.2
	Test 02	19.4	
	Test 03	22.3	
	Test 04	22	
0% RA	Test 01	13.4	13.96±3.5
	Test 02	16.3	
	Test 03	12.2.	

[b] CI= 90% Confidence Interval

The results confirm that RA has a beneficial role in enhancing macropitting life under boundary lubrication. Also, the 0% RA samples had maximum initial compressive residual stress but still exhibited the lowest RCF life. This indicates that initial residual stress is less of a factor compared to RA in impacting macropitting life.

Figure 6.3 shows a representative evolution of the P/P accelerometer signal for the different RA samples during RCF testing. In all cases, the RCF life can be divided into two periods N1 and N2. The N1 period shows no significant change in P/P accelerometer signal because the sub-surface crack initiation and propagation cannot affect the vibration amplitude. The N2 period shows a significant and very rapid change in the vibration amplitude due to formation of a spall on the surface. Thus, N2 represents the spall progression period, which is very short compared to N1, with the N2/N1 ratio varying between 0.02-0.07 among these three types of samples. This observation is consistent

with observations made by previous researchers [23] and shows that macropitting or spalling is a catastrophic failure which occurs in a very short time.

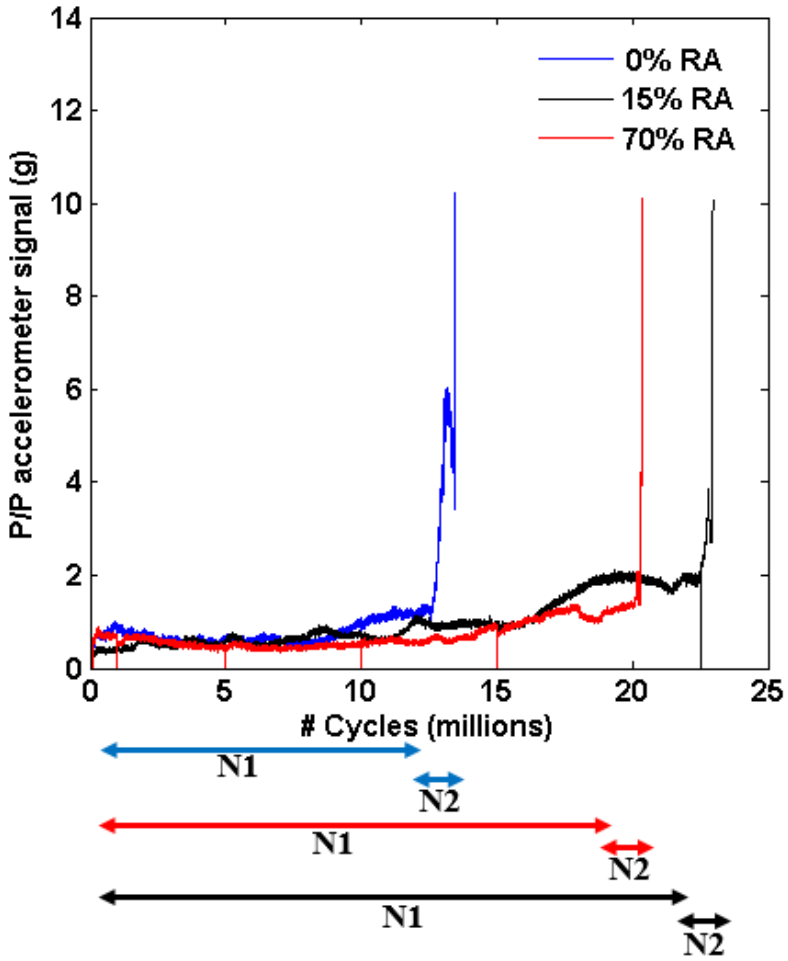

Figure 6.3: P/P accelerometer signal during RCF tests

6.5.2 Morphology of macropitting on different samples

Figure 6.4 shows the evolution of roller surface with number of cycles during RCF test before failure. In all three cases the run-in happened in the initial 0.01 million cycles which resulted in significant drop in sample roughness. Eventually microscale pits appeared on the surface with pit depths of less than a micron and eventually stabilized in

size resulting in a stable accelerometer signal during their RCF life (N1 period) as observed in Figure 6.3.

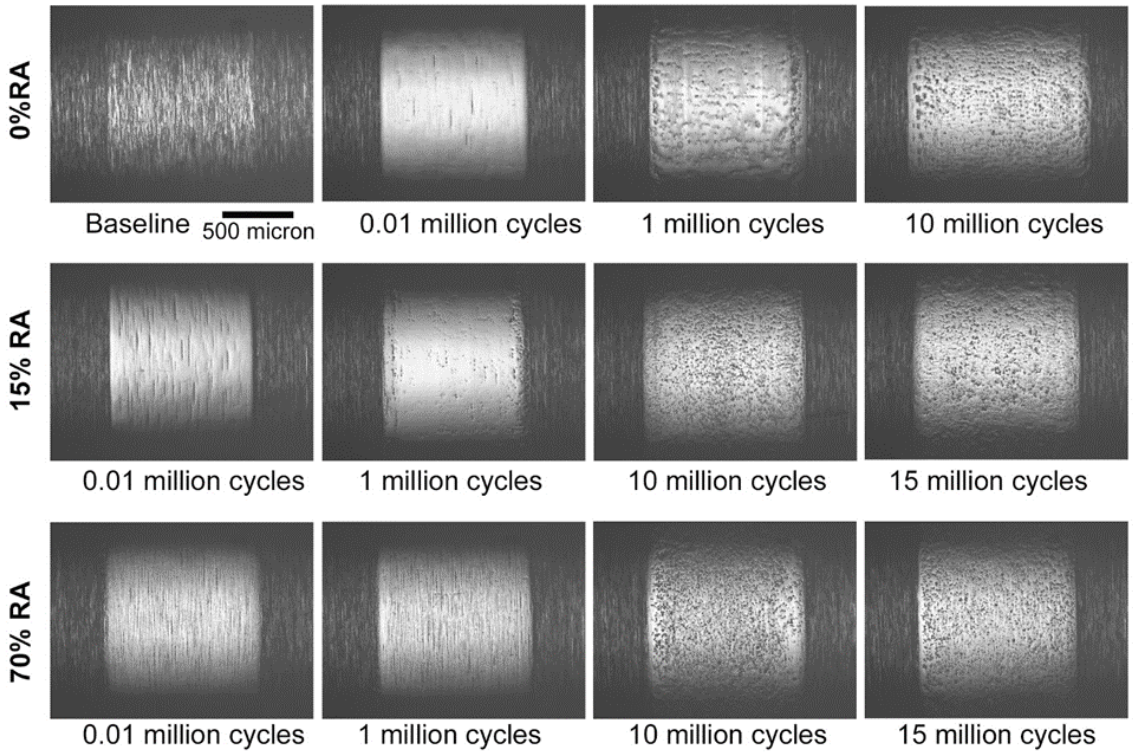

Figure 6.4: Surface evolution during macropitting tests of different RA samples

Figure 6.5 shows the height map and secondary electron images of macropits for the different RA samples. The maximum depth of the macropits observed was within 100-120 μm. Most of the samples failed due to formation of a single big macropit or spall at the center of roller contact surface covering almost the entire contact face width of roller samples. This confirms that these pits did not form due to stress concentration at the edges of contact region. There was no significant trend observed in the size or depth of the pits among samples from different RA levels.

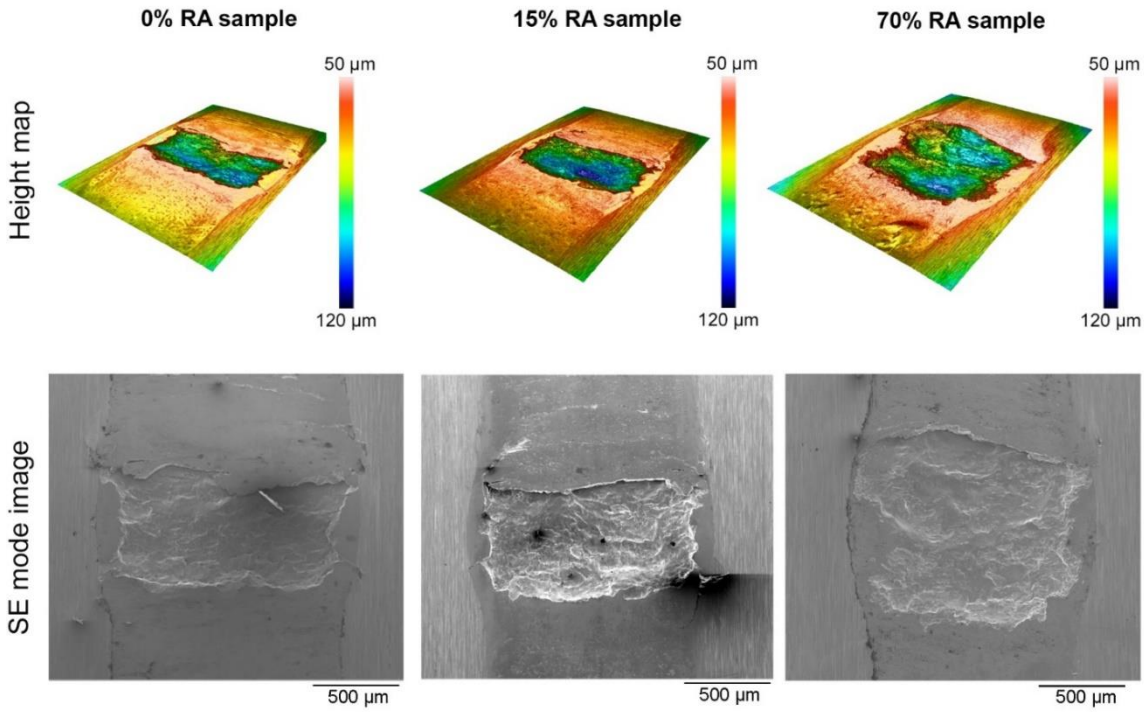

Figure 6.5: Height map and secondary mode images of macropits

In secondary mode, the damaged surface appears white in the fractured zones due to charging of electron in those uneven areas. The fracture plane at the bottom of macropits are quite flat and the external profile edges of the spalled regions are sharp. This is due to catastrophic delamination of spall from the contact surface region at the end of their RCF life.

6.5.3 Phase transformation

Figure 6.6 shows the evolution of RA in 15% and 70% RA samples as a function of contact cycles. The maximum amount of phase transformation happened during first 0.01 million cycles with the 15% RA sample showing almost complete transformation in this time. This is the time period when the tip of asperities on both contacting surfaces deform plastically until the increased bearing area becomes sufficient to bear the applied load.

This is called ‘break-in’ or ‘run-in’ period in gears and bearings [29]. This is consistent with previous observations reported by Dommarco et al. [2].

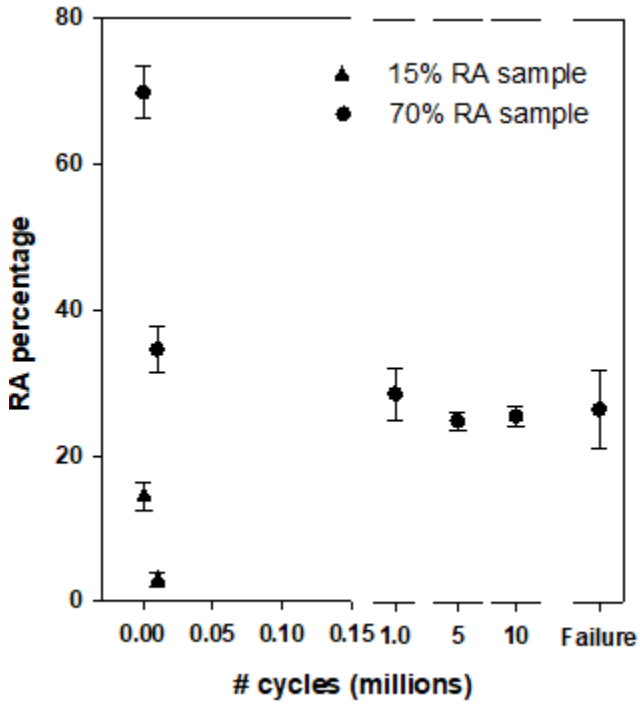

Figure 6.6: Phase transformation during RCF tests for medium and high RA samples

Subsequently, in the case of the 70% RA samples, the RA amount stabilized at about 24% after around 5 million cycles. RA in the microstructure helped improve RCF life in two ways. First, inherent ductility of RA helps to delay crack growth by blunting tips of crack while growing. Second, martensitic phase transformation can generate compressive residual stresses increase in the case depth (described in section 6.5.4), which also contribute to delayed crack growth by promoting crack closure. This is the reason behind observing higher macropitting life for 15% and 70% RA samples compared to 0% RA samples. There is no statistically significant trend observed in terms of 15% and 70% RA samples.

6.5.4 Evolution of residual stress

Figure 6.7 shows the baseline and post experiment residual stress numbers for different RA samples. A significant increase in compressive residual stress is observed for 70% and 15% RA samples.

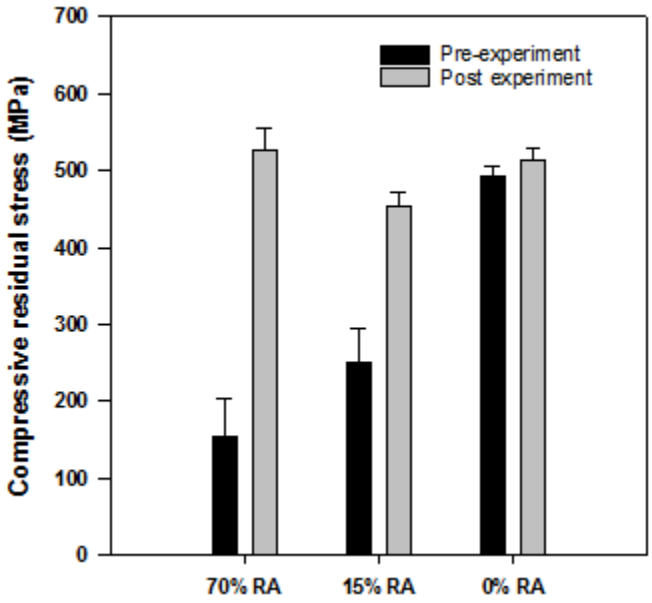

Figure 6.7: Evolution of residual stress during RCF tests for different RA samples

The specific volume of martensite is larger than austenite so during phase transformation, volume expansion results in increase in compressive residual stress for the samples. In case of 70 % RA samples, the amount of phase transformation was more compared to 15% RA samples resulting in larger difference between baseline and post experiment residual stress. However, the final compressive residual stresses do not correlate well with the observed life, suggesting that this attribute is not a strong predictor of macropitting life.

6.5.5 Microstructural observation

The baseline and post experiment microstructure for all three levels of RA samples are depicted in Figure 6.8. Prior to experiments, samples showed blocky islands of RA and needle like martensite zones. MnS based inclusions were also detected in all samples. These inclusions are sometimes added to steel microstructure intentionally to increase machinability of steel [30]. In case of the 0% RA sample, high temperature tempering transformed remaining austenite to martensite. Martensite is formed by shear mechanism where many atoms moves cooperatively and almost simultaneously. It has been previously observed that the high carbon plate martensite is sensitive to micro cracking due to the non-parallel plate formation [31]. The micro cracks are generally formed in the largest martensite plates. Our 0% RA samples exhibited such microcracks in few of the martensite plate regions as shown in Figure 6.8. For the 15% RA sample, no internal cracks were observed. In the case of the 70% RA sample, long internal subsurface cracks were observed in different regions. Due to high carbon potential carburizing for 70% RA samples, carbide precipitation at grain boundary regions occurred. Generally, stress concentration occurs at the sharp or uneven edges of carbide particles and this may result in crack initiation [32]. In our previous study, we observed that higher RA can help to improve RCF life by decreasing crack propagation rate [33]. Higher amounts of RA create more barriers for fatigue crack growth resulting improvement in fatigue life. This can be attributed to the formation of very fine martensite particles in local plasticity in adjacent of crack, which effectively block dislocation motion [34]. It has also been argued that dispersed fine martensite particles retard the propagation of fatigue cracks. In addition, the transformation of retained austenite to martensite during deformation can

relax the stress field and introduce a compressive stress which is also considered to improve fatigue strength. Due to this beneficial effect of RA, higher RA samples (15% and 70% RA samples) showed improved macropitting life compared to 0% RA samples. The baseline microstructure explains the reason behind not observing significant improvement on macropitting life for 70% RA samples compared to 15% RA samples. In the present investigation, initial large subsurface cracks in 70% RA samples had a negative impact on RCF life compared to the 15% RA sample. But if the RCF life of the 70% RA is compared against 0% RA samples, 70% RA samples showed better macropitting life even though they had larger and more sub-surface cracks due to higher RA in microstructure. This strengthens the finding that increasing RA contributes to increased macropitting life.

Post experiment microstructures were captured from regions away from the micropitted zone to observe sub-surface condition in other areas where there was potential to form spall as well. One common observation is, in all three cases the top surface looked very smooth and no surface initiated craters were observed. Also, sub-surface cracks with a depth of 80-100 μm are observed in the circumferential direction of all samples. The depths of spalls observed in Figure 6.5 are of similar range which indicates that spalls occurred due to propagation of these sub-surface cracks to surface. This confirms that spalling is a sub-surface initiated failure mode. The smoother surface of the post experiment samples explains the reason behind observing a relatively stable accelerometer signal during the N1 period of RCF life (Figure 6.3).

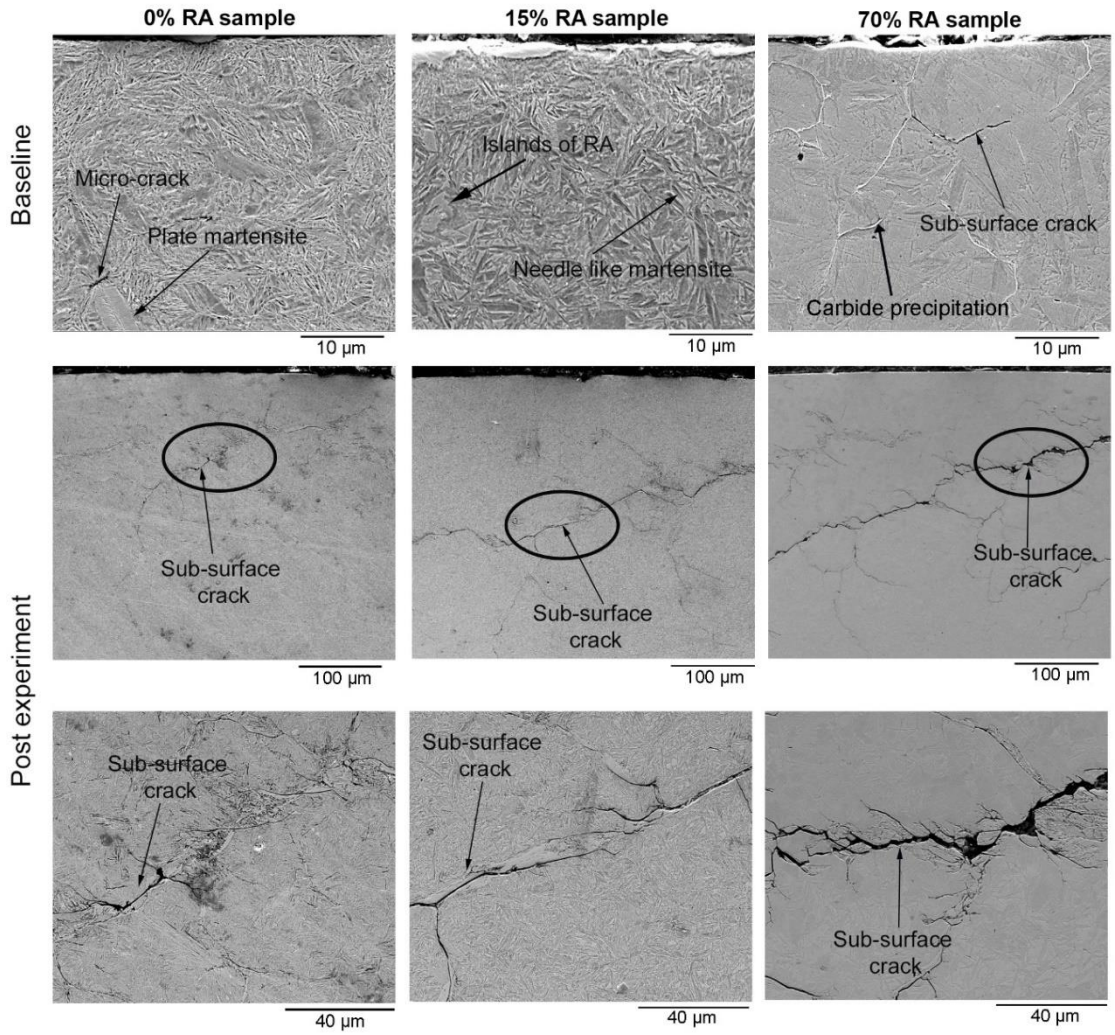

Figure 6.8: Cross-sectional microstructure for baseline and failed samples

If the RCF test condition is set in such a way that the propagation of surface-initiated micropitting occurred, this was accompanied with a gradual increase in accelerometer signal and these tests never showed any spalling. Micropitting and spalling are two competitive modes of failure. To replicate spalling in a benchtop test rig it is necessary to design the test conditions in such a way that it creates a favorable environment in the contact surface region for spalling. Stabilized contact surface condition where there is no gradual increase of surface micropits helps in initiation and propagation of the sub-surface cracks during their N1 period of RCF life. After certain RCF cycles these cracks

suddenly deviate their direction and propagate to surface creating spall on the contact surface. It can be observed from the zoomed view of the crack networks in all three types of samples (Figure 6.8) that the main crack propagates in circumferential direction and various sub-cracks form during the propagation. Some of these sub-cracks propagate to surface. This leads to delamination of the whole bulk material and results in deep spalls on surface.

6.6 Conclusions

Steel samples with an RA range of 0-70% were prepared to evaluate the effect of RA on macropitting or spalling by varying carbon potential (1.2 to 2%) and tempering temperature and time. Experiments revealed that microstructure with almost no RA showed the lowest spalling life. 70% RA samples showed better macropitting life compared to 0% RA samples even though it had larger sub-surface cracks at baseline condition. If RCF life for 0% and 15% RA samples are compared, both samples had insignificant sub-surface defects but 15% RA samples showed significantly improved macropitting life. In case of 70% RA samples, although they had very high RA but due to sub-surface cracks these samples did not show significantly higher RCF life than 15% RA samples. These observations confirm that increasing RA and decreasing sub-surface cracks at baseline condition can help to enhance macropitting life. The 0% RA samples had maximum residual stress but still showed lowest spalling life. Thus, the baseline residual stress cannot be the main factor to control macropitting behavior. The failure mechanism for all three samples were similar. Sub-surface cracks initially propagated in the circumferential direction and suddenly deviated upwards to create a spall on the surface. Thus, in all cases spalling was due to sub-surface crack initiation and

propagation. Samples with medium and high RA showed clear evidence of RA transforming to martensite. Higher amounts of RA can create more barriers for fatigue crack growth and therefore macropitting life is improved. Secondly, inherent ductility of austenite also plays a beneficial role to delay crack initiation and propagation.

The study helps establish the role of RA on macropitting in the context of other mechanical and microstructural phenomena as well as the correlation of behavior to heat treatment routes for preferred fatigue life. Overall, the findings will provide valuable input for the design and manufacturing of drivetrain components for a wide range of applications under low lambda conditions ranging from agricultural equipment to the wind energy sectors.

6.7 Acknowledgements

The authors would like to thank Matt Smeeth from PCS Instruments and Ian Griffin from Wallwork for their help with sample preparation, Warren Straszheim in the Materials Analysis and Research Laboratory (MARL) for help with SEM imaging, Erina Kagami in Rigaku Corporation for assisting with the XRD measurements and Benjamin Gould in Argonne National Laboratory for help in microstructural observation. Partial funding for this work was provided by John Deere Product Engineering Center in Waterloo, Iowa and Iowa State University.

6.8 References

1. Wilde, R.A., *Failures in Gears and Related Machine Components.* National Bureau of Standards Special Publication 423, 1976: p. 55-66.

2. Dommarco, R.C., et al., *Residual stresses and retained austenite evolution in SAE 52100 steel under non-ideal rolling contact loading.* Wear, 2004. **257**(11): p. 1081-1088.

3. Shen, Y., et al., *Effect of retained austenite - Compressive residual stresses on rolling contact fatigue life of carburized AISI 8620 steel.* International Journal of Fatigue, 2015. **75**: p. 135-144.

4. D'Errico, F., *Micropitting Damage Mechanism on Hardened and Tempered, Nitrided, and Carburizing Steels.* Materials and Manufacturing Processes, 2011. **26**(1): p. 7-13.

5. Mahmoudi, B., et al., *Influence of a WC/a-C:H Coating on Micropitting Wear of Bearing Steel.* Tribology & Lubrication Technology, 2015. **71**(4): p. 24-27.

6. Rivero, I.V. and C.O. Ruud, *Deviation of residual stress patterns in 52100 bearing steel due to inherent microstructural transformations after rolling contact.* Materials Characterization, 2004. **53**(5): p. 381-393.

7. Bakoglidis, K.D., et al., *Rolling performance of carbon nitride-coated bearing components in different lubrication regimes.* Tribology International, 2017. **114**: p. 141-151.

8. Soltanahmadi, S., et al., *Investigation of the effect of a diamine-based friction modifier on micropitting and the properties of tribofilms in rolling-sliding contacts.* Journal of Physics D-Applied Physics, 2016. **49**(50).

9. Moallem, H., S. Akbarzadeh, and A. Ariaei, *Prediction of micropitting life in spur gears operating under mixed-lubrication regime using load-sharing concept.* Proceedings of the Institution of Mechanical Engineers Part J-Journal of Engineering Tribology, 2016. **230**(5): p. 591-599.

10. Wei, J., A.Q. Zhang, and P. Gao, *A study of spur gear pitting under EHL conditions: Theoretical analysis and experiments.* Tribology International, 2016. **94**: p. 146-154.

11. Soltanahmadi, S., et al., *Tribochemical study of micropitting in tribocorrosive lubricated contacts: The influence of water and relative humidity.* Tribology International, 2017. **107**: p. 184-198.

12. Ding, Y. and N.F. Rieger, *Spalling formation mechanism for gears.* Wear, 2003. **254**(12): p. 1307-1317.

13. Alban, L.E., *Systematic Analysis of Gear Failure*. 1985: ASM International: Metals Park, OH.

14. Ding, Y. and J.A. Gear, *Spalling depth prediction model.* Wear, 2009. **267**(5-8): p. 1181-1190.

15. Xu, G. and F. Sadeghi, *Spall initiation and propagation due to debris denting.* Wear, 1996. **201**(1-2): p. 106-116.

16. Kudish, I.I., *A new statistical model of contact fatigue.* Tribology Transactions, 2000. **43**(4): p. 711-721.

17. Tallian, T.E., *Spalling Life Model with Relaxed Distribution Constraints, for Rough Hertz Line Contacts.* Journal of Tribology-Transactions of the Asme, 1993. **115**(3): p. 453-459.

18. Blake, J.W. and C.F. Draper, *Further Development of a Predictive Pitting Model for Gears - Improvements in the Life Prediction Analysis.* Tribology Transactions, 1994. **37**(2): p. 237-244.

19. Way, S., *Pitting due to rolling contact.* Journal of Appllied Mechanics, 1935. **57**: p. A49-A58.

20. Cheng, H.S., L.M. Keer, and T. Mura, *Analytical modelling of surface pitting in simulated gear-teeth contacts.* SAE Technical Paper, 1984: p. 4.987–4.995.

21. Raje, N., F. Sadeghi, and R.G. Rateick, *A statistical damage mechanics model for subsurface initiated spalling in rolling contacts.* Journal of Tribology-Transactions of the Asme, 2008. **130**(4).

22. Santus, C., et al., *Surface and subsurface rolling contact fatigue characteristic depths and proposal of stress indexes.* International Journal of Fatigue, 2012. **45**: p. 71-81.

23. Choi, Y. and C.R. Liu, *Spall progression life model for rolling contact verified by finish hard machined surfaces.* Wear, 2007. **262**(1-2): p. 24-35.

24. Roy, S. and S. Sundararajan, *The effect of heat treatment routes on the retained austenite and Tribomechanical properties of carburized AISI 8620 steel.* Surface & Coatings Technology, 2016. **308**: p. 236-243.

25. Roy, S., et al., *Effect of laser treatment parameters on surface modification and tribological behavior of AISI 8620 steel.* Tribology International, 2017. **112**: p. 94-102.

26. Kim, H.J. and Y.G. Kweon, *The effects of retained austenite on dry sliding wear behavior of carburized steels.* Wear, 1996. **193**(1): p. 8-15.

27. Verhoeven, J.D., *Steel Metallurgy for the Non-Metallurgist*. 2007: ASM International.

28. Jenson, A.D., S. Roy, and S. Sundararajan, *The evolution of hardness and tribofilm growth during running-in of case carburized steel under boundary lubrication.* Tribology International, 2018. **118**: p. 1-10.

29. Sadeghi, F., et al., *A Review of Rolling Contact Fatigue.* Journal of Tribology-Transactions of the Asme, 2009. **131**(4).

30. Aring;nmark, N., A. Karasev, and P.G. Jonsson, *The Effect of Different Non-Metallic Inclusions on the Machinability of Steels.* Materials, 2015. **8**(2): p. 751-783.

31. Marder, A.R., Benscote.Ao, and G. Krauss, *Microcracking Sensitivity in Fe-C Plate Martensite.* Metallurgical Transactions, 1970. **1**(6): p. 1545-&.

32. Wang, Y.H., et al., *Rolling Contact Fatigue Performances of Carburized and High-C Nanostructured Bainitic Steels.* Materials, 2016. **9**(12).

33. Ooi, G.T.C., S. Roy, and S. Sundararajan, *Investigating the effect of retained austenite and residual stress on rolling contact fatigue of carburized steel with XFEM and experimental approaches.* Materials Science & Engineering A, 2018. **Under review**.

34. Krupp, U., C. West, and H.J. Christ, *Deformation-induced martensite formation during cyclic deformation of metastable austenitic steel: Influence of temperature and carbon content.* Materials Science and Engineering a-Structural Materials Properties Microstructure and Processing, 2008. **481**: p. 713-717.

CHAPTER 7. EFFECT OF RETAINED AUSTENITE ON WHITE ETCHING CRACK BEHAVIOR OF CARBURIZED STEEL UNDER BOUNDARY LUBRICATION

Modified from a paper to be submitted in *Acta Materialia*

Sougata Roy, Benjamin Gould, Ye Zhou, Nicholaos G. Demas, Aaron C. Greco and Sriram Sundararajan

7.1 Abstract

The formation of white etching cracks (WECs) is a dominant failure mode in wind turbine gearbox bearings that can significantly shorten their operating life. Although the phenomenon of WECs has been reported in the field for over a decade, the driving mechanisms are still debated, and the impact of proposed mitigation techniques is not quantified. Leading hypotheses to inhibit the formation of WECs center on material solutions, including the use of steel with high levels of retained austenite (RA). The present work aims to explore the impact of RA on the formation of WECs within AISI 8620 steel under boundary lubrication. A three ring-on-roller bench top test rig was used to systematically replicate WECs in samples with different levels of RA. While varying levels of RA had a minimal effect on time until failure, a significant effect on crack morphology was observed. Additionally, potential underlying mechanisms of WEA formation were elucidated. Under the current test conditions, the microstructural alterations adjacent to the cracks in the lower RA samples were more developed compared to those of the higher RA samples. Additionally, the WEC networks in the high RA samples contained significantly more crack branches than those of the low RA samples.

7.2 Introduction

Industrial scale drivetrain bearings, particularly those used in wind turbines, often exhibit premature spalling or macro-pitting well before reaching their rolling contact fatigue (RCF) design life [1-3]. In many of these cases, the premature failures are caused by broad-branching crack networks surrounded by local regions of nano-grained, microstructurally altered steel [4-8]. When bearings containing these cracks are sectioned and etched with Nital (nitric acid and ethanol), the nano-grained regions resist the etchant, and appear white in contrast with the surrounding steel. Because of this, these failures are often referred to as "White etching cracks" (WECs). Figure 7.1 shows a damaged bearing, and a section of the WEC network which caused the damage.

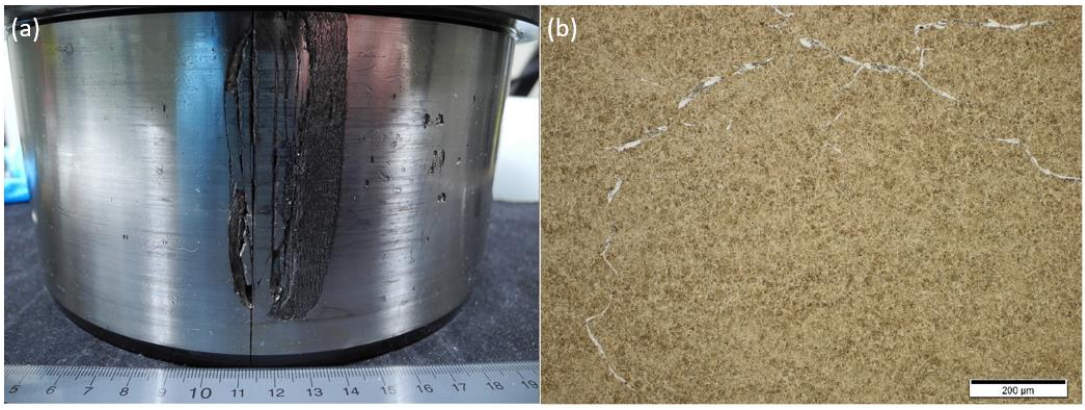

Figure 7.1 (a) A failed high-speed shaft bearing pulled from a wind turbine, and (b) a section of the WEC network which caused the failure. Image taken from [9]

The cause of WEC networks in field bearings is unknown. However, that the microstructural alterations adjacent to the crack faces must form due to local excess in energy causing atomic diffusion or recrystallization. Previous researchers have attributed the formation of WECs to multiple drivers, including: applied strain due to normal loading [10-24], torque reversals leading to impacts [18, 19, 25], hydrogen release from degraded

or contaminated lubricants [16, 26, 27], electrical discharge [28], tensile frictional stresses at the contact surface [29], and sliding contacts induced via acceleration or under-loading [30-32]. Because no consensus exists on WEC drivers in the field, researchers have taken multiple avenues with regards to recreating these crack networks in benchtop tests. These efforts include: the use of specific lubricant formulations thought to promote the formation of WECs [9, 24, 33-39], pre-charging test samples with hydrogen [22, 40-55], grain boundary embrittlement induced via heat treatment [56], the application of external electrical load [28], excessive slip [9, 24, 57, 58], and impact loading [59]. In-depth reviews of the leading hypotheses as to the factors responsible for the formation of WECs can be found in [17, 60]. While there are many unknowns surrounding WECs, recent analysis by Gould et al. [60, 61] elucidated many of the formation mechanisms of these crack networks within field bearings. Gould et al.used X-ray tomography to investigate the morphology of newly initiated WECs. It was found that the WECs studied initiated in the subsurface of bearings, preferentially at inclusions that contained both a manganese sulfide component and an aluminum oxide component. Additionally, it was found that formation of a crack is a pre-requisite to the formation of microstructural alterations [61]. This suggests that efforts to mitigate the formation of WECs should focus on combating the formation of subsurface crack networks.

Industry has proposed multiple solutions that aim to eliminate the formation of WECs. These include the use of soft black oxide coatings to protect bearings from embrittlement stemming from contamination or lubricant decomposition, the use of hard coatings, such as diamond-like carbon, to mitigate the formation of nascent steel surfaces, the use of case carburization to impede subsurface crack initiation and propagation, and

the use of specific steel microstructures, particularly those rich in retained austenite (RA), to inhibit cracking [62, 63]. While numerous proposed solutions exist, the public literature is severely lacking when it comes to quantifying the effectiveness of each of these solutions. Therefore, the aim of the current work is to investigate one of these proposed solutions with regards to the formation of WECs, namely the effect of varying the level of RA within manufactured steel samples.

7.3 Materials

7.3.1 Sample preparation and characterization

In this study, samples with different levels of RA and residual stress were achieved by carburizing and tempering [64-66]. Increasing carbon potential decreases martensite start (M_s) and martensite finish (M_f) temperature [66]. This results in incomplete conversion of austenite to martensite and helps to increase retained austenite content on surface. On the other hand, increasing tempering temperature and time help to convert existing retained austenite to bainite or pearlite depending on tempering time and temperature [64]. In this study, the carbon potential was varied from 1.2 to 2%. The tempering temperature and time were varied from 50°C for 1 hour to 400°C for 2 hours. A Rigaku SmartLab X-ray diffractometer with micro-diffraction capability was used to quantify RA percentage of the samples after heat treatment. A Cu Kα target (wavelength 1.54 Å) was used with a target voltage of 40 KV and current 44 mA. XRD scan data for a range of 40 to 90 degrees (2θ angle) was analyzed using TOPAS software to determine the amount of RA in those samples [17, 65, 67].

The residual stress level of the samples was measured using Cr XRD (wavelength 2.29 Å) with a target voltage of 35KV and current of 1.5 mA. For these measurements, the (211)-

peak of Cr Kα radiation was used to determine the peak positions for residual stress determination. The resulting levels of RA and residual stress of the samples prepared by three different heat treatment schemes are shown in Table 7.1. Subsequently, the three levels of RA which are approximated at 70%, 15% and 0% RA will be referred to as "High RA, "Medium RA" and "Low RA". Carburizing helped to generate compressive residual stress on all sample surfaces. High temperature tempering resulted in a phase transformation of austenite. This helps in the expansion of surface layer due to volumetric increase during the phase transformation [64]. Consequently, higher compressive residual stresses were observed in lower RA samples. Following the heat treatment, the samples were ground and polished to achieve an average surface roughness of 0.22 ±0.02 μm over a scan size of 1 mm × 0.6 mm.

Table 7.1: RA and residual stress levels on the carburized samples

Heat treatment scheme	RA level	RA%	Compressive residual stress (MPa)
2% C potential carburizing with tempering at 50°C for 1 hr.	'High RA'	69.7±3.7	153.2±49.3
1.2% C potential carburizing with tempering at 190°C for 1.5 hrs.	'Medium RA'	14.5±1.9	251±42.9
1.2%C potential carburizing with tempering at 400°C for 2hrs	'Low RA'	0.4±0.2	493.3±11.3

7.3.2 Microhardness tests

The resulting subsurface hardness for each heat treatment was determined by probing an untested roller at multiple points below the contact surface using a Vickers micro-indenter with a mass of 400g at an average spacing of around 100 microns. This data is shown in Figure 7.2. It is worth noting that the surface hardness for the Low RA sample was lower than the Medium and High RA sample due to the higher tempering temperature used during sample preparation. Additionally, the hardness of the High RA sample actually increased with depth below the contact surface, until a depth of around 400microns. The authors hypothesize that the reason for this increase is that, the amount of diffused carbon decreased with depth below the contact surface due to the carburizing heat treatment. Therefore, within the case layer, the amount of hard martensite increased with depth, and the amount of softer RA decreased with depth.

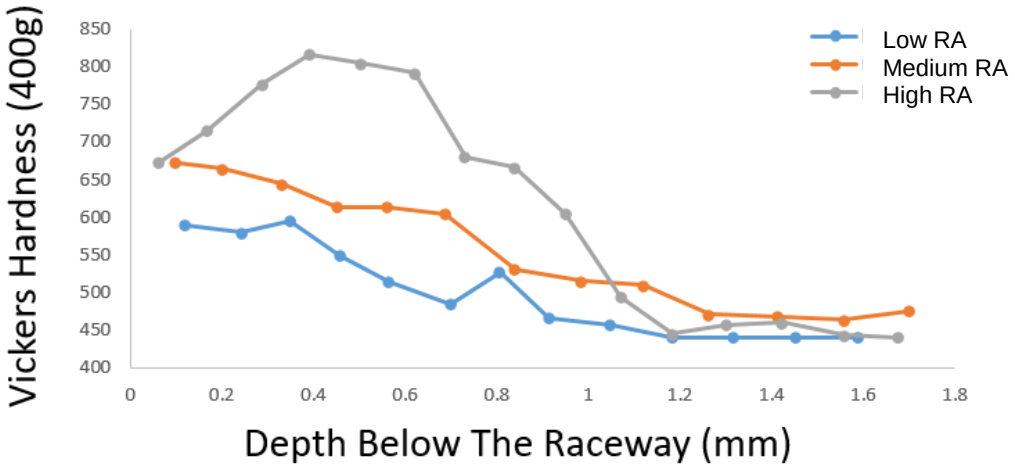

Figure 7.2: A chart showing the measured hardness of rollers of varying heat treatment vs depth below the raceway surface. The hardness was measured at multiple points using a Vickers micro-indenter with a load of 400g.

7.4 Methods

7.4.1 Rolling contact fatigue tests

Rolling contact fatigue tests were performed using a Micro Pitting Rig (MPR) from PCS instruments (London, UK) [68]. A schematic representation of the experimental setup is shown Figure 7.3a. The MPR is a computer controlled disc-on-disc contact instrument in which a central roller (sample) is in contact with three harder counter face rings as shown in Figure 7.3b. Therefore, the roller experiences three contact cycles per revolution at a constant contact pressure. The speeds of the rings and rollers are controlled independently which allows different combinations of rolling and sliding contact. The MPR utilizes a dip lubrication system, with the oil level 27.8 millimeters below the center of the roller and a sump volume of 150 milliliters. The unit is also temperature controlled to maintain the desired operating temperature of the lubricant sump. A chamfered roller with a 1mm face-width (see Figure 7.3c) was used for the tests performed in this study. The diameter of the roller and the rings was 12 mm and 54 mm respectively. The relative amount of rolling and sliding during testing is determined by the slide-to-roll ratio (SRR) and is defined as follows:

$$\text{SRR}\ (\%) = \frac{U_1 - U_2}{1/2(U_1 + U_2)} \cdot 100 \tag{7.1}$$

where U_1 is the speed of the rings and U_2 is the speed of the roller. All tests were conducted using the conditions listed in Table 7.2, and were derived from MPR conditions which have been previously used to generate WECs [9, 24].

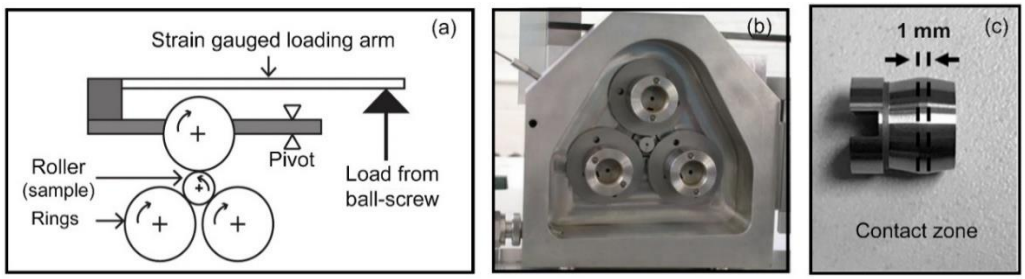

Figure 7.3: a- Schematic diagram of micropitting test rig (MPR); b- Experimental setup of roller and rings inside MPR chamber; c-Representative image of roller (test sample)

Table 7.2: Operating test conditions

Test parameter	
Entrainment velocity (m/sec)	1
Slide to roll ratio (%)	-30
Normal Load (N)	500
Maximum Hertzian contact pressure (GPa)	1.9
Lubricant sump temperature (°C)	80
Oil film thickness (nm)[a]	51
Lambda ratio	0.16

[a] Estimated using Eq. (7.2)

The lubricating oil used in this study was an API group II base oil with Zinc dialkyldithiophosphate (ZDDP) anti-wear and other additives. The lubricating oil was sheared before testing by running it through a piston pump for 48 hours to ensure no change in viscosity would occur due to shearing during rolling contact fatigue tests. The kinematic viscosity of the sheared oil was 50.51–51.44cSt at 40 °C and 7.56–7.81cSt at 100 °C.

Minimum oil film thickness (H_{min}) for the experiments was calculated using the Pan-Hamrock equation mentioned below,

$$H_{min} = 1.714\, U^{0.694} G^{0.568} W^{-0.128} \tag{7.2}$$

where, U is dimensionless speed parameter, G is the dimensionless material parameter, and W is the dimensionless load parameter. The film thickness ratio (λ) was calculated using H_{min} and measured initial composite roughness (Rq) to verify tests were run under boundary lubrication.

An accelerometer attached to the instrument provides peak to peak (P/P) values of vibration experienced by the roller. Crack propagation and surface deformation during RCF tests lead to increased vibrations and increased P/P values. All experiments were run till the system detected a P/P accelerometer signal of 10g. In our tests, this value was reached due to formation of macropits on the sample surface. Each experiment included a 2-min time duration 'ramp-up' step where the test parameters were ramped to preset conditions (as mentioned in Table 7.2) for the upcoming fatigue step. A Sensofar 3D non-contact optical surface profilometer using focus variation microscopy mode was used to capture the height maps of the macropits at the end of each tests.

7.4.2 White etching crack characterization protocol

At the end of every test, the respective rollers were sectioned in the circumferential-depth plane. Figure 7.4 shows a schematic describing the cross-sectional plan for observing WECs in different samples. Samples were then mounted in Bakelite, and polished to multiple locations along the wear track using a series of polishing steps: 220 grit (grinding), followed by 9 µm, 3 µm, and 1µm diamond polishing medium. At each section, the samples were etched with a 3% Nital solution and the subsurface of each sample was examined for microstructural alterations using and optical microscope. When necessary, additional analysis was performed on an FEI Quanta 400F scanning electron microscope (SEM).

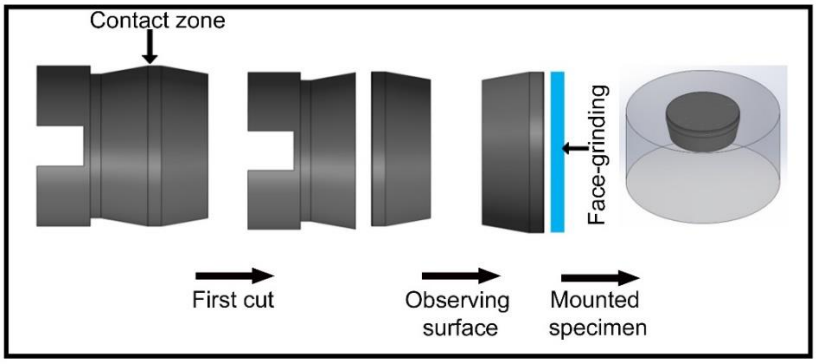

Figure 7.4: Cross-sectional plan for WECs observation

7.5 Results

7.5.1 Rolling contact fatigue test observations

Table 7.3 shows the results of the RCF tests. It can be observed that the low RA samples had slightly lower RCF life compared to medium and high RA samples. While there was no statistically significant difference in RCF life among medium and high RA samples, the medium RA samples had a slightly larger average time until failure.

Table 7.3: Rolling contact fatigue life (P/P accelerometer to reach 10g)

Sample	Test trials	RCF life (million)
High RA	Test 01	20.4
	Test 02	18.9
Medium RA	Test 03	23
	Test 04	22.3
Low RA	Test 05	16.3
	Test 06	12.2

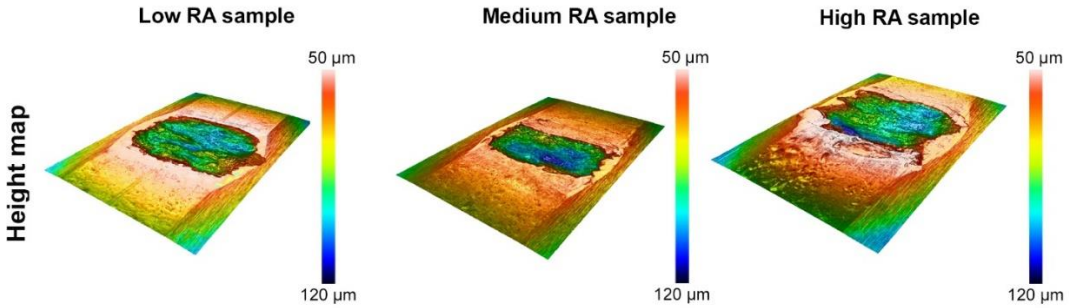

Figure 7.5: Representative height maps of macropits formed during RCF tests

In all cases, the tests were automatically shut down due to the formation of a macropit. Figure 7.5 shows the representative height maps of macropits for different RA samples. The maximum depth of the pits was within 100-120 µm. There was no significant trend observed in terms of pit size and depths among the samples from different RA levels.

Figure 7.6a shows a representative evolution of the P/P accelerometer signal for the different RA samples during RCF testing. In all cases, the RCF life can be divided into two periods N1 and N2. The N1 period shows no significant change in P/P accelerometer signal because crack initiation and propagation did not affect the vibration amplitude. N2 period shows a significant change in the vibration amplitude due to formation of spall on the surface. Thus, N2 represents the spall progression period which is very short compared to N1. This observation is consistent with observations made by previous researchers [69] and shows that macropitting or spalling is a catastrophic failure which occurs in a very short time. Figure 7.6b shows the optical micrograph of the roller at baseline condition. Figure 7.6c shows the accelerometer signal after 12 million RCF cycles and optical micrographs of spalls which resulted increase of P/P accelerometer signal to 10g.

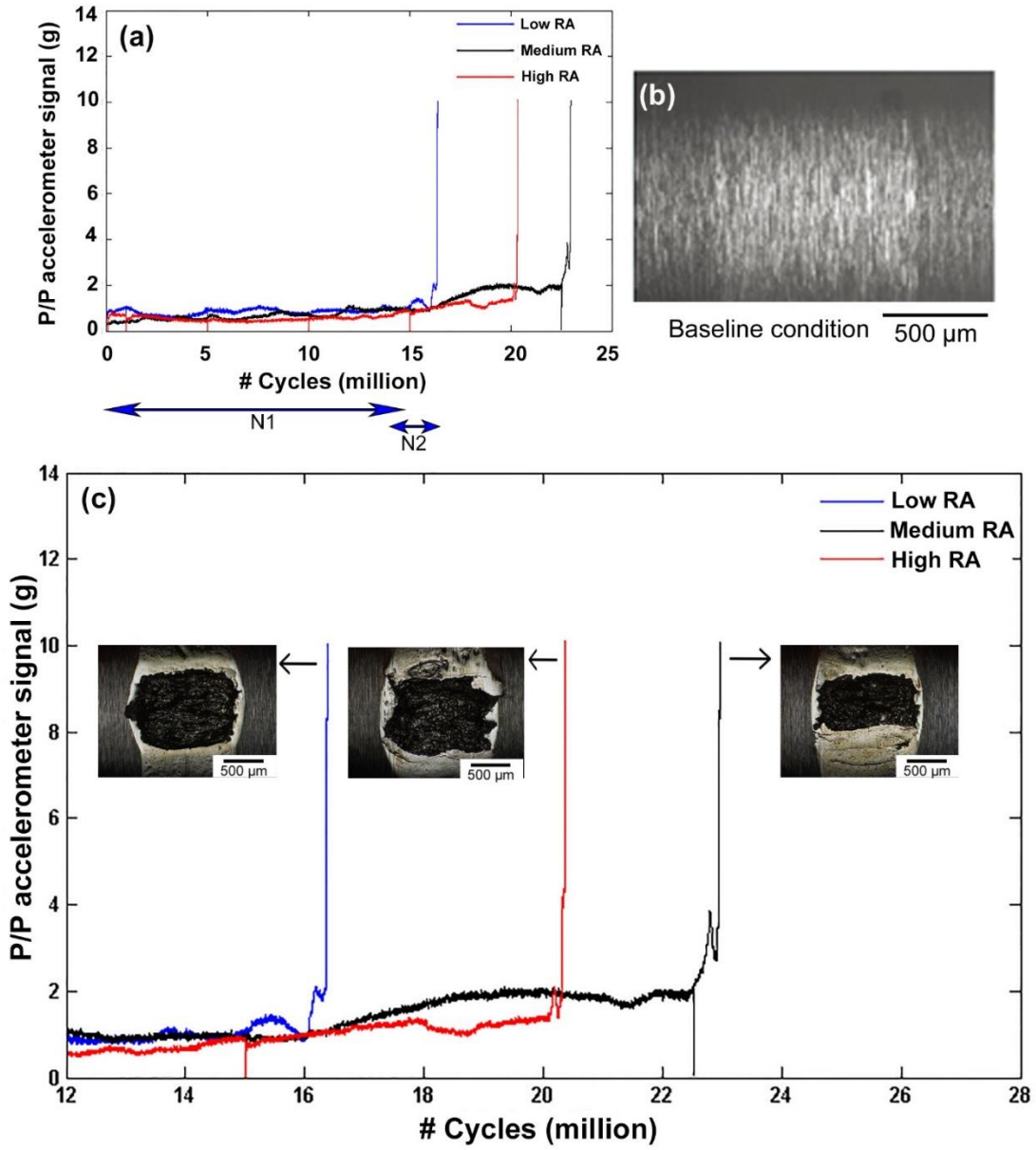

Figure 7.6: Evolution of P/P accelerometer signal of different RA roller samples: (a) P/P signal for whole RCF life where N1 is the spall initiation period and N2 is the spall progression period; (b) optical micrograph of roller surface at baseline condition; (c) optical micrograph of roller surface at the end of their RCF life with accelerometer signal from 12 million cycles till end-of-test

7.6 Discussion

7.6.1 Effect of RA on WEC formation and Crack morphology

It was observed that the level of retained austenite had a drastic effect on the morphology of the crack networks, as well as the WEA that accompanied them. The WEC networks that formed in the samples with higher levels of RA contained a larger number of crack branches, and the WEA adjacent to the crack faces was less developed. Examples of crack networks displaying these observations are shown in Figure 7.7 and Figure 7.8.

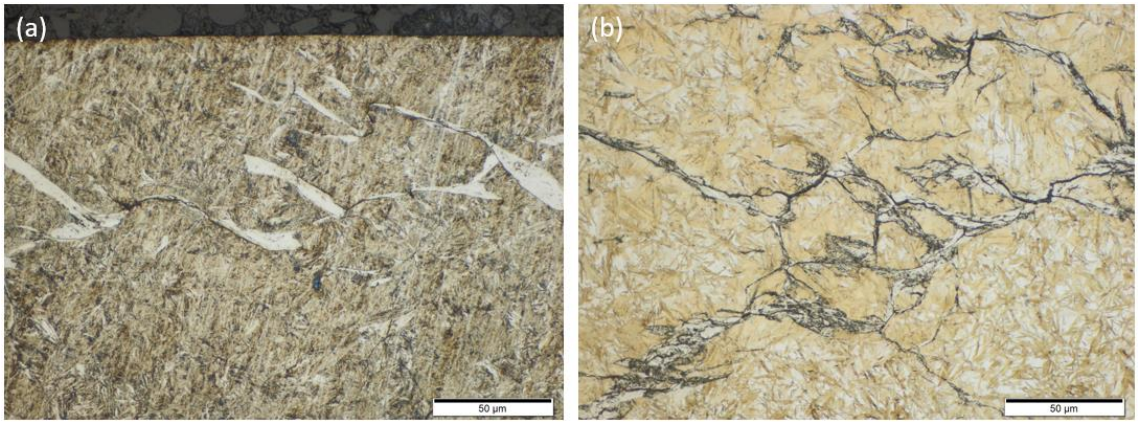

Figure 7.7: (a) A WEC network observed within Test 6, a sample with a low level of RA and (b) a WEC network within Test 2, a sample with a high level of RA. These images show the increase in the branching nature of the WEC networks documented in the higher RA samples.

As stated above, the method that was used to induce high levels of RA was supersaturating the outer layer of the samples with carbon. If enough carbon exists locally, and the steel is constrained from expanding in volume, then the microstructure of the steel must remain in the face center cubic (FCC) configuration of austenite as opposed to the body center cubic (BCC) lattice of ferrite, or the body center tetragonal (BCT) lattice of martensite. This is due to the fact that the FCC configuration has a much higher carbon solubility limit than that of a BCC or BCT structure [70]. As crack networks initiate and propagate through the subsurface of the samples containing large amount of RA, they

inevitably interact with regions of RA. The spacing induced by the crack network (i.e. the width of the crack) will allow the RA adjacent to the crack to expand from its FCC lattice to the BCT lattice of martensite. This expansion, in turn, will place a significant compressive stress on the crack tip impeding further crack propagation. The crack will then propagate in a new direction based on the path of least resistance for the given stress state, significant branching within the higher RA samples. Each time a crack face interacts with a region of RA, the RA transforms, leading to a new path of least resistance, and therefore a new direction of crack propagation. Figure 7.9 supports this hypothesis. This figure shows two significantly branched crack networks within a high RA sample. As stated above, regions of RA appear white when etched. Within Figure 7.9, it can be observed that steel adjacent to the crack network is devoid of RA, thereby indicating that the RA that has interacted with the crack network has undergone a transformation to martensite.

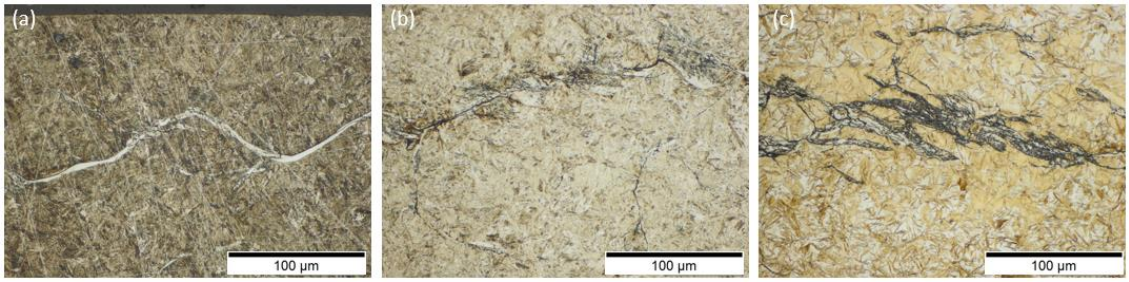

Figure 7.8: Three images showing how increased levels of RA within samples led to changes in the appearance of the microstructural alterations which appear adjacent to the crack networks in each sample. (a) shows Test 5 (low RA), (b) shows Test 4 (mid RA), and (c) shows Test 2 (high RA). It was documented that the rollers which contained a lower level of RA formed WEA that was far more defined then that of the higher levels of RA.

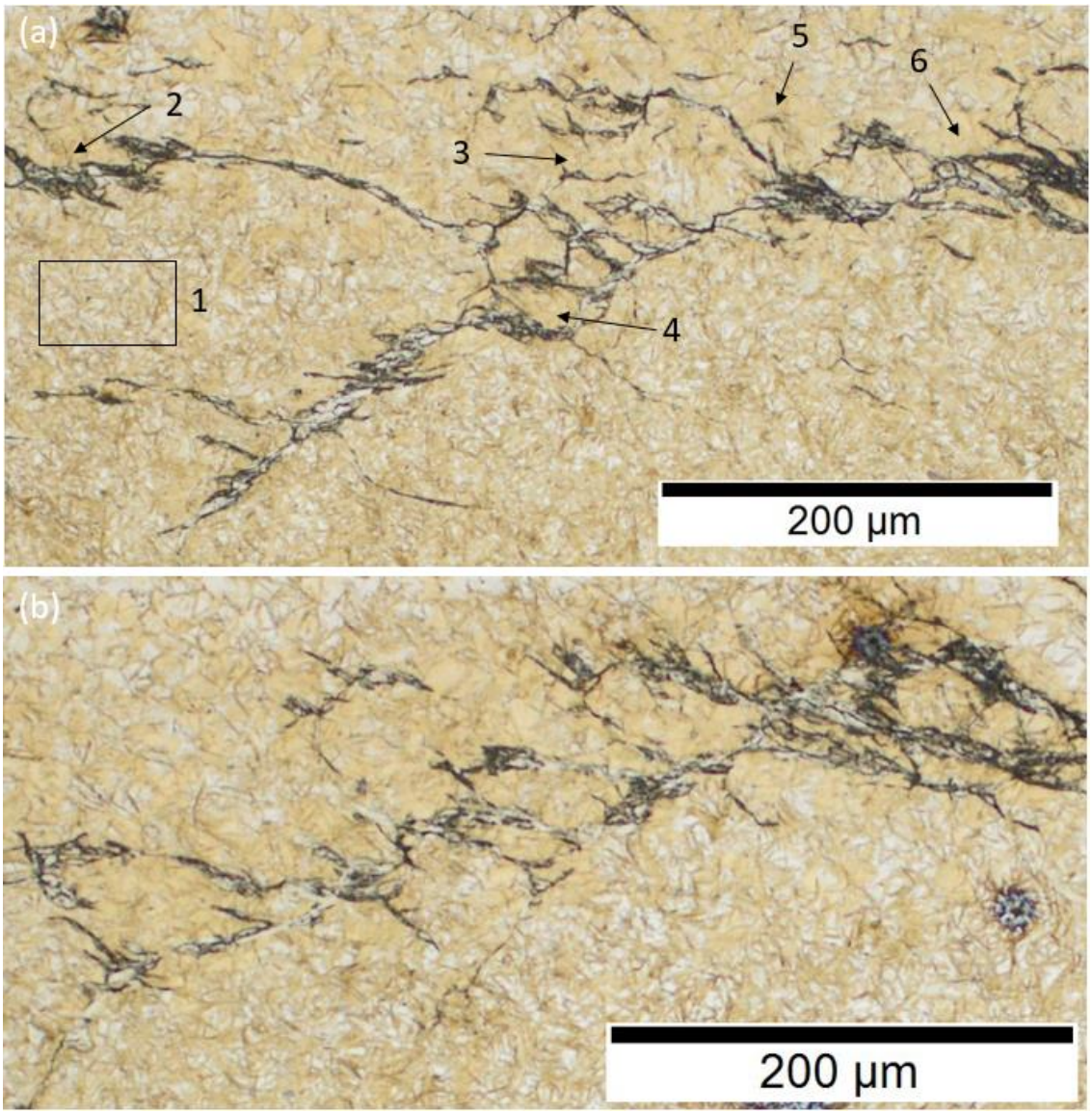

Figure 7.9: (a) an image of a broad branching WEC network within (Test 2). Zone 1 within this image shows the matrix microstructure, which is unaffected by the cracking failure. This zone shows large regions of lighter etching, corresponding to areas rich in RA. Regions 2-6, which are all adjacent to crack faces, show a clear depletion of this lighter etching. This indicates that these regions have transformed from RA to Martensite due to the presence of the crack. (b) Shows another WEC network within this sample, where it can be observed, similar to (a), that the steel adjacent to the crack faces contains far less RA then the steel unaffected by the crack.

It was also observed that the regions of WEA adjacent to the crack networks were less developed in the higher RA samples. This can be seen in Figure 7.7 and in Figure 7.8. The

leading hypotheses as to why WEA forms adjacent to crack networks are based on the local accumulation of energy which leads to a gradual increase in the dislocation density [17, 24, 71, 72]. As the dislocation density increases, the dislocations rearrange to form new, smaller cells, causing gradual grain refinement. The energy that drives this process likely comes from multiple origins, including: strain-based energy release due to over-rolling, frictional energy generated due to sliding at the contact surface, and frictional energy generated at the crack interface due to crack face rubbing. The authors have two theories as to why the samples with higher levels of RA contained less developed WEAs than the samples with low levels of RA. The first theory is that the cracks contained within the higher RA samples had less time from initiation to a macropitting failure, and thus less time to accrue localized energy before a failure. This idea stems from the fact that the medium and high RA samples were much harder, and therefore less tough, than the low RA samples. The second theory as to why these observable differences in WEA morphology occur has to do with differences in the rate of energy generated due to crack face rubbing. In the cases of WECs generated in steels with a low level of RA, such as the images shown in Figure 7.7a, 7.8a as well as most 52100 through hardened steels, the WEAs adjacent to the crack networks are distinct and well defined. An SEM image showing a well-defined WEA within a low RA sample is shown in Figure 7.10a. Within these well-defined WEAs there are normally very few crack branches. Therefore, when the region is loaded, the imposed stress is concentrated on a single crack causing the two crack faces to be easily compressed together, the shear component of the stress state causes crack face rubbing, and subsequent energy is released which increases the dislocation density adjacent to the cracks. However, in the case of a crack network within a high RA sample,

there are numerous crack branches within a local area for the reasons stated above. Therefore, when a region containing multiple crack networks is stressed, the numerous crack branches in a local area all compress to varying levels. In other words, there are significantly more degrees of freedom in terms of how the compression can be accommodated. Therefore, a multitude of cracks can take the various shear and compressive components of over-rolling, leading to a decrease in energy localization adjacent to any single crack face. Because of this, gradual microstructural alterations form adjacent to the numerous cracks in a local area, as opposed to well-defined microstructural alterations forming adjacent to one crack face. An example of a non-well-defined WEA within a high RA sample is shown in Figure 7.10b.

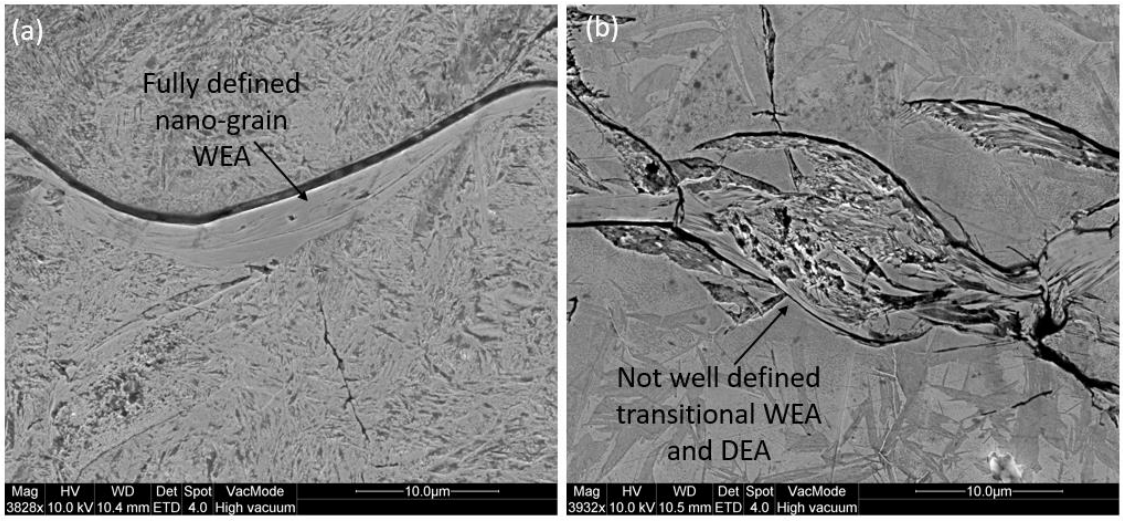

Figure 7.10: Two SEM images showing the differences in the appearance of the WEA within the Low RA samples (a) and the high RA samples (b).

7.7 Conclusions

Steel samples with a retained austenite (RA) range of 0-70% were prepared to evaluate the effect of RA on macropitting by varying carbon potential (1.2 to 2%) and tempering temperature and time. These samples were tested within the PCS Instruments micro-pitting

rig under conditions which were previously documented to lead to the formation of WECs [9, 24].

- The average RCF test life for high, medium and low RA samples based on two tests from each batch of samples were 19.7 million, 22.7 million and 14.3 million cycles respectively.
- Varying the RA level also caused drastic differences in the morphology of the WECs which developed within the samples.
- Samples with higher levels of RA contained far more branching crack networks, and the WEA adjacent to the crack networks was less defined. This shows positive impact of RA on WEC formation.

The study helps establish the role of RA on WEC behavior in the context of other mechanical and microstructural phenomena as well as the correlation of rolling contact fatigue behavior to heat treatment routes. Overall, the findings provide valuable input for the design and manufacturing of drivetrain components for a wide range of applications under boundary lubrication ranging from agricultural equipment to the wind energy sector.

7.8 Acknowledgements

The authors would like to thank Matt Smeeth from PCS Instruments and Ian Griffin from Wallwork for their help with sample preparation, Scott Schlorholtz in the Materials Analysis and Research Laboratory (MARL) for help with XRD data postprocessing, Erina Kagami in Rigaku Corporation for assisting with the XRD measurements, Dr. Maria De La Cinta Lorenzo Martin for her assistance with electron microscopy, and Dr. Oyelayo Ajayi for his helpful discussion on metallurgy. Partial funding for this work was provided

by John Deere Product Engineering Center in Waterloo, Iowa and Iowa State University. This work was also supported by the U.S. Department of Energy Office of Energy Efficiency and Renewable Energy, Wind Energy Technology Office under Contract No. DE-AC02-06CH11357. The authors are grateful to DOE Project Managers Mr. Michael Derby and Mr. Brad Ring for their support and encouragement. Use of the Center for Nanoscale Materials an Office of Science user facility was supported by the U.S. Department of Energy Office of Science, Office of Basic Energy Sciences under Contract No. DE-AC02-06CH11357.

7.9 References

1. Kotzalas, M.N. and G.L. Doll, *Tribological advancements for reliable wind turbine performance.* Philosophical Transactions of the Royal Society a-Mathematical Physical and Engineering Sciences, 2010. **368**(1929): p. 4829-4850.

2. Musial, W., S. Butterfield, and B. McNiff, *Improving wind turbine gearbox reliability,* in *European Wind Energy Conference* 2007: Milan Italy. p. 7-10.

3. Greco, A., et al., *Material wear and fatigue in wind turbine Systems.* Wear, 2013. **302**(1-2): p. 1583-1591.

4. Kang, J.H., et al., *Solute redistribution in the nanocrystalline structure formed in bearing steels.* Scripta Materialia, 2013. **69**(8): p. 630-633.

5. Smelova, V., et al., *Electron microscopy investigations of microstructural alterations due to classical Rolling Contact Fatigue (RCF) in martensitic AISI 52100 bearing steel.* International Journal of Fatigue, 2017. **98**: p. 142-154.

6. Smelova, V., et al., *Microstructural changes in White Etching Cracks (WECs) and their relationship with those in Dark Etching Region (DER) and White Etching Bands (WEBs) due to Rolling Contact Fatigue (RCF).* International Journal of Fatigue, 2017. **100**: p. 148-158.

7. Su, Y.-S., et al., *Review of the damage mechanism in wind turbine gearbox bearings under rolling contact fatigue.* Frontiers of Mechanical Engineering, 2017: p. 1-8.

8. Su, Y.S., et al., *Deformation-induced amorphization and austenitization in white etching area of a martensite bearing steel under rolling contact fatigue.* International Journal of Fatigue, 2017. **105**: p. 160-168.

9. Gould, B. and A. Greco, *The Influence of Sliding and Contact Severity on the Generation of White Etching Cracks.* Tribology Letters, 2015. **60**(2).

10. Grabulov, A., R. Petrov, and H.W. Zandbergen, *EBSD investigation of the crack initiation and TEM/FIB analyses of the microstructural changes around the cracks formed under Rolling Contact Fatigue (RCF).* International Journal of Fatigue, 2010. **32**(3): p. 576-583.

11. Grabulov, A., U. Ziese, and H.W. Zandbergen, *TEM/SEM investigation of microstructural changes within the white etching area under rolling contact fatigue and 3-D crack reconstruction by focused ion beam.* Scripta Materialia, 2007. **57**(7): p. 635-638.

12. Martin, J.A., S.F. Borgese, and Eberhard.Ad, *Microstructural Alterations of Rolling - Bearing Steel Undergoing Cyclic Stressing.* Journal of Basic Engineering, 1966. **88**(3): p. 555-&.

13. Obrien, J.L. and A.H. King, *Electron Microscopy of Stress-Induced Structural Alterations near Inclusions in Bearing Steels.* Journal of Basic Engineering, 1966. **88**(3): p. 568-&.

14. Lund, T.B., J. Beswick, and S.W. Dean, *Sub-Surface Initiated Rolling Contact Fatigue—Influence of Non-Metallic Inclusions.* Journal of ASTM International, 2010. **7**(5): p. 102559.

15. Scott, D., B. Loy, and G.H. Mills, *Paper 10: Metallurgical Aspects of Rolling Contact Fatigue.* Proceedings of the Institution of Mechanical Engineers SAGE Journals, 1966: p. 94-103.

16. Stadler, K., J. Lai, and R. Vegter, *A Review: The Dilemma With Premature White Etching Crack (WEC) Bearing Failures.* Bearing Steel Technologies: 10th Volume, Advances in Steel Technologies for Rolling Bearings, ASTM International, , 2015. **487-508**.

17. Evans, M.H., *An updated review: white etching cracks (WECs) and axial cracks in wind turbine gearbox bearings.* Materials Science and Technology, 2016. **32**(11): p. 1133-1169.

18. Luyckx, J. *Hammering Wear Impact Fatigue Hypothesis WEC/irWEA failure mode on roller bearings*. 2011.

19. Hyde, S. *White Etch Areas: Metallurgical Characterization & Atomistic Modeling*. 2014.

20. Solano-Alvarez, W. and H.K.D.H. Bhadeshia, *White-Etching Matter in Bearing Steel. Part II: Distinguishing Cause and Effect in Bearing Steel Failure.*

Metallurgical and Materials Transactions a-Physical Metallurgy and Materials Science, 2014. **45a**(11): p. 4916-4931.

21. Bhadeshia, H.K.D.H., *Steels for bearings.* Progress in Materials Science, 2012. **57**(2): p. 268-435.

22. Evans, M.H., et al., *Serial sectioning investigation of butterfly and white etching crack (WEC) formation in wind turbine gearbox bearings.* Wear, 2013. **302**(1-2): p. 1573-1582.

23. Bruce, T., et al., *Characterisation of white etching crack damage in wind turbine gearbox bearings.* Wear, 2015. **338**: p. 164-177.

24. Gould, B. and A. Greco, *Investigating the Process of White Etching Crack Initiation in Bearing Steel.* Tribology Letters, 2016. **62**(2).

25. Errichello, R., et al. *Wind Trubine Tribology Seminar: A Recap*. 2011.

26. Holweger, W., *Progresses in solving White etching crack phenoma*, in *NREL - Gearbox reliability collaborative*. 2014: Golden, CO, USA.

27. Strandell, I., C. Fajers, and T. Lund, *Corrosion—One Root Cause for Premature Failures*, in *37th Leeds-Lyon Symposium on Tribology*. 2010.

28. Loos, J., I. Bergmann, and M. Goss, *Influence of Currents from Electrostatic Charges on WEC Formation in Rolling Bearings.* Tribology Transactions, 2016. **59**(5): p. 865-875.

29. Gegner, J., *Tribological aspects of rolling bearing failures*, in *INTECH Open Access Publisher*. 2011.

30. Gould, B.J. and D.L. Burris, *Effects of wind shear on wind turbine rotor loads and planetary bearing reliability.* Wind Energy, 2015. **19**: p. 1011-1021.

31. Garabedian, N., et al., *Wear and fatigue as contributors to the premature failure of wind turbine planet bearings - under-loading or over-loading?* Tribology Transactions, 2018.

32. Kang, Y.S., R.D. Evans, and G.L. Doll, *Roller-Raceway Slip Simulations of Wind Turbine Gearbox Bearings Using Dynamic Bearing Model.* Proceedings of the Stle/Asme International Joint Tribology Conference, 2010, 2011: p. 407-409.

33. Guzman, F.G., et al., *Reproduction of white etching cracks under rolling contact loading on thrust bearing and two-disc test rigs.* Wear, 2017. **390-391**: p. 23-32.

34. Danielsen, H.K., et al., *Multiscale characterization of White Etching Cracks (WEC) in a 100Cr6 bearing from a thrust bearing test rig.* Wear, 2017. **370**: p. 73-82.

35. Richardson, A.D., et al., *The Evolution of White Etching Cracks (WECs) in Rolling Contact Fatigue-Tested 100Cr6 Steel.* Tribology Letters, 2018. **66**(1).

36. Richardson, A.D., et al., *Thermal Desorption Analysis of Hydrogen in Non-hydrogen-Charged Rolling Contact Fatigue-Tested 100Cr6 Steel.* Tribology Letters, 2018. **66**(1).

37. Scepanskis, M., B. Gould, and A. Greco, *Empirical Investigation of Electricity Self-Generation in a Lubricated Sliding–Rolling Contact.* Tribology Letters, 2017. **65**: p. 109-119.

38. Evans, M.H., et al., *Confirming subsurface initiation at non-metallic inclusions as one mechanism for white etching crack (WEC) formation.* Tribology International, 2014. **75**: p. 87-97.

39. Franke, J., et al., *White Etching Cracking—Simulation in Bearing Rig and Bench Tests.* Tribology Transactions, 2017: p. 1-11.

40. Iso, K., A. Yokouchi, and H. Takemura, *Research work for clarifying the mechanism of white structure flaking and extending the life of bearings.* SAE Technical Paper, 2005(SP-1967): p. 39-48.

41. Vegter, R.H. and J.T. Slycke, *The Role of Hydrogen on Rolling Contact Fatigue Response of Rolling Element Bearings.* Journal of ASTM International, 2009. **7**(2): p. 1-12.

42. Uyama, H., et al., *The effects of hydrogen on microstructural change and surface originated flaking in rolling contact fatigue.* Tribology Online, 2011. **6**: p. 123-132.

43. Hiraoka, K., et al., *Generation process observation of micro-structural change in rolling contact fatigue by hydrogen-charged specimens.* Journal of Japanese Society of Tribologists, 2007. **52**(12): p. 888-895.

44. Kino, N. and K. Otani, *The influence of hydrogen on rolling contact fatigue life and its improvement.* Jsae Review, 2003. **24**(3): p. 289-294.

45. Tamada, K. and H. Tanaka, *Occurrence of brittle flaking on bearings used for automotive electrical instruments and auxiliary devices.* Wear, 1996. **199**(2): p. 245-252.

46. Ciruna, J.A. and H.J. Szieleit, *The effect of hydrogen on the rolling contact fatigue life of AISI 52100 and 440C steel balls.* Wear, 1973. **24**: p. 107-118.

47. Grunberg, L., *The Formation of Hydrogen Peroxide on Fresh Metal Surfaces.* Proceedings of the Physical Society of London Section B, 1953. **66**(399): p. 153-161.

48. Imran, T., B. Jacobson, and A. Shariff, *Quantifying diffused hydrogen in AISI-52100 bearing steel and in silver steel under tribo-mechanical action: Pure rotating bending, sliding-rotating bending, rolling-rotating bending and uni-axial tensile loading.* Wear, 2006. **261**(1): p. 86-95.

49. Ray, D., et al., *Hydrogen Embrittlement of a Stainless Ball-Bearing Steel.* Wear, 1980. **65**(1): p. 103-111.

50. Matsubara, Y. and H. Hamada, *A novel method to evaluate the influence of hydrogen on fatigue properties of high strength steels.* Journal of ASTM International, 2006. **3**: p. 1-14.

51. Lu, H., et al., *Hydrogen-enhanced dislocation emission, motion and nucleation of hydrogen-induced cracking for steel.* Science in China Series E-Technological Sciences, 1997. **40**(5): p. 530-538.

52. Fujita, S., et al., *Effect of hydrogen on Mode II fatigue crack behavior of tempered bearing steel and microstructural changes.* International Journal of Fatigue, 2010. **32**(6): p. 943-951.

53. Evans, M.H., et al., *Effect of hydrogen on butterfly and white etching crack (WEC) formation under rolling contact fatigue (RCF).* Wear, 2013. **306**(1-2): p. 226-241.

54. Ruellan, A., et al., *Understanding white etching cracks in rolling element bearings: The effect of hydrogen charging on the formation mechanisms.* Proceedings of the Institution of Mechanical Engineers, Part J: Journal of Engineering Tribology, 2014. **228**: p. 1252-1265.

55. Evans, M.H., et al., *White etching crack (WEC) investigation by serial sectioning, focused ion beam and 3-D crack modelling.* Tribology International, 2013. **65**: p. 146-160.

56. Paladugu, M. and R.S. Hyde, *White etching matter promoted by intergranular embrittlement.* Scripta Materialia, 2017. **130**: p. 219-222.

57. Paladugu, M. and R.S. Hyde, *Microstructure deformation and white etching matter formation along cracks.* Wear, 2017. **390-391**: p. 367-375.

58. Li, S.X., et al., *Microstructural evolution in bearing steel under rolling contact fatigue.* Wear, 2017. **380-381**: p. 146-153.

59. Bruce, T., et al., *Formation of white etching cracks at manganese sulfide (MnS) inclusions in bearing steel due to hammering impact loading.* Wind Energy, 2016. **19**(10): p. 1903-1915.

60. Gould, B., et al., *An analysis of premature cracking associated with microstructural alterations in an AISI 52100 failed wind turbine bearing using X-ray tomography.* Materials & Design, 2017. **117**: p. 417-429.

61. Gould, B., et al., *Using advanced tomography techniques to investigate the development of White Etching Cracks in a prematurely failed field bearing.* Tribology International, 2017. **116**: p. 362-370.

62. Errichello, R., R. Budny, and R. Eckert, *Investigations of Bearing Failures Associated with White Etching Areas (WEAs) in Wind Turbine Gearboxes.* Tribology Transactions, 2013. **56**(6): p. 1069-1076.

63. Paladugu, M. and R.S. Hyde, *Influence of microstructure on retained austenite and residual stress changes under rolling contact fatigue in mixed lubrication conditions.* Wear, 2018. **406-407**: p. 84-91.

64. Verhoeven, J.D., *Steel Metallurgy for the Non-Metallurgist*. 2007: ASM International.

65. Roy, S. and S. Sundararajan, *The effect of heat treatment routes on the retained austenite and Tribomechanical properties of carburized AISI 8620 steel.* Surface & Coatings Technology, 2016. **308**: p. 236-243.

66. Kim, H.J. and Y.G. Kweon, *The effects of retained austenite on dry sliding wear behavior of carburized steels.* Wear, 1996. **193**(1): p. 8-15.

67. Roy, S., et al., *Effect of laser treatment parameters on surface modification and tribological behavior of AISI 8620 steel.* Tribology International, 2017. **112**: p. 94-102.

68. Jenson, A.D., S. Roy, and S. Sundararajan, *The evolution of hardness and tribofilm growth during running-in of case carburized steel under boundary lubrication.* Tribology International, 2018. **118**: p. 1-10.

69. Choi, Y. and C.R. Liu, *Spall progression life model for rolling contact verified by finish hard machined surfaces.* Wear, 2007. **262**(1-2): p. 24-35.

70. Chung, Y.-W., *Introduction to Materials Science and Engineering*. 2006: CRC Press.

71. Evans, M.H., *White structure flaking (WSF) in wind turbine gearbox bearings: effects of 'butterflies' and white etching cracks (WECs).* Materials Science and Technology, 2012. **28**(1): p. 3-22.

72. Osterlund, R., et al., *Butterflies in gatigued all bearings-formation mechanism and structure.* Scandinavian Journal of Metallurgy, 1982. **11**: p. 23-32.

CHAPTER 8. CONCLUSION

Retained austenite or RA is a crucial phase in steel which has a significant impact on the wear and fatigue life of steel. In the first phase of my Ph.D. study, I have elucidated the impact of different heat treatment routes on controlling RA and micro-tribological (i.e. friction and wear) behavior of AISI 8620 steel. The significant results and observations with respect to each research objective are summarized below.

The effect of heat treatment routes on the retained austenite and tribomechanical properties of carburized AISI 8620 steel

A 3–15% range of RA with varied hardness and residual stress in AISI 8620 steel was achieved by varying carbon potential (0.45% to 1.05%) during carburizing as well as by employing different end-quenching routes (from air-cooling to deep freezing). Varying the carbon potential impacted the resulting range of RA% more than varying quenching routes. The higher carbon potential resulted in higher hardness due to increased carbon near the surface. The carburizing technique generates compressive residual stress which is beneficial for wear resistance. The hardness and amount of RA contribute more to the differences in wear behavior of samples as compared to the residual stresses. The results show that the combined effect of RA and hardness on the abrasive wear resistance is highly dependent on the contact stress. Below a certain pressure level, the effect of RA is insignificant. At higher contact pressures, a higher hardness and higher RA% result in superior wear resistance. This is attributed to the higher hardness resulting from the heat treatment route to generate higher RA% as well as martensitic transformation of austenite during sliding. The role of RA increases at higher penetration depths where the effect of

carbon potential (and hence hardness) plays a lesser role. The heat treatments did not significantly affect the coefficient of friction of the samples when subjected to dry sliding against a steel probe. The findings indicate that heat treatment technique for 8620 steel modelled in such a way as to produce higher hardness as well as moderately higher RA (~15%), through carburizing and quenching will yield increased abrasive wear resistance. This study also provides some insight into varying the RA in AISI 8620 steel, which is commonly used in drivetrains, and the effect that the RA can have on abrasive wear resistance.

Effect of laser treatment parameters on surface modification and tribological behavior of AISI 8620 steel

This study provides some insight to proper selection of scanning velocity and shielding gases during laser heat treatment to control the mechanical properties in AISI 8620 steel, which is commonly used in drivetrains. The results showed that it is possible to control RA levels below 10% by proper selection of power density and scanning velocity levels. Phase transformation based hardening occurs in this regime resulting in martensite and RA on the laser treated layer close to the surface. Generated RA% due to laser treatment is higher at lower scanning velocity and with air and nitrogen as a shielding gas compared to argon. The air and nitrogen shielded environments along with lower scanning velocity result in a higher hardness due to combination of deeper interaction volume and higher heat input. Oxygen content in air results higher surface roughness on laser treated sample but air shielded laser treatment showed largest interaction volume. This suggests that, nitrogen and oxygen can be blended to achieve a larger reaction volume along with reasonable surface rough ness. However, air shielded samples showed higher friction levels due to

shearing of oxide layers and high surface roughness compared to other samples. The nitrogen shielded samples with lower scanning velocity result in the most promising wear resistance behavior which is attributed to nitride formation on surface. The findings indicate that by proper selection of laser heat treatment parameters such as a nitrogen shielded environment with comparatively lower scanning velocity can result in a good combination of surface properties such as moderate RA% with higher surface hardness, lower surface roughness and better wear resistance for AISI 8620 steel.

Effect of retained austenite on micropitting behavior of carburized AISI 8620 steel under boundary lubrication

Steel samples with an RA range of 0-70% were prepared to evaluate the effect of RA on micropitting by varying carbon potential (1.2 to 2%) and tempering temperature and time. Experiments revealed that increasing RA% contributed to significant increase in micropitting life. The failure mechanism for the lowest RA samples was dominated by early crack initiation and rapid crack propagation, whereas samples with medium and high RA showed initiation and propagation of micropitting with clear evidence of RA transforming to martensite. It was observed that in case of 70% RA samples the RA was transformed to around 20% in 5 million cycles after which the transformation stabilized. Evolution of the phase transformation indicated that at 15% RA, almost all the RA is transformed to martensite within 10^4 cycles. XFEM simulations showed that higher amounts of RA delays fatigue crack growth and therefore micropitting life is improved. Secondly, inherent ductility of austenite also plays a beneficial role to delay crack initiation and propagation. Although 70% retained austenite sample exhibited the lowest compressive residual stress, it showed the maximum micropitting life. This indicates that

the role of retained austenite had greater impact than that of residual stress in affecting the micropitting life. Thus, ensuring a sufficiently high level of RA% at the start to enable a stable level remains after martensitic transformation is desirable for improved micropitting life. Overall, the findings provide valuable input for the design and manufacturing of drivetrain components for a wide range of applications under low lambda conditions ranging from agricultural equipment to the wind energy sectors.

Correlation between evolution of surface roughness parameters and micropitting of carburized steel under boundary lubrication condition

Four different amplitude roughness parameters and a spatial parameter were studied to investigate correlation between micropitting initiation and propagation and surface roughness parameters during rolling contact fatigue test of carburized AISI 8620 steel. Run-in occurred within the first 10^4 cycles of RCF tests for all samples, during which the Ra and R_{RMS} values dropped to around 50% of their initial value due to plastic deformation of asperity tips. This was accompanied by a drastic climb in the correlation length along the axial or transverse direction until stabilization was achieved. After run-in, 0% RA samples failed very quickly due to early crack initiation and rapid crack propagation. These cracks developed a channel-like formation in transverse direction, which caused a consistent increase in the correlation length until the surface became fully covered with cracks and resulted a nearly random surface in the axial direction. In case of 15 and 70% RA samples, micropitting initiation and propagation were observed. Ra and R_{RMS} increased with onset of cracking as well as initiation and propagation of micropitting. An inverse relationship exists between RMS roughness and correlation length. Similarly, this trend continued after run-in for the 15 and 70% RA cases. The propagation of micropitting and

correlation length also showed an inverse relationship in those samples. Skewness and kurtosis were found to be reliable indicators to detect initiation and propagation of micropitting. Micropitting acts like indents on surface which results in negative skewness during its propagation. On the other hand, kurtosis numbers will rise with increase of micropitting. The observed correlation between surface roughness parameter evolution and micropitting can be used to monitor and effectively predict the long-term performance of components subject to rolling contact fatigue under boundary lubrication regime.

Effect of retained austenite on spalling behavior of carburized AISI 8620 steel under boundary lubrication

Steel samples with an RA range of 0-70% were prepared to evaluate the effect of RA on macropitting or spalling by varying carbon potential (1.2 to 2%) and tempering temperature and time. Experiments revealed that microstructure with almost no RA showed the lowest spalling life. 70% RA samples showed better macropitting life compared to 0% RA samples even though it had larger sub-surface cracks at baseline condition. If RCF life for 0% and 15% RA samples are compared, both samples had insignificant sub-surface defects but 15% RA samples showed significantly improved macropitting life. In case of 70% RA samples, although they had very high RA but due to sub-surface cracks these samples did not show significantly higher RCF life than 15% RA samples. These observations confirm that increasing RA and decreasing sub-surface cracks at baseline condition can help to enhance macropitting life. The 0% RA samples had maximum residual stress but still showed lowest spalling life. Thus, the baseline residual stress cannot be the main factor to control macropitting behavior. The failure mechanism for all three samples were similar. Sub-surface cracks initially propagated in the circumferential direction and suddenly

deviated upwards to create a spall on the surface. Thus, in all cases spalling was due to sub-surface crack initiation and propagation. Samples with medium and high RA showed clear evidence of RA transforming to martensite. Higher amounts of RA can create more barriers for fatigue crack growth and therefore macropitting life is improved. Secondly, inherent ductility of austenite also plays a beneficial role to delay crack initiation and propagation. The study helps establish the role of RA on macropitting in the context of other mechanical and microstructural phenomena as well as the correlation of behavior to heat treatment routes for preferred fatigue life. Overall, the findings will provide valuable input for the design and manufacturing of drivetrain components for a wide range of applications under low lambda conditions ranging from agricultural equipment to the wind energy sectors.

Effect of retained austenite on white etching crack behavior of carburized steel under boundary lubrication

Steel samples with an RA range of 0-70% were prepared to evaluate the effect of RA on white etching crack behavior by varying carbon potential (1.2 to 2%) and tempering temperature and time. These samples were tested within the PCS Instruments micro-pitting rig under conditions which were previously documented to lead to the formation of WECs. While varying the RA level within test rollers only lead to minor changes in time until failure, it did cause drastic differences in the morphology of the WECs which developed within the samples. Samples which were tested in higher levels of RA contained far more branching crack networks, and the WEA adjacent to the crack networks was less defined. This shows positive impact of RA on WEC formation. The study helps establish the role of RA on WEC behavior in the context of other mechanical and microstructural phenomena as well as the correlation of behavior to heat treatment routes for preferred rolling contact

fatigue life. Overall, the findings provide valuable input for the design and manufacturing of drivetrain components for a wide range of applications under low lambda conditions ranging from agricultural equipment to the wind energy sectors.